The Astronomical Journal, 136:2782–2845, 2008 December doi:10.1088/0004-6256/136/6/2782

THE STAR FORMATION EFFICIENCY IN NEARBY GALAXIES: MEASURING WHERE GAS FORMS STARS EFFECTIVELY

Adam K. Leroy[1], Fabian Walter[1], Elias Brinks[2], Frank Bigiel[1], W. J. G. de Blok[3,4], Barry Madore[5], and M. D. Thornley[6]

[1] Max-Planck-Institut für Astronomie, Königstuhl 17, D-69117, Heidelberg, Germany
[2] Centre for Astrophysics Research, University of Hertfordshire, Hatfield AL10 9AB, UK
[3] Research School of Astronomy and Astrophysics, Mount Stromlo Observatory, Cotter Road, Weston ACT 2611, Australia
[4] Department of Astronomy, University of Cape Town, Private Bag X3, Rondebosch 7701, South Africa
[5] Observatories of the Carnegie Institution of Washington, Pasadena, CA 91101, USA
[6] Department of Physics and Astronomy, Bucknell University, Lewisburg, PA, 17837, USA
Received 2008 March 17; accepted 2008 September 25; published 2008 November 18

ABSTRACT

We measure the star formation efficiency (SFE), the star formation rate (SFR) per unit of gas, in 23 nearby galaxies and compare it with expectations from proposed star formation laws and thresholds. We use H I maps from The H I Nearby Galaxy Survey (THINGS) and derive H_2 maps of CO measured by HERA CO-Line Extragalactic Survey and Berkeley-Illinois-Maryland Association Survey of Nearby Galaxies. We estimate the SFR by combining *Galaxy Evolution Explorer* (*GALEX*) far-ultraviolet maps and the *Spitzer* Infrared Nearby Galaxies Survey (SINGS) 24 μm maps, infer stellar surface density profiles from SINGS 3.6 μm data, and use kinematics from THINGS. We measure the SFE as a function of the free fall and orbital timescales, midplane gas pressure, stability of the gas disk to collapse (including the effects of stars), the ability of perturbations to grow despite shear, and the ability of a cold phase to form. In spirals, the SFE of H_2 alone is nearly constant at $(5.25 \pm 2.5) \times 10^{-10}$ yr^{-1} (equivalent to an H_2 depletion time of 1.9×10^9 yr) as a function of all of these variables at our 800 pc resolution. Where the interstellar medium (ISM) is mostly H I, however, the SFE decreases with increasing radius in both spiral and dwarf galaxies, a decline reasonably described by an exponential with scale length $0.2r_{25}$–$0.25r_{25}$. We interpret this decline as a strong dependence of giant molecular cloud (GMC) formation on environment. The ratio of molecular-to-atomic gas appears to be a smooth function of radius, stellar surface density, and pressure spanning from the H_2-dominated to H I-dominated ISM. The radial decline in SFE is too steep to be reproduced only by increases in the free-fall time or orbital time. Thresholds for large-scale instability suggest that our disks are stable or marginally stable and do not show a clear link to the declining SFE. We suggest that ISM physics below the scales that we observe—phase balance in the H I, H_2 formation and destruction, and stellar feedback—governs the formation of GMCs from H I.

Key words: galaxies: evolution – galaxies: ISM – radio lines: galaxies – stars: formation

Online-only material: color figures, machine-readable and VO tables

1. INTRODUCTION

In nearby galaxies, the star formation rate (SFR) is observed to correlate spatially with the distribution of neutral gas, at least to first order. This is observed using a variety of SFR and gas tracers, but the quantitative relationship between the two remains poorly understood. Although it is common to relate SFR to gas surface density via a power law, the relationship is often more complex. The same surface density of gas can correspond to dramatically different SFRs depending on whether it is found in a spiral or irregular galaxy or in the inner or outer part of a galactic disk. Such variations have spurred suggestions that the local potential well, pressure, coriolis forces, chemical enrichment, or shear may regulate the formation of stars from the neutral interstellar medium (ISM).

In this paper, we compare a suite of proposed star formation laws and thresholds with observations. In this way, we seek to improve observational constraints on theories of galactic-scale star formation. Such theories are relevant to galaxy evolution at all redshifts, but must be mainly tested in nearby galaxies, where observations have the spatial resolution and sensitivity to map star formation to local conditions. An equally important goal is to calibrate and test empirical star formation recipes. In lieu of a strict theory of star formation, such recipes remain indispensable input for galaxy modeling, particularly because star formation takes place mostly below the resolution of cosmological simulations. This requires the implementation of "subgrid" models that map local conditions to the SFR (e.g., Springel & Hernquist 2003).

Our analysis is based on the highest quality data available for a significant sample of nearby galaxies: H I maps from The H I Nearby Galaxy Survey (THINGS; Walter et al. 2008), far-ultraviolet (FUV) maps from the *Galaxy Evolution Explorer* (*GALEX*) Nearby Galaxies Survey (Gil de Paz et al. 2007), infrared (IR) data from the *Spitzer* Infrared Nearby Galaxies Survey (SINGS; Kennicutt et al. 2003), CO 1 $\rightarrow$ 0 maps from the Berkeley-Illinois-Maryland Association (BIMA) Survey of Nearby Galaxies (BIMA SONG; Helfer et al. 2003), and CO 2 $\rightarrow$ 1 maps from the HERA CO-Line Extragalactic Survey (HERACLES; Leroy et al. 2008). This combination yields sensitive, spatially-resolved measurements of kinematics, gas surface density, stellar surface density, and SFR surface density across the entire optical disks of 23 spiral and irregular galaxies.

The topic of star formation in galaxies is closely linked to that of giant molecular cloud (GMC) formation. In the Milky Way, most star formation takes place in GMCs, which are predominantly molecular, gravitationally bound clouds with typical masses $\sim 10^5$–10^6 $M_\odot$ (Blitz 1993). Similar clouds

dominate the molecular ISM in Local Group galaxies (e.g., Fukui et al. 1999; Engargiola et al. 2003). If the same is true in other galaxies, then a close association between GMCs and star formation would be expected to be a general feature of our data. Bigiel et al. (2008) studied the relationship between atomic hydrogen (H I), molecular gas (H_2), and the SFR in the same data used here. Working at a resolution of 750 pc, they did not resolve individual GMCs, but did find that a single power law with an index $n = 1.0 \pm 0.2$ relates H_2 and SFR surface density over the optical disks of spirals. This suggests that as in the Milky Way, a key prerequisite to forming stars is the formation of GMCs (or at least H_2).

Bigiel et al. (2008) found no similar trend relating H I and SFR. Instead, the ratios of H_2-to-H I and SFR-to-H I vary strongly within and among galaxies. GMC formation, therefore, appears to be a function of local conditions. Here, we investigate this dependence. We focus on where the ISM can form gravitationally bound, predominantly molecular structures, that is, the "star formation threshold," and investigate how the molecular fraction of the ISM varies with local conditions. In equilibrium, the fraction of the ISM in GMCs may be set by the timescale over which these structures form. Therefore, we also consider suggested timescales for the formation of GMCs and compare them to observations.

Maps with good spatial coverage and sensitivity are critical to distinguish between the various proposed thresholds and timescales. Perhaps *the* key observation to test theories of galactic-scale star formation is that the star formation per unit gas mass decreases in the outer disks of spiral and irregular galaxies (e.g., Kennicutt 1989; Martin & Kennicutt 2001; Thornley et al. 2006). The details of this decrease vary with the specifics of the observations. For example, Martin & Kennicutt (2001) observed a sharp drop in the distribution of H II regions, while UV maps suggest a steady decline (Boissier et al. 2007), but this is without dispute that the SFR per unit gas mass does indeed decline (also see Wong & Blitz 2002). Maps with good spatial extent contain both regions where GMC formation proceeds efficiently and regions where it is suppressed. Including both H I-rich dwarf galaxies and H_2-dominated spirals offers a similar contrast.

In Section 2, we present a set of star formation laws and thresholds that we will compare to observations. We phrase these in terms of the star formation per unit neutral gas, which we call the "star formation efficiency (SFE)." This quantity, the inverse of the gas depletion time, removes the basic scaling between stars and gas and measures how effectively each parcel of the ISM forms stars.

In Section 3, we briefly describe our sample, data, and methodology. In order to focus the main part of the paper on analysis, we defer most detailed discussion of data and methodology to the appendices.

In Section 4, we look at how the SFE relates to other basic quantities (Section 4.1), proposed laws (Section 4.2), and thresholds (Section 4.3). In Section 5, we analyze and interpret these results. In Section 6, we illustrate our conclusions by comparing predictions for the SFE to observations. In Section 7, we give our conclusions.

Appendices A–D contain all the information required to reproduce our calculations, including descriptions of the data and how we convert from observables to physical quantities. We present our data as an electronic table of radial profiles described in Appendix E and as maps and plotted profiles for each galaxy in Appendix F.

2. BACKGROUND

Following, for example, Kennicutt (1989), we break the topic of star formation in galaxies into two parts. Where star formation is widespread, we refer to the quantitative relationship between neutral gas and the SFR as the star formation *law*. To predict the SFR over an entire galactic disk, it is also necessary to know which gas actively forms stars. This topic is often phrased as the star formation *threshold*, but may be more generally thought of as the problem of where a cold phase ($n \sim$ 4–80 cm^{-3}, $T \sim$ 50–200 K) or gravitationally bound clouds can form; both are thought to be prerequisites to star formation. We give a brief background on both laws and thresholds, first noting that neither term is strictly accurate: "laws" here refer to observed (or predicted) correlations and the "threshold" is probably a smooth variation from non-star-forming to actively star-forming gas.

We cast this discussion in terms of the SFE. There are many definitions for the SFE, but throughout this paper, we use the term only to refer to the SFR surface density per unit neutral gas surface density along a line of sight (LOS), that is, SFE = $\Sigma_{\rm SFR}/\Sigma_{\rm gas}$ with units of yr^{-1}. We will also discuss SFE (H_2), which refers to the SFR per unit H_2 ($\Sigma_{\rm SFR}/\Sigma_{\rm H_2}$), and SFE (H I) ($\Sigma_{\rm SFR}/\Sigma_{\rm H\,I}$). The SFE is the inverse of the gas depletion time, the time required for present-day star formation to consume the gas reservoir. It represents a combination of the real timescale for neutral gas to form stars and the fraction of gas that ends up in stars; for example, if 1% of the gas is converted to stars every 10^7 yr, the SFE = 10^{-9} yr^{-1}. Because it is normalized by $\Sigma_{\rm gas}$, the SFE is more useful than $\Sigma_{\rm SFR}$ alone to identify where conditions are conducive to star formation (i.e., where gas is "good at forming stars").

As we describe proposed laws (Section 2.1) and thresholds (Section 2.2), we present quantitative forms for each that can be compared to the observed SFE. Table 1 collects these expressions, which we compare to observations in Section 4.

2.1. Star Formation Laws

A star formation law should predict the SFE from local conditions. Here we describe three proposals for the limiting timescale over which gas forms stars: the free-fall timescale in the gas disk, the orbital timescale, and the characteristic timescale for cloud-cloud collisions. We also describe proposals that GMCs form stars with a fixed SFE and that the midplane gas pressure regulates the fraction of the ISM in the molecular phase. We present each proposal as a prediction for the SFE in terms of observables. These appear together in the upper part of Table 1.

2.1.1. Disk Free-Fall Time With Fixed Scale Height

The most common formulation of the star formation law is a power law relating gas and star formation (surface) densities following Schmidt (1959, 1963). Kennicutt (1989, 1998a) calibrated this law in its observable (surface density) form. Averaging over the star-forming disks of spiral and starburst galaxies, he found

$$\Sigma_{\rm SFR} \propto \Sigma_{\rm gas}^{1.4}, \quad (1)$$

often referred to as the "Kennicutt–Schmidt law."

The exponent in Equation (1), $n \approx 1.5$, can be approximately explained by arguing that stars form with a characteristic timescale equal to the free-fall time in the gas disk, which in turn inversely depends on the square root of the gas volume density, $\tau_{\rm ff} \propto \rho_{\rm gas}^{-0.5}$ (e.g., Madore 1977). For a fixed scale height,

Table 1
Star Formation Laws and Thresholds

Theory	Form	Observables
	Star Formation Laws	
Disk free-fall time		
... fixed scale height	$\mathrm{SFE} \propto \Sigma_{\rm gas}^{0.5}$	$\Sigma_{\rm gas}$
... variable scale height	SFE or $R_{\rm mol} \propto \frac{\Sigma_{\rm gas}}{\sigma_{\rm g}} \left(1 + \frac{\Sigma_*}{\Sigma_{\rm gas}} \frac{\sigma_{\rm g}}{\sigma_{*,z}}\right)^{0.5}$	$\Sigma_{\rm gas}, \Sigma_*, \sigma_g, \sigma_*$
Orbital timescale	SFE or $R_{\rm mol} \propto \tau_{\rm orb}^{-1} = \frac{v(r_{\rm gal})}{2\pi r_{\rm gal}}$	$v(r_{\rm gal})$
Cloud–cloud collisions	$\mathrm{SFE} \propto \tau_{\rm orb}^{-1} Q_{\rm gas}^{-1}(1 - 0.7\beta)$	$v(r_{\rm gal})$
Fixed GMC efficiency	$\mathrm{SFE} = \mathrm{SFE}(\mathrm{H_2}) \frac{R_{\rm mol}}{R_{\rm mol}+1}$	$\Sigma_{\rm H_2}$
Pressure and ISM phase	$R_{\rm mol} \propto (\Sigma_{\rm gas}(\Sigma_{\rm gas} + \frac{\sigma_{\rm g}}{\sigma_{*,z}}\Sigma_*) P_0^{-1})^{1.2}$	$\Sigma_{\rm gas}, \Sigma_*, \sigma_{\rm g}, \sigma_*$
	Star Formation Thresholds	
Gravitational instability		
... in the gas disk	$Q_{\rm gas} = \left(\frac{\sigma_{\rm g}\kappa}{\pi G \Sigma_{\rm gas}}\right) < 1$	$\Sigma_{\rm gas}, \sigma_{\rm g}, v(r_{\rm gal})$
... in a disk of gas and stars	$Q_{\rm stars+gas} = \left(\frac{2}{Q_{\rm stars}} \frac{q}{1+q^2} + \frac{2}{Q_{\rm gas}} R \frac{q}{1+q^2 R^2}\right)^{-1} < 1$	$\Sigma_{\rm gas}, \Sigma_*, \sigma_{\rm g}, \sigma_*, v(r_{\rm gal})$
Competition with shear	$\Sigma_{\rm gas} > \frac{2.5 A \sigma_{\rm g}}{\pi G}$	$\Sigma_{\rm gas}, \sigma_{\rm g}, v(r_{\rm gal})$
Cold gas phase	$\Sigma_{\rm gas} > 6.1\ M_\odot\ \mathrm{pc}^{-2} f_{\rm g}^{0.3} Z^{-0.3} I^{0.23}$	$\Sigma_{\rm gas}, \Sigma_*, Z, I$

$\rho_{\rm gas} \propto \Sigma_{\rm gas}$ and $\Sigma_{\rm SFR} \propto \Sigma_{\rm gas}^{1.5}$. Thus, the first star formation law that we consider is

$$\mathrm{SFE} \propto \Sigma_{\rm gas}^{0.5}, \tag{2}$$

which is approximately Equation (1).

2.1.2. Disk Free-Fall Time With Variable Scale Height

If the scale height is not fixed, but instead set by hydrostatic equilibrium in the disk, then

$$\tau_{\rm ff} \propto \frac{1}{\sqrt{\rho_{\rm mp,gas}}} \propto \frac{\sigma_{\rm g}}{\Sigma_{\rm gas}\sqrt{1 + \frac{\Sigma_*}{\Sigma_{\rm gas}} \frac{\sigma_{\rm g}}{\sigma_{*,z}}}}, \tag{3}$$

where $\sigma_{\rm g}$ and $\sigma_{*,z}$ are the (vertical) velocity dispersions of gas and stars, respectively, $\Sigma_{\rm gas}$ and Σ_* are the surface densities of the same, and $\rho_{\rm mp,gas}$ is the midplane gas density. Equation (3) combines the expression for midplane density from Krumholz & McKee (2005, their Equation 34) and midplane gas pressure from Elmegreen (1989, his Equation 11, used to calculate ϕ_P). The second star formation law that we consider is

$$\mathrm{SFE} \propto \tau_{\rm ff}^{-1} \propto \frac{\Sigma_{\rm gas}}{\sigma_{\rm g}} \left(1 + \frac{\Sigma_*}{\Sigma_{\rm gas}} \frac{\sigma_{\rm g}}{\sigma_{*,z}}\right)^{0.5}, \tag{4}$$

which incorporates variations in the scale height and thus gas volume density with a changing potential well.

2.1.3. Orbital Timescale

It is also common to equate the timescale for star formation and the orbital timescale (e.g., Silk 1997; Elmegreen 1997). Kennicutt (1998a) and Wong & Blitz (2002) found that such a formulation performs as well as Equation (1). In this case,

$$\mathrm{SFE} \propto \tau_{\rm orb}^{-1} = \frac{\Omega}{2\pi} = \frac{v(r_{\rm gal})}{2\pi r_{\rm gal}}, \tag{5}$$

where $v(r_{\rm gal})$ is the rotational velocity at a galactocentric radius $r_{\rm gal}$ and Ω is the corresponding angular velocity.

2.1.4. Cloud–Cloud Collisions

Tan (2000) suggested that the rate of collisions between gravitationally bound clouds sets the timescale for star formation so that

$$\mathrm{SFE} \propto \tau_{\rm orb}^{-1} Q_{\rm gas}^{-1}(1 - 0.7\beta), \tag{6}$$

where $Q_{\rm gas}$, defined below, measures gravitational instability in the disk and $\beta = d \log v(r_{\rm gal})/d \log r_{\rm gal}$ is the logarithmic derivative of the rotation curve. The dependence on β reflects the importance of galactic shear in setting the frequency of cloud–cloud collisions. In the limit $\beta = 0$ (a flat rotation curve), this prescription reduces to essentially Equation (5); for $\beta = 1$ (solid body rotation), the SFE is depressed by the absence of shear.

2.1.5. Fixed GMC Efficiency

If the SFE of an individual GMC depends on its intrinsic properties and if these properties are not themselves strong functions of environment or formation mechanism, then we expect a fixed SFR per unit molecular gas, SFE ($\mathrm{H_2}$). Krumholz & McKee (2005) posited such a case, arguing that the SFE of a GMC depends on the free-fall time in the cloud, itself only a weak function of cloud mass in the Milky Way (Solomon et al. 1987). Bigiel et al. (2008) found support for this idea. Studying the same data used here, they derived a linear relationship between $\Sigma_{\rm H_2}$ and $\Sigma_{\rm SFR}$ on scales of 750 pc.

SFE ($\mathrm{H_2}$) is likely to appear constant if the scaling relations and mass spectrum (i.e., the intrinsic properties) of GMCs are approximately universal, the gas pressure is low enough that GMCs are largely decoupled from the rest of the ISM, individual resolution elements contain at least a few GMCs, and the properties of a cloud regulate its ability to form stars (Section 5.1 and Bigiel et al. 2008). This is the fifth star formation law that we consider, that star formation in spiral galaxies occurs mostly in GMCs and that once such clouds are formed, they have approximately uniform properties so that

$$\mathrm{SFE}(\mathrm{H_2}) = \text{constant}, \tag{7}$$

which we can convert to the SFE of the total gas given $R_{\rm mol} = \Sigma_{\rm H_2}/\Sigma_{\rm H\,I}$, the ratio of $\mathrm{H_2}$ to H I gas. Then,

$$\mathrm{SFE} = \mathrm{SFE}(\mathrm{H_2}) \frac{R_{\rm mol}}{R_{\rm mol} + 1}, \tag{8}$$

or if we measure only $\Sigma_{\rm H\,I}$ (as is the case in dwarfs), then SFE(HI) = SFE(H_2)$R_{\rm mol}$.

The balance between GMC/H_2 formation and destruction will set $R_{\rm mol} = \Sigma_{H_2}/\Sigma_{\rm H\,I}$. If GMCs with a fixed lifetime form over a free-fall time or orbital time, then $R_{\rm mol} \propto \tau_{\rm ff}^{-1}$ or $R_{\rm mol} \propto \tau_{\rm orb}^{-1}$ (Section 5.4), which we have noted in Table 1. Combined with Equation (8), an expression for $R_{\rm mol}$ predicts the SFE.

2.1.6. Pressure and Phase of the ISM

Wong & Blitz (2002), Blitz & Rosolowsky (2004), and Blitz & Rosolowsky (2006) explicitly considered $R_{\rm mol}$. Following Elmegreen (1989) and Elmegreen & Parravano (1994), they identified pressure as the critical quantity that sets the ability of the ISM to form H_2. They showed that the midplane hydrostatic gas pressure, $P_{\rm h}$, correlates with this ratio in the inner parts of spiral galaxies.

Pressure, which is directly proportional to the gas volume density, should affect both the rate of H_2 formation/destruction and the likelihood of a gravitationally unstable overdensity condensing out of a turbulent ISM (Elmegreen 1989; Elmegreen & Parravano 1994). Elmegreen (1989) gives the following expression for $P_{\rm h}$:

$$P_{\rm h} \approx \frac{\pi}{2} G \Sigma_{\rm gas} \left(\Sigma_{\rm gas} + \frac{\sigma_{\rm g}}{\sigma_{*,z}} \Sigma_{*} \right), \tag{9}$$

and Elmegreen (1993) predicted that the fraction of gas in the molecular phase depends on both $P_{\rm h}$ and the interstellar radiation field, j, via $R_{\rm mol} \propto P^{2.2} j^{-1}$. If $\Sigma_{\rm SFR} \propto \Sigma_{H_2}$ and we make the simple assumption that $j \propto \Sigma_{\rm SFR}$, then Elmegreen (1993) predicts

$$R_{\rm mol} \propto P_h^{1.2} \quad \text{or} \quad \Sigma_{H_2} = \Sigma_{\rm H\,I} P_h^{1.2}, \tag{10}$$

which combines with Equation (8) to predict the SFE.

Wong & Blitz (2002) and Blitz & Rosolowsky (2006) found observational support for Equation (10). Using a modified Equation (9) appropriate where $\Sigma_* \gtrsim \Sigma_{\rm gas}$, Blitz & Rosolowsky (2006) fitted a power law of the form

$$R_{\rm mol} = \frac{\Sigma_{\rm H2}}{\Sigma_{\rm HI}} = \left(\frac{P_h}{P_0} \right)^{\alpha}, \tag{11}$$

finding $P_0 = 4.3 \times 10^4$ cm^{-3} K, the observed pressure where the ISM is equal parts of H I and H_2, and a best-fit exponent $\alpha = 0.92$. Wong & Blitz (2002) found $\alpha = 0.8$. Robertson & Kravtsov (2008) recently found support from simulations for $\alpha \sim 0.9$.

2.2. Star Formation Thresholds

We have described suggestions for the efficiency with which gas form stars, but not *whether* gas forms stars. A "star formation threshold" is often invoked to accompany a star formation law. This is a criterion designed to address the question "which gas is actively forming stars?" or "where can the ISM form gravitationally bound, molecular clouds?" and proposed thresholds have mostly focused on the existence of gravitational or thermal instability in the gas disk.

A common way to treat the issue of thresholds is to formulate a critical gas surface density, $\Sigma_{\rm crit}$, that is a function of local conditions—kinematics, stellar surface density, or metallicity. If $\Sigma_{\rm gas}$ is below $\Sigma_{\rm crit}$, star formation is expected to be suppressed; we refer to such regions as "subcritical." Where the gas surface density is above the critical surface density, star formation is expected to be widespread. We refer to such regions as "supercritical."

In practice, we expect to observe a drop in the SFE associated with the transition from supercritical to subcritical. We do not necessarily expect SFE = 0 in subcritical regions. Even with excellent resolution, an LOS through a galaxy probes a range of physical conditions and this is certainly true at our working resolution of 400–800 pc. Within a subcritical resolution element, star formation may still occur in isolated pockets that locally meet the threshold criterion.

Expressions for star formation thresholds are collected in the lower part of Table 1.

2.2.1. Gravitational Instability

Kennicutt (1989, 1998a) and Martin & Kennicutt (2001) argued that star formation is only widespread where the gas disk is unstable against large-scale collapse. Following Toomre (1964), the condition for instability in a thin gas disk is

$$Q_{\rm gas} = \frac{\sigma_g \kappa}{\pi G \Sigma_{\rm gas}} < 1. \tag{12}$$

where σ_g is the gas velocity dispersion, G is the gravitational constant, and κ is the epicyclic frequency, calculated via

$$\kappa = 1.41 \frac{v(r_{\rm gal})}{r_{\rm gal}} \sqrt{1+\beta}, \tag{13}$$

where $\beta = d \log v(r_{\rm gal})/d \log r_{\rm gal}$.

Martin & Kennicutt (2001) found that H II regions are common where $\Sigma_{\rm gas}$ exceeds a critical surface density derived following Equation (12),

$$\Sigma_{{\rm crit},Q} = \alpha_Q \frac{\sigma_g \kappa}{\pi G}. \tag{14}$$

In regions where $\Sigma_{\rm gas}$ is above this threshold, gas is unstable against large-scale collapse, which leads to star formation. Below the threshold, Coriolis forces counteract the self-gravity of the gas and suppress cloud/star formation. The factor α_Q is an empirical calibration, the observed average value of $1/Q_{\rm gas}$ at the star formation threshold. For an ideal thin gas disk, $\alpha_Q = 1$. At the edge of star-forming disks, Kennicutt (1989) found $\alpha_Q = 0.63$ and Martin & Kennicutt (2001) found $\alpha_Q = 0.69$ ($Q_{\rm gas} \sim 1.5$).

Kennicutt (1989) and Martin & Kennicutt (2001) mentioned the influence of stars as a possible cause for $Q_{\rm gas} > 1$ at the star formation threshold. Hunter et al. (1998a) presented an in-depth discussion of how several factors influence α_Q, for example stars and viscosity lower it, while the thickness of the gas disk raises it. Kim & Ostriker (2001, 2007) argued, based on simulations, that the observed threshold corresponds to the onset of nonlinear, nonaxisymmetric instabilities. Schaye (2004) and de Blok & Walter (2006) suggested a different explanation: $\alpha_Q \neq 1$, because σ_g has been systematically mishandled; they pointed out that σ_g measured from 21 cm emission will overestimate the true velocity dispersion of gas in a cold phase.

The stellar potential well may substantially affect the stability of the gas disk. Rafikov (2001) extended work by Jog & Solomon (1984) to provide a straightforward way to calculate the instability of a gas disk in the presence of a collisionless stellar disk. Rafikov defined

$$Q_{\rm stars} = \frac{\sigma_{*,r} \kappa}{\pi G \Sigma_*}, \tag{15}$$

where $\sigma_{*,r}$ is the (radial) velocity dispersion of stars and Σ_* is the stellar mass surface density. The condition for instability in the gas disk is

$$\frac{1}{Q_{\rm stars+gas}} = \frac{2}{Q_{\rm stars}}\frac{q}{1+q^2} + \frac{2}{Q_{\rm gas}}R\frac{q}{1+q^2R^2} > 1, \quad (16)$$

where $q = k\sigma_{*,r}/\kappa$, with k the wavenumber of the instability being considered, and $R = \sigma_{\rm g}/\sigma_{*,r}$. The minimum value of $Q_{\rm stars+gas}$ indicates whether the gas disk is unstable to large-scale collapse. In our sample, typical values of q correspond to wavelengths $\lambda = 2\pi/k \approx$ 1–5 kpc at maximum instability.

Hunter et al. (1998a) and Blitz & Rosolowsky (2004) observed strong correlations between star and GMC formation and the distribution of stars, consistent with stellar gravity playing a key role in star formation. Yang et al. (2007) recently showed that $Q_{\rm stars+gas}$ does an excellent job of predicting the location of star formation in the Large Magellanic Cloud (LMC), and Boissier et al. (2003) showed that including stars improves the correspondence between Q and star formation in disk galaxies. Li et al. (2005, 2006) found the same results from numerical simulations of disk galaxies, that is, stability against large-scale collapse critically depends on the stellar potential well, with star formation where $Q_{\rm stars+gas} \lesssim 1.6$.

2.2.2. Galactic Shear

Motivated by the failure of the Toomre $Q_{\rm gas}$ threshold in dwarf irregular galaxies, Hunter et al. (1998a) suggested that collecting the material for cloud formation may be easier than implied by $Q_{\rm gas}$, for example, through the aid of magnetic fields (see also Kim & Ostriker 2001). They hypothesized that the destructive influence of galactic shear may instead limit where GMCs can form and describe a threshold that depends on the ability of clouds to form in the time allowed by shear.

This threshold is based on the local shear rate, described by Oort's A constant:

$$A = -0.5 r_{\rm gal}\frac{d\Omega}{dr_{\rm gal}}. \quad (17)$$

Substituting $\Omega = v(r_{\rm gal})/r_{\rm gal}$,

$$A = 0.5\left(\frac{v(r_{\rm gal})}{r_{\rm gal}} - \frac{dv(r_{\rm gal})}{dr_{\rm gal}}\right) = 0.5\frac{v(r_{\rm gal})}{r_{\rm gal}}(1-\beta). \quad (18)$$

Then the threshold has the form

$$\Sigma_{\rm crit,A} = \frac{\alpha_A \sigma_g A}{\pi G}. \quad (19)$$

Hunter et al. (1998a) suggested $\alpha_{\rm A} = 2.5$, but this normalization for $\Sigma_{\rm crit,A}$ is relatively uncertain. The value chosen by Hunter et al. (1998a) corresponds to perturbations growing by a factor of ∼100 during the time allowed by shear, which roughly matches both the surface density contrast between $\Sigma_{\rm H\,I}$ and a GMC and the condition $Q_{\rm gas} \lesssim 1$ where $dv(r_{\rm gal})/dr_{\rm gal} = 0$.

The practical advantage of shear over $Q_{\rm gas}$ is that shear is low in dwarf galaxies and the inner disks of spiral galaxies ($\beta = 1$ for solid body rotation), both locales where widespread star formation is observed. In the outer disks of spiral galaxies—where star formation cutoffs are observed—rotation curves tend to be flat ($\beta = 0$) so that $\Sigma_{\rm crit,A}$ and $\Sigma_{\rm crit,Q}$ reduce to the same form.

2.2.3. Formation of a Cold Phase

The very long time needed to assemble a massive GMC from coagulation of smaller clouds suggests that most GMCs in galaxy disks form "top down" (e.g., McKee & Ostriker 2007). However, this does not necessarily require the whole gas disk to be unstable. Where cold H I is abundant, the lower velocity dispersion associated with this phase may render the ISM locally unstable (Schaye 2004), leading to the formation of GMCs and stars.

Therefore, instead of large-scale gravitational instability or cloud destruction by shear, the ability to form a cold neutral medium (McKee & Ostriker 1977; Wolfire et al. 2003) may regulate GMC formation. Schaye (2004) argued, based on modeling, that near the cutoffs observed by Martin & Kennicutt (2001), gas becomes mostly cold H I and H_2, σ_g drops accordingly, and Q becomes less than 1 in the cold gas. In a similar vein, Elmegreen & Parravano (1994) suggested that the SFE in the outer parts of galaxies drops because the pressure becomes too low to allow a cold phase to form even given perturbations, for example, from supernova shocks. Braun (1997) found support for this idea using 21 cm observations; he associated networks of high surface brightness filaments with cold H I and showed that these filaments are pervasive across the star-forming disk, but become less common at large radii (though work on THINGS by A. Usero et al. 2008, in preparation, calls this result into question).

Schaye (2004) modeled the ISM to estimate where the average temperature drops to ≈ 500 K, the molecular fraction reaches $\approx 10^{-3}$, and $Q_{\rm gas} \approx 1$, which are good indicators that cold H I is common and H_2 formation is efficient. These all occur where $\Sigma_{\rm gas}$ exceeds

$$\Sigma_{\rm S04} \approx \frac{6.1}{M_\odot\ {\rm pc}^{-2}}\ f_{\rm g}^{0.3}\left(\frac{Z}{0.1Z_\odot}\right)^{-0.3}\left(\frac{I}{10^6\ {\rm cm}^{-2}\ {\rm s}^{-1}}\right)^{0.23}, \quad (20)$$

where $f_{\rm g} \approx \Sigma_{\rm gas}/(\Sigma_{\rm gas}+\Sigma_*)$ is the fraction of mass in gas (we assume a two-component disk), Z is the metallicity of the ISM, and I is the flux of ionizing photons. $\Sigma_{\rm S04}$ also depends on the ratio of thermal to turbulent pressure and higher-order terms not shown here. Schaye (2004) selected fiducial values to match those expected in outer galaxy disks, but concluded that the influence of Z, $f_{\rm g}$, and the radiation field is relatively small. Most reasonable values yield $\Sigma_{\rm S04} \approx$ 3–10 $M_\odot$ pc^{-2}.

Schaye (2004) argued that a simple column density threshold may work as well as dynamical thresholds. This agrees with the observation by, for example, Skillman (1987) and de Blok & Walter (2006) that a simple H I column density threshold does a good job of predicting the location of star formation in dwarf irregulars. This threshold, $\Sigma_{\rm H\,I} \approx 10\ M_\odot$ pc^{-2}, also corresponds to the surface density above which H I is observed to saturate (Martin & Kennicutt 2001; Wong & Blitz 2002; Bigiel et al. 2008), that is, gas in excess of this surface density in spiral galaxies is in the molecular phase.

3. DATA

The right-hand column of Table 1 lists the observables required to evaluate each law or threshold. We require estimates of the surface density of atomic gas ($\Sigma_{\rm H\,I}$), molecular gas ($\Sigma_{\rm H_2}$), SFR ($\Sigma_{\rm SFR}$), and stellar mass (Σ_*), the velocity dispersions of gas and stars ($\sigma_{\rm gas}$ and σ_*), and the rotation curve ($v(r_{\rm gal})$). Estimates of the metallicity await future work.

Table 2
Sample Galaxies

Galaxy[a]	Res.[b] (″)	CO	Rotation Curve[c]	Also in Sample of[d]
DDO 154	19	...	dB	...
Ho I	21	...	T	...
Ho II	24	...	T	...
IC 2574	21	...	dB	...
NGC 4214[e]	28	...	T	...
NGC 2976	23	...	dB	...
NGC 4449[e]	20	...	...	...
NGC 3077[e]	22	...	...	...
NGC 7793	21	...	dB	...
NGC 925	9	...	dB	1, 2, 4
NGC 2403	26	...	dB	1, 2, 4
NGC 628	23	HERACLES	T	1, 2
NGC 3198	12	HERACLES	dB	...
NGC 3184	15	HERACLES	T	...
NGC 4736	35	HERACLES	dB	1, 2, 3, 5
NGC 3351	16	HERACLES	T	...
NGC 6946	28	HERACLES	dB	2
NGC 3627	18	BIMA SONG	dB	5
NGC 5194	21	BIMA SONG	T	2, 4, 5
NGC 3521	15	HERACLES	dB	5
NGC 2841	12	HERACLES	dB	1, 2
NGC 5055	16	HERACLES	dB	2, 3, 5
NGC 7331	11	HERACLES	dB	2, 5

Notes.
[a] In order of increasing stellar mass.
[b] Angular resolution to match working spatial resolution in the subsample, 400 pc for dwarf galaxies and 800 pc for spirals.
[c] Rotation curve data: dB = de Blok et al. (2008); T = only THINGS first moment (Walter et al. 2008).
[d] 1: Kennicutt (1989); 2: Martin & Kennicutt (2001); 3: Wong & Blitz (2002); 4: Boissier et al. (2003); 5: Blitz & Rosolowsky (2006).
[e] IR data from *Spitzer* archive (not SINGS).

3.1. The Sample

We assemble maps and radial profiles of the necessary quantities in 23 nearby, star-forming galaxies that we list in order of increasing stellar mass in Table 2. These are galaxies for which we could compile the necessary data, which means the overlap of THINGS, SINGS, the *GALEX* Nearby Galaxy Survey (NGS), and (for spirals) either BIMA SONG or HERACLES.

We work with two subsamples: 11 H I-dominated, low-mass galaxies and 12 large spiral galaxies. In Table 2, the galaxies that we classify "dwarf galaxies" lie above the horizontal dividing line. These have rotation velocities $v_{\rm rot} \lesssim 125$ km s^{-1}, stellar masses $M_* \lesssim 10^{10}\ M_\odot$, and $M_B \gtrsim -20$ mag. The galaxies that we label "spirals" lie below the dividing line and have $v_{\rm rot} \gtrsim 125$ km s^{-1}, $M_* \gtrsim 10^{10}\ M_\odot$, and $M_B \lesssim -20$ mag.

This division allows us to explore two distinct regimes in parallel. Compared with their larger cousins, dwarf galaxies have low metallicities, intense radiation fields, lower galactic shear, and a weak or absent spiral structure. Metallicity, in particular, should have a strong effect on the thermal balance of the ISM. In lieu of direct measurements, separating the sample in this way allows us to assess its impact.

We treat the two subsamples differently in two ways. First, we place data for spirals at a common spatial resolution of 800 pc and data for dwarf galaxies at 400 pc. The spirals in our sample are farther away than the dwarf galaxies with larger physical radii, and this approach ensures a good number of resolution elements across each galaxy and a fairly uniform angular resolution of ∼20″ (see Table 2).

Second, we use CO maps combined with a constant CO-to-H_2 conversion factor, $X_{\rm CO}$, to derive $\Sigma_{\rm H_2}$ in spirals, while we treat the molecular gas content of dwarf galaxies as unknown (see Appendix A.3). CO emission in very low mass galaxies is usually weak or not detected (e.g., Taylor et al. 1998; Leroy et al. 2005, and see Table 4) and its interpretation is confused by potential variations in $X_{\rm CO}$. Because dwarf galaxies lack H_2-filled H I depressions like those observed in the centers of spirals, we expect $\Sigma_{\rm H\,I}$ to at least capture the basic morphology of the total gas. Although we do not measure $\Sigma_{\rm H_2}$ in dwarf galaxies, we consider our results in light of the possibility of an unseen reservoir of molecular gas (Section 5.3).

3.2. Data to Physical Quantities

Appendices A–D explain in detail how we translate observables into physical quantities. Here and in Table 3, we summarize this mapping.

Atomic Hydrogen Surface Density (Appendix A). We derive atomic gas mass surface density, $\Sigma_{\rm H\,I}$, from 21 cm line integrated intensity maps obtained by Walter et al. (2008) as part of the THINGS survey using the Very Large Array (VLA).[7] $\Sigma_{\rm H\,I}$ is corrected for inclination and includes a factor of 1.36 to account for helium.

Molecular Hydrogen Surface Density (Appendix A). In spirals, we estimate the molecular gas mass surface density, $\Sigma_{\rm H_2}$, from CO line emission. For 10 galaxies, we use data from HERACLES, a large program at the IRAM[8] 30 m telescope (Leroy et al. 2008) that used the HERA focal plane array (Schuster et al. 2004) to map a subsample of THINGS in the CO $J = 2 \rightarrow 1$ line. For NGC 3627 and NGC 5194, we use $J = 1 \rightarrow 0$ line maps from the BIMA SONG survey (Helfer et al. 2003).

We convert from CO line intensity to $\Sigma_{\rm H_2}$ assuming a constant CO-to-H_2 conversion factor appropriate for the solar neighborhood, $X_{\rm CO} = 2 \times 10^{20}$ cm^{-2} (K km s^{-1})$^{-1}$, and a fixed line ratio $I_{\rm CO}(2 \rightarrow 1) = 0.8 I_{\rm CO}(1 \rightarrow 0)$, typical of the disks of spiral galaxies. We correct for the effects of inclination and include a factor of 1.36 to reflect the presence of helium.

Galactic Rotation (Appendix B). We fit a simple functional form to the high-quality rotation curves derived from THINGS by de Blok et al. (2008) and the THINGS first moment maps (Walter et al. 2008). These fits yield smooth, well-behaved (analytic) derivatives and match well the observations. Two galaxies (NGC 3077 and NGC 4449) have complex velocity fields that require substantial effort to interpret, and we omit them from analyses requiring kinematics.

Gas Velocity Dispersion (Appendix B). We assume a fixed gas velocity dispersion, $\sigma_{\rm gas} = 11$ km s^{-1}, a value motivated by the THINGS second moment maps.

Stellar Velocity Dispersion (Appendix B). We estimate the vertical stellar velocity dispersion, $\sigma_{*,z}$, from hydrostatic equilibrium, the assumption of an isothermal disk, and an estimated (radially invariant) stellar scale height. We derive this scale height for each galaxy from our measured stellar scale length and an average flattening ratio for disk galaxies. We

[7] The VLA is operated by the National Radio Astronomy Observatory (NRAO), which is a facility of the National Science Foundation operated under cooperative agreement by Associated Universities, Inc.
[8] IRAM is supported by CNRS/INSU (France), the MPG (Germany), and the IGN (Spain).

Table 3
Data to Physical Quantities

Quantity	Observation	Survey	Reference	Key Assumptions
$\Sigma_{\rm H\,I}$	21 cm line	THINGS	Walter et al. (2008)	
$\Sigma_{\rm H_2}$ (spirals only)	CO 2 → 1	HERACLES	Leroy et al. (2008)	Fixed line ratio, CO-to-H_2 conversion
	CO 1 → 0	BIMA SONG	Helfer et al. (2003)	Fixed CO-to-H_2 conversion
Unobscured $\Sigma_{\rm SFR}$	FUV	*GALEX* NGS	Gil de Paz et al. (2007)	
Embedded $\Sigma_{\rm SFR}$	24 μm	SINGS	Kennicutt et al. (2003)	
Σ_*	3.6 μm	SINGS	Kennicutt et al. (2003)	$\Upsilon_\star^K = 0.5\ M_\odot/L_{\odot,K}$
Kinematics	21 cm line	THINGS	de Blok et al. (2008)	Simple functional fit; fixed $\sigma_{\rm gas}$

Table 4
Properties of Sample Galaxies

Galaxy	Dist. (Mpc)	i (°)	P.A. (°)	Morph.	M_B (mag)	r_{25} (kpc)	$v_{\rm flat}$ (km s^{-1})	$l_{\rm flat}$ (kpc)	log M_* ($M_\odot$)	log $M_{\rm HI}$ ($M_\odot$)	log $M_{\rm H2}$ ($M_\odot$)	SFR ($M_\odot$ yr^{-1})	l_* (kpc)	$l_{\rm SFR}$ (kpc)	$l_{\rm CO}$ (kpc)
DDO 154	4.3	66	230	Irr	−14.4	1.2	50	2.0	7.1	8.7	⩽6.8	0.005	0.8	1.0	...
Ho I	3.8	12	50	Irr	−14.9	1.8	53	0.4	7.4	8.3	⩽7.2	0.009	0.8	1.2	...
Ho II	3.4	41	177	Irr	−16.9	3.7	36	0.6	8.3	8.9	⩽7.6	0.048	1.2	1.3	...
IC 2574	4.0	53	56	Irr	−18.0	7.5	134	12.9	8.7	9.3	⩽7.9	0.070	2.1	4.8	...
NGC 4214	2.9	44	65	Irr	−17.4	2.9	57	0.9	8.8	8.7	7.0	0.107	0.7	0.5	...
NGC 2976	3.6	65	335	Sc	−17.8	3.8	92	1.2	9.1	8.3	7.8	0.087	0.9	0.8	1.2
NGC 4449	4.2	60	230	Irr	−19.1	2.8	...	...	9.3	9.2	6.9[a]	0.371	0.9	0.8	...
NGC 3077	3.8	46	45	Sd	−17.7	3.0	...	...	9.3	9.1	6.5[a]	0.086	0.7	0.3	...
NGC 7793	3.9	50	290	Scd	−18.7	6.0	115	1.5	9.5	9.1	...	0.235	1.3	1.3	...
NGC 2403	3.2	63	124	SBc	−19.4	7.3	134	1.7	9.7	9.5	7.3	0.382	1.6	2.0	1.9
NGC 0925	9.2	66	287	SBcd	−20.0	14.2	136	6.5	9.9	9.8	8.4	0.561	4.1	4.1	...
NGC 0628	7.3	7	20	Sc	−20.0	10.4	217	0.8	10.1	9.7	9.0	0.807	2.3	2.4	2.4
NGC 3198	13.8	72	215	SBc	−20.7	13.0	150	2.8	10.1	10.1	8.8	0.931	3.2	3.4	2.7
NGC 3184	11.1	16	179	SBc	−19.9	11.9	210	2.8	10.3	9.6	9.2	0.901	2.4	2.8	2.9
NGC 4736	4.7	41	296	Sab	−20.0	5.3	156	0.2	10.3	8.7	8.6	0.481	1.1	0.9	0.8
NGC 3351	10.1	41	192	SBb	−19.7	10.6	196	0.7	10.4	9.2	9.0	0.940	2.2	1.8	2.5
NGC 6946	5.9	33	243	SBc	−20.9	9.8	186	1.4	10.5	9.8	9.6	3.239	2.5	2.7	1.9
NGC 3627	9.3	62	173	SBb	−20.8	13.9	192	1.2	10.6	9.0	9.1	2.217	2.8	1.9	2.2
NGC 5194	8.0	20	172	SBc	−21.1	9.0	219	0.8	10.6	9.5	9.4	3.125	2.8	2.4	2.3
NGC 3521	10.7	73	340	SBbc	−20.9	12.9	227	1.4	10.7	10.0	9.6	2.104	2.9	3.1	2.2
NGC 2841	14.1	74	153	Sb	−21.2	14.2	302	0.6	10.8	10.1	8.5	0.741	4.0	5.3	...
NGC 5055	10.1	59	102	Sbc	−20.6	17.4	192	0.7	10.8	10.1	9.7	2.123	3.2	3.1	3.1
NGC 7331	14.7	76	168	SAb	−21.7	19.6	244	1.3	10.9	10.1	9.7	2.987	3.3	4.5	3.1

Notes.
[a] Unless noted log $M_{\rm H2}$ comes from HERACLES (Leroy et al. 2008) or BIMA SONG (Helfer et al. 2003). NGC 3077 is from Walter et al. (2001) and NGC 4449 is from Bolatto et al. (2008). Upper limits are at 5σ significance.

take the vertical and radial velocity dispersions to be related by $\sigma_{*,z} = 0.6\sigma_{*,r}$.

Stellar Surface Density (Appendix C). We estimate the stellar surface density, Σ_*, from *Spitzer* 3.6 μm maps, mostly from SINGS (Kennicutt et al. 2003). To avoid contamination by hot dust and foreground stars, we construct radial profiles only, using the median 3.6 μm intensity in each tilted ring. We convert from 3.6 μm intensity to Σ_* via an empirical K-to-3.6 μm calibration and adopt a fixed K-band mass-to-light ratio, $\Upsilon_\star^K = 0.5\ M_\odot/L_{\odot,K}$.

SFR Surface Density (Appendix D). We combine FUV and 24 μm maps to derive maps of $\Sigma_{\rm SFR}$, giving us a tracer sensitive to both exposed and dust-embedded star formation. The FUV data come from the *GALEX* Nearby Galaxies Survey (Gil de Paz et al. 2007), and the 24 μm maps are part of SINGS. Because this precise combination of data is new, Appendix D includes an extended motivation for how we convert intensity to $\Sigma_{\rm SFR}$.

3.3. Properties of the Sample

Table 4 compiles the integrated properties of each galaxy in our sample. Columns (1)–(7) give basic parameters adopted from other sources: the name of the galaxy; the distance, inclination, and position angle (Walter et al. 2008, except that we adopt $i = 20°$ in NGC 5194); and the morphology, B-band isophotal radius at 25 mag arcsec^{-2} (r_{25}), and B-band absolute magnitude from LEDA (Prugniel & Heraudeau 1998). Columns (8) and (9) give $v_{\rm flat}$ and $l_{\rm flat}$, the free parameters for our rotation curve fit (Appendix B); from these two parameters, one can calculate $v(r_{\rm gal})$ and β. Columns (10)–(13) give the total stellar mass, H I mass, H_2 mass, and SFR from integrating our data within $1.5r_{25}$.

Columns (14)–(17) give scale lengths derived from exponential fits to the Σ_*, $\Sigma_{\rm SFR}$, and $\Sigma_{\rm H_2}$ (CO) radial profiles. The stellar scale lengths match those found by Tamburro et al. (2008b) with 15% scatter; they are ∼10% shorter than those found by Regan et al. (2001), with a root mean square (rms) scatter of 20%. Our CO scale lengths are taken from Leroy et al. (2008); these are ∼30% shorter than those of Regan et al. (2001) on average.

3.4. Methodology

We work with maps of $\Sigma_{\rm H\,I}$, $\Sigma_{\rm H_2}$, and $\Sigma_{\rm SFR}$ on the THINGS astrometric grid. All data are placed at a common spatial

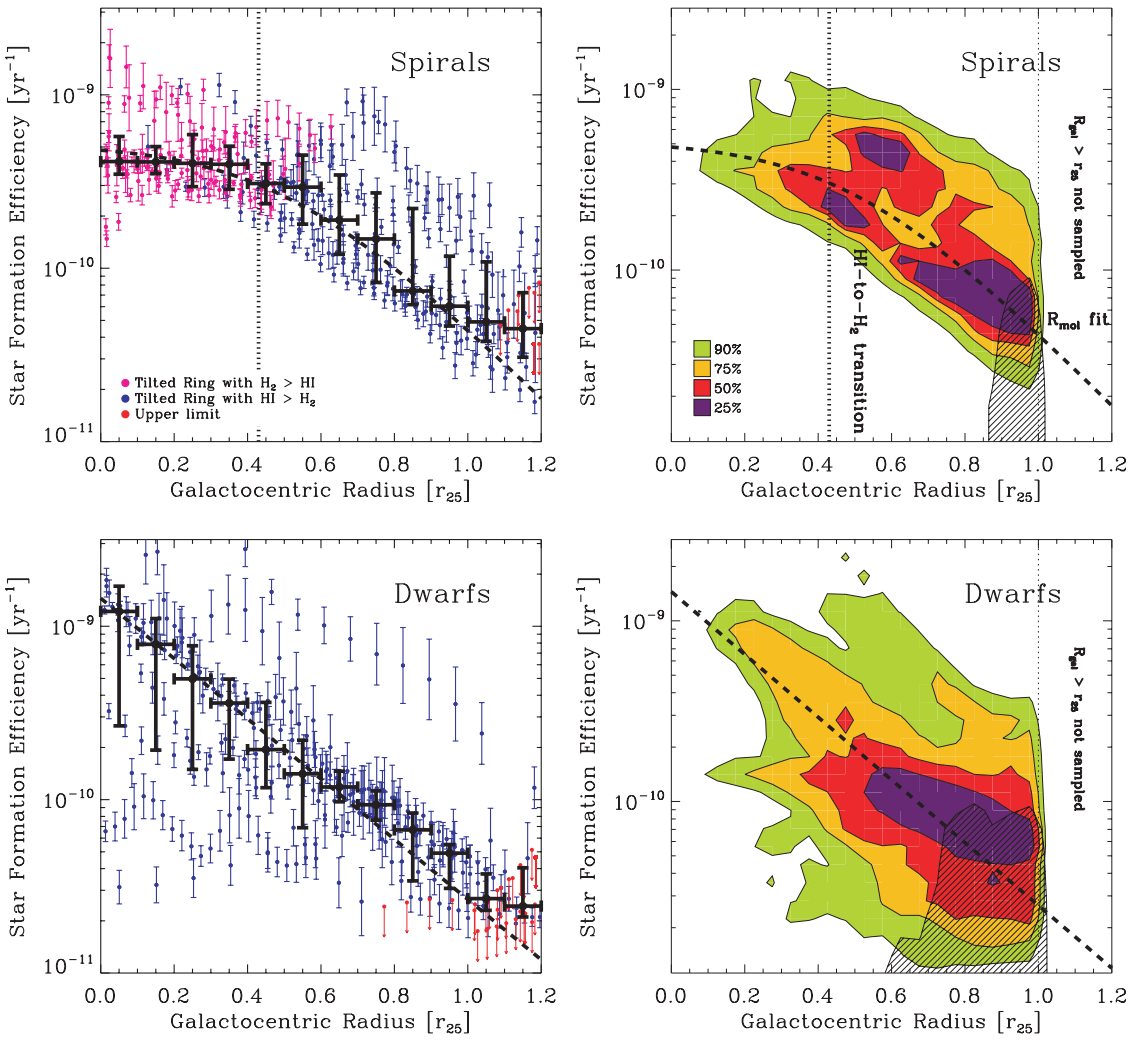

Figure 1. SFE as a function of galactocentric radius in spiral (top row) and dwarf (bottom row) galaxies. The left panels show results for radial profiles; each point shows the average SFE over a 10″ wide tilted ring; magenta points are H_2-dominated ($\Sigma_{H_2} > \Sigma_{HI}$), blue points are H I-dominated ($\Sigma_{H_2} < \Sigma_{HI}$), and red arrows indicate upper limits. The right panels show data for individual LOSs. We give equal weight to each galaxy and choose contours that include 90%, 75%, 50%, and 25% of the data. The hatched regions indicate where we are incomplete. The top panels show a nearly fixed SFE in H_2-dominated galaxy centers (magenta). Where H I dominates the ISM (blue), we observe the SFE to decline exponentially with radius; the thick dashed lines show fits of SFE to r_{gal} (Equations 22 and 23). The vertical dotted line in the upper panels shows r_{gal} at the H I-to-H_2 transition in spirals, $0.43 \pm 0.18 r_{25}$ (Section 5.2).

resolution of 400 pc for dwarf galaxies and 800 pc for spirals; when necessary, we use a Gaussian kernel to degrade our data to this resolution. The convolution occurs before any deprojection and may be thought of as placing each subsample at a single distance. Radial profiles of these maps and Σ_* appear in Appendix E.

Using these data, we compute each quantity in Table 1 for each pixel inside $1.2r_{25}$ and derive radial profiles over the same range following the methodology in Appendix E. Because we measure Σ_* and $v(r_{gal})$ only in radial profile, these maps are often a hybrid between radial profiles and pixel-by-pixel measurements.

In Sections 4–6, we analyze the combined data set for the two subsamples and avoid discussing results for individual galaxies. We refer readers interested in individual galaxies to the Appendices. Appendix E gives our radial profile data and the atlas in Appendix F shows maps of Σ_{H_I}, Σ_{H_2}, total gas, unobscured Σ_{SFR}, dust-embedded Σ_{SFR}, and total Σ_{SFR}, as well as profiles of the quantities in Table 1.

In keeping with our emphasis on the combined dataset, we default to quoting the mean and 1σ scatter when we give uncertainties in parameters derived from the ensemble of galaxies (we usually estimate the scatter using the median absolute deviation to reduce sensitivity to outliers). We prefer this approach to giving the uncertainty in the mean because we are usually interested in how well a given number describes our whole sample, and not how precisely we have measured the mean.

4. RESULTS

Here we present our main observational results: how the SFE varies as a function of other quantities. In Section 4.1, we begin by showing the SFE as a function of three basic parameters: galactocentric radius, stellar surface density, and gas surface density. Then in Section 4.2, we look at SFE as a function of the laws described in Section 2.1. Finally, in Section 4.3 we show the SFE as a function of the thresholds described in Section 2.2.

We present these results as a series of plots that each show SFE as a function of another quantity. These all follow the format seen in Figure 1, where we show SFE (y-axis) versus galactocentric radius (x-axis), normalized to the optical radius, r_{25}. We separately plot the subsamples of spiral (top row) and dwarf galaxies (bottom row).

On the left, we show results for radial profiles. Each point shows the average SFE over one 10″ wide tilted ring in one galaxy. The color indicates whether the ISM averaged over the ring is mostly (> 50%) H I (blue) or H_2 (magenta). Thick black crosses show all data binned into a single trend. For each bin, we plot the median, 50% range (*y*-error bar), and bin width (*x*-error bar; here, $0.1r_{25}$).

On the right, we again show SFE as a function of radius, this time calculated for each LOS. We co-add all galaxies, giving equal weight to each, and pick contours that contain 90% (green), 75% (yellow), 50% (red), and 25% (purple) of the resulting data. Most numerical results use the annuli, which are easier to work with; these pixel-by-pixel plots verify that conclusions based on rings hold pixel by pixel down to kiloparsec scales.

We do not analyze data with $\Sigma_{\rm gas} < 1\ M_\odot\ {\rm pc}^{-2}$ because the SFE is not well determined for low gas surface densities. That is, we only address the question "where there is gas, is it good at forming stars?" Data with $\Sigma_{\rm SFR} < 10^{-4}\ M_\odot\ {\rm yr}^{-1}\ {\rm kpc}^{-2}$ are treated as upper limits. These are red arrows in the radial profile plots. In the pixel-by-pixel plots, hatched regions show the area inhabited by 95% of the data with $\Sigma_{\rm SFR} \leqslant 10^{-4}\ M_\odot\ {\rm yr}^{-1}\ {\rm kpc}^{-2}$, that is, the hatched regions indicate the area where we are incomplete. In the pixel-by-pixel plots, we include data out to r_{25}, while we plot radial profile data out to $1.2r_{25}$.

4.1. SFE and Other Basic Quantities

4.1.1. SFE and Radius

In Section 1, we argued that a critical observation for theories of galactic-scale star formation is that the SFE declines in the outer parts of spiral galaxies. Figure 1 shows this via plots of SFE against galactocentric radius (normalized to r_{25}) in our two subsamples.

In spiral galaxies (top row), the SFE is nearly constant where the ISM is mostly H_2 (magenta), which agrees with our observation of a linear relationship between Σ_{H_2} and $\Sigma_{\rm SFR}$ in Bigiel et al. (2008). Typically, the ISM is equal parts of H I and H_2 at $r_{\rm gal} = 0.43 \pm 0.18 r_{25}$ (Section 5.2). Outside this transition, the SFE decreases steadily with increasing radius. This decline continues to $r_{\rm gal} \gtrsim r_{25}$, the limit of our data. This is similar, though not identical, to the observation by Kennicutt (1989) and Martin & Kennicutt (2001) that star formation is not widespread beyond a certain radius.

The SFE in spirals can be reasonably described in two ways. First, a constant SFE in the inner parts of galaxies followed by a break at $0.4r_{25}$ (slightly inside the transition to a mostly-H I ISM):

$$\mathrm{SFE} = \begin{cases} 4.3 \times 10^{-10} & r_{\rm gal} < 0.4r_{25} \\ 2.2 \times 10^{-9} \exp\left(\dfrac{-r_{\rm gal}}{0.25r_{25}}\right) & r_{\rm gal} > 0.4r_{25} \end{cases} \ {\rm yr}^{-1}. \quad (21)$$

Alternatively, we can adopt Equation (8), appropriate for a fixed SFE (H_2), and derive the best-fit exponential relating $R_{\rm mol}$ to $r_{\rm gal}$:

$$\mathrm{SFE} = 5.25 \times 10^{-10} \frac{R_{\rm mol}}{R_{\rm mol}+1}\ {\rm yr}^{-1}, \qquad R_{\rm mol} = 10.6 \exp(-r_{\rm gal}/0.21r_{25}), \quad (22)$$

which appears as a thick dashed line in the upper panels of Figure 1. The two fits reproduce the observed SFE with similar accuracy; the scatter about each is ≈ 0.26 dex, slightly better than a factor of 2.

In dwarf galaxies (lower panels), we observe a steady decline in the SFE with increasing radius for all $r_{\rm gal}$, approximately described by

$$\mathrm{SFE} = 1.45 \times 10^{-9} \exp(-r_{\rm gal}/0.25r_{25})\ {\rm yr}^{-1} \quad (23)$$

with ∼0.4 dex scatter about the fit, that is, a factor of 2–3.

In dwarfs, we take $\Sigma_{\rm gas} \approx \Sigma_{\rm H\,I}$, so that $\mathrm{SFE} = \Sigma_{\rm SFR}/\Sigma_{\rm H\,I}$. For comparison with Equation (22), however, we rewrite Equation (23) *assuming* that SFE (H_2) $= 5.25 \times 10^{-10}\ {\rm yr}^{-1}$, the value measured in spirals. In terms of $R_{\rm mol}$, Equation (23) becomes

$$\mathrm{SFE} = \frac{\Sigma_{\rm SFR}}{\Sigma_{\rm H\,I}} = 5.25 \times 10^{-10}\ R_{\rm mol}\ {\rm yr}^{-1}, \qquad R_{\rm mol} = 2.76 \exp(-r_{\rm gal}/0.25r_{25}). \quad (24)$$

The outer parts of dwarfs, $r_{\rm gal} \gtrsim 0.4r_{25}$, appear similar to the outer disks of spiral galaxies in Figure 1. Surprisingly, however, we find the SFE to be *higher* in the central parts of dwarf galaxies than in the molecular gas of spirals. A higher SFE in dwarf galaxies is quite unexpected. Their lower metallicities, more intense radiation fields, and weaker potential wells should make gas *less* efficient at forming stars. A simple explanation for the high observed SFE is the presence of a significant amount of H_2. Figure 1 assumes that $\Sigma_{\rm gas} \approx \Sigma_{\rm H\,I}$ in dwarfs. If we miss a significant amount of H_2 along a LOS, we will overestimate the SFE because we underestimate $\Sigma_{\rm gas}$. We quantify the possibility of substantial H_2 in dwarfs in Section 5.3, but the magnitude of the effect can be directly read from Equation (24). At $r_{\rm gal} = 0$, if dwarf galaxies have the same SFE (H_2) as spirals, $R_{\rm mol} \approx 2.76$, that is, $\Sigma_{H_2} \approx 2.76\Sigma_{\rm H\,I}$.

4.1.2. SFE and Stellar Surface Density

Galactocentric radius is probably not intrinsically important to a local process like star formation, but Figure 1 suggests that local conditions covariant with radius have a large effect on the ability of gas to form stars. The radius, r_{25}, that we use to normalize the *x*-axis is defined by an optical isophote and thus measures stellar light. Therefore, r_{25} is closely linked to the stellar distribution.

Figure 2 shows this link directly. We plot the stellar scale length, l_*, measured via an exponential fit to the 3.6 μm profile as a function of r_{25} for our spiral subsample. We see that $r_{25} = (4.6 \pm 0.8) l_*$ and that we could have equivalently normalized the *x*-axis in Figure 1 by l_*. We may then suspect that the stellar surface density, Σ_*, underlies the well-defined relation between SFE and $r_{\rm gal}$ observed in Figure 1.

In Figure 3, we explore this connection by plotting SFE as a function of Σ_*. In both spiral and dwarf galaxies, we see a nearly linear relationship between SFE and Σ_* where the ISM is H I-dominated (blue points).

A basic result of THINGS is that over the optical disk of most star forming galaxies, the H I surface density varies remarkably little (Appendices E and F and Walter et al. 2008). Inspecting our atlas, one sees that $\Sigma_{\rm H\,I} \approx 6\ M_\odot\ {\rm pc}^{-2}$ (within a factor of 2) over a huge range of local conditions, including most of the optical disk in most galaxies. Because $\Sigma_{\rm gas}$ is nearly constant in the H I-dominated (blue) regime, SFE $\propto \Sigma_*$ approximately defines a line of fixed specific SFR (SSFR), that is, SFR per unit stellar mass.

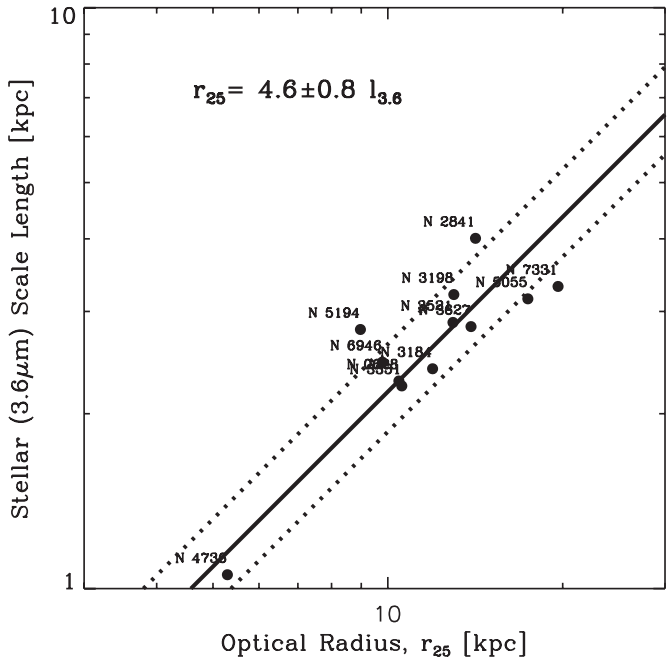

Figure 2. Stellar scale length, l_*, as a function of isophotal radius, r_{25}. Solid and dashed lines show $r_{25} = (4.6 \pm 0.8) l_*$.

The inverse of the SSFR is the stellar assembly time, $\tau_* = \Sigma_*/\Sigma_{SFR}$. This is the time required for the present SFR to build up the observed stellar disk. In our spiral subsample, the mean $\log_{10} \tau_* \approx 10.5 \pm 0.3$, that is, 3.2×10^{10} years or slightly more than 2 Hubble times. Dwarf galaxies have shorter assembly times, $\log_{10} \tau_* \approx 10.2 \pm 0.3$ years, about a Hubble time (dashed lines in Figure 3 show these values using average values of $\Sigma_{\rm gas}$ for each subsample). Taking these numbers at face value, dwarfs are forming stars at about their time-average rate, while spirals are presently forming stars at just under half of their average rate.

We *only* observe SFE $\propto \Sigma_*$ where the ISM is mostly H I. Where the ISM is mostly H_2 in spirals galaxies, we observe a constant SFE at a range of Σ_*; similar to the constancy as a function of $r_{\rm gal}$ observed in the inner parts of spirals (Figure 1). The transition between these two regimes occurs at $\Sigma_* = 81 \pm 25\ M_\odot\ {\rm pc}^{-2}$ (Section 5.2) in spirals. In dwarfs, LOSs with Σ_* above this transition value exhibit systematically high SFE, lending further, albeit indirect, support to the idea that these points correspond to unmeasured H_2.

Figures 1 and 3 show that where the ISM is mostly H_2, the SFR per unit of *gas* (SFE) is nearly constant and that where the ISM is mostly H I, the SFR per unit of *stellar mass* (SSFR) is nearly constant. Together these observations suggest that H_2,

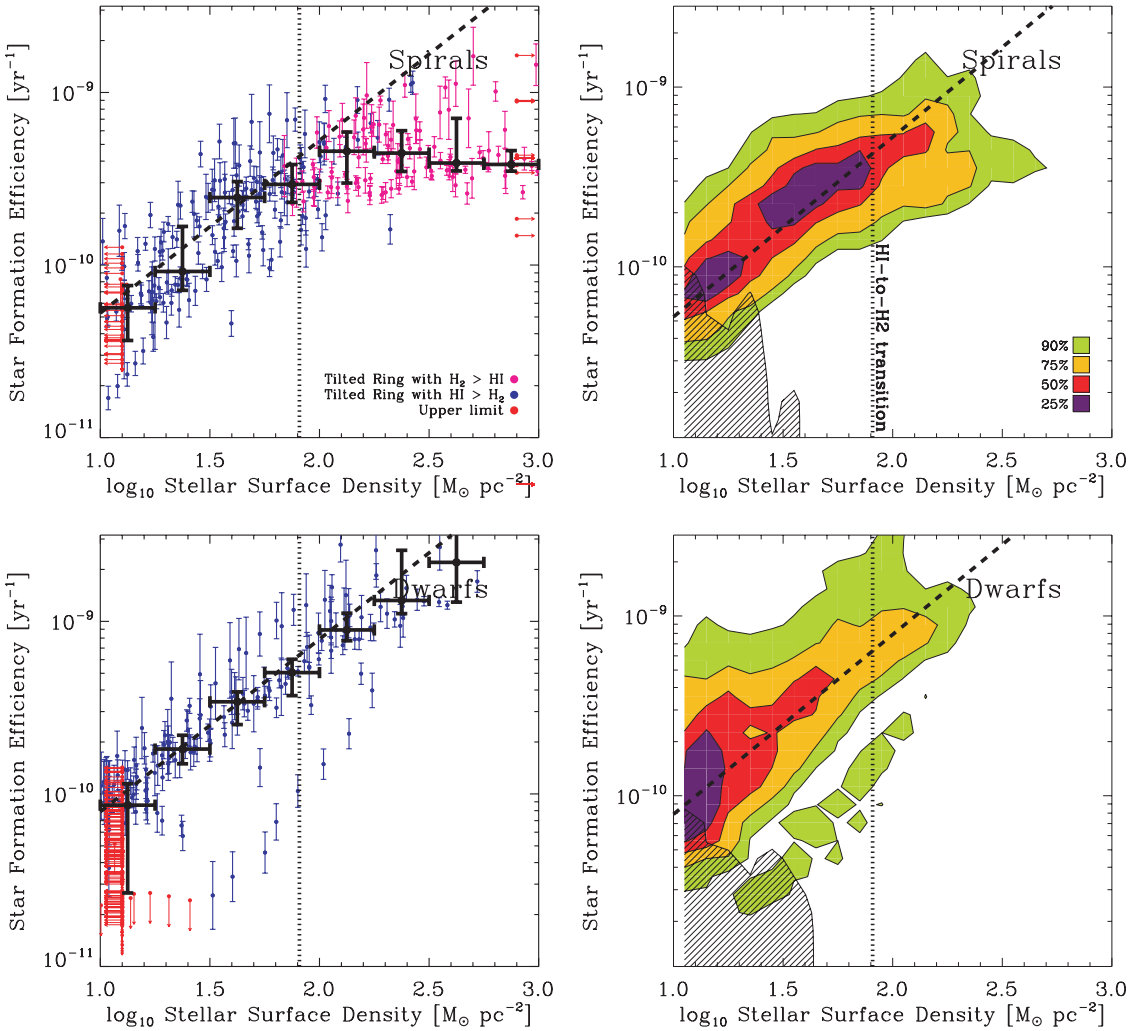

Figure 3. SFE as a function of stellar surface density, Σ_*, in spiral (top row) and dwarf (bottom row) galaxies. Conventions and symbols are as in Figure 1. Dashed diagonal lines show the linear relationship between SFE and Σ_* expected for the mean stellar assembly time and $\Sigma_{\rm gas}$ for each subsample. Vertical dotted lines show Σ_* where the ISM is equal parts of H I and H_2 in spirals (Section 5.2), $\Sigma_* = 81 \pm 25\ M_\odot\ {\rm pc}^{-2}$.

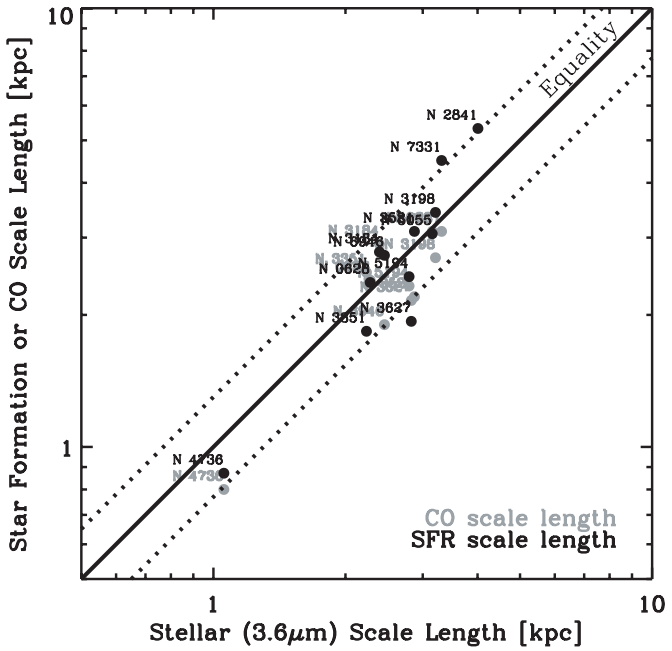

Figure 4. Scale lengths of star formation (black) and CO (gray) as a function of the stellar scale length (*x*-axis). All three scale lengths are similar, the dashed lines show slope unity and ±30% (the approximate scatter in the data).

stars, and star formation have similar structure with all three embedded in a relatively flat distribution of H I. Figure 4 shows that the scale lengths of these three distributions are, in fact, comparable. The SFR (black) and CO (gray) scale lengths of spiral galaxies are both roughly equal to the stellar scale length:

$$l_{\rm CO} = (0.9 \pm 0.2) l_* \quad \text{and} \quad l_{\rm SFR} = (1 \pm 0.2) l_*. \qquad (25)$$

Regan et al. (2001) also found that $l_{\rm CO} \approx l_*$ comparing *K*-band maps to BIMA SONG and Young et al. (1995) found $l_{\rm CO} \approx 0.2 r_{25}$, which is almost identical to our $l_{\rm CO} \sim 0.9 l_*$ and $(4.6 \pm 0.8) l_* = r_{25}$.

4.1.3. SFE and Gas Surface Density

This link between Σ_* and the SFE is somewhat surprising because it is common to view $\Sigma_{\rm SFR}$, and thus the SFE, as set largely by $\Sigma_{\rm gas}$ alone over much of the disk of a galaxy (following, e.g., Kennicutt 1998a). In Figure 5, we show this last slice through SFR-stars-gas parameter space, plotting SFE as a function of $\Sigma_{\rm gas}$.

As in Figures 1 and 3, we observe two distinct regimes. In spirals, where $\Sigma_{\rm gas} > 14 \pm 6\, M_\odot$ pc^{-2} (Section 5.2), the ISM is mostly H_2 and we observe a fixed SFE. This $\Sigma_{\rm gas}$, shown by a vertical dotted line, corresponds approximately to both the $N(H) \sim 10^{21}$ cm^{-2} star formation threshold noted by Skillman (1987) and the saturation value for H I observed by, for example, Martin & Kennicutt (2001) and Wong & Blitz (2002) (and seen strikingly in THINGS at $\Sigma_{\rm gas} = 12\, M_\odot$ pc^{-2} by Bigiel et al. 2008, who quote $\Sigma_{\rm gas} = 9\, M_\odot$ pc^{-2} but do not include helium).

In contrast to $r_{\rm gal}$ and Σ_*, $\Sigma_{\rm gas}$ does not exhibit a clear correlation with the SFE where the ISM is mostly H I. Instead, over the narrow range $\Sigma_{\rm gas} \approx$ 5–10 $M_\odot$ pc^{-2}, the SFE varies from $\sim 3 \times 10^{-11}$ to 10^{-9} yr^{-1}. We see little evidence that $\Sigma_{\rm H\,I}$ plays a central role regulating the SFE in either spirals or dwarfs. Rather, the most striking observation in Figure 5 is that $\Sigma_{\rm H\,I}$ exhibits a narrow range of values over the optical disk and is therefore itself likely subject to some kind of regulation.

The possibility of a missed reservoir of molecular gas in dwarfs is again evident from the lower panels in Figure 5. A subset of data has SFE higher than that observed for H_2 in spirals and just to the left of the H I saturation value. If H_2 were added to these points, they would move down (as the SFE decreases) and to the right (as $\Sigma_{\rm gas}$ increases), potentially yielding a data distribution similar to that we observe in spirals.

4.2. SFE and Star Formation Laws

We now ask whether the star formation laws proposed in Section 2.1 can explain the radial decline in SFE and whether SFE(H_2), already observed to be constant as a function of $r_{\rm gal}$, Σ_*, and $\Sigma_{\rm gas}$ (but with some scatter), exhibits *any* kind of systematic behavior. We compare the SFE to four quantities that drive the predictions in Table 1: gas surface density (already seen in Figure 5), gas pressure (density), the orbital timescale, and the derivative of the rotation curve, β.

4.2.1. Free-Fall Time in a Fixed Scale Height Disk

A dashed line in Figure 5 illustrates SFE $\propto \Sigma_{\rm gas}^{0.5}$, expected if the SFE is proportional to the free-fall time in a fixed scale height gas disk (similar to the Kennicutt–Schmidt law; Kennicutt 1998a). The normalization matches the H_2-dominated parts of spirals and roughly bisects the range of SFE observed for dwarfs, but large areas have much lower SFE than one would predict from this relation. Adjusting the normalization can move the line up or down but cannot reproduce the distribution of data observed in Figure 5.

The culprit here is the small dynamic range in $\Sigma_{\rm H\,I}$. Because $\Sigma_{\rm H\,I}$ does not vary much across the disk, while the SFE does, the free-fall time in a fixed scale height disk, or any other weak dependence of SFE on $\Sigma_{\rm gas}$ alone, cannot reproduce variations in the SFE where the ISM is mostly H I. A quantity other than $\Sigma_{\rm gas}$ must play an important role at radii as low as $\sim 0.5 r_{25}$ (a fact already recognized by Kennicutt 1989, among others).

4.2.2. Free-Fall Time in a Variable Scale Height Gas Disk; Pressure and ISM Phase

In Section 4.1, we saw that where the ISM is mostly H I, the SFE correlates better with Σ_* than with $\Sigma_{\rm gas}$. This might be expected if the stellar potential well plays a central role in setting the *volume* density of the gas, $\rho_{\rm gas}$, because Σ_* varies much more strongly with radius than $\Sigma_{\rm H\,I}$. In Section 2, we presented two predictions relating SFE to $\rho_{\rm gas}$: that the timescale over which GMCs form depends on the $\tau_{\rm ff}$, the free-fall time in a gas disk with a scale height set by hydrostatic equilibrium,[9] and that the ratio $R_{\rm mol} = \Sigma_{\rm H_2}/\Sigma_{\rm H\,I}$ primarily depends on midplane gas pressure, $P_{\rm h}$.

Under our assumption of a fixed $\sigma_{\rm gas}$, $P_{\rm h} \propto \rho_{\rm gas}$ and both predictions can be written as a power law relating SFE or $R_{\rm mol}$ to $P_{\rm h}$. In Figure 6, we plot SFE as a function of $\rho_{\rm gas}$ and $P_{\rm h}$ (top and bottom *x*-axis), estimated from hydrostatic equilibrium (Equation 9).

Where the ISM is mostly H_2 (magenta points) in spirals (top row), we observe no clear relationship between $P_{\rm h}$ and SFE, further evidence that SFE (H_2) is largely decoupled from global conditions in the ISM in our data.

Where the ISM is mostly H I (blue points) in dwarf galaxies and the outer parts of spirals, the SFE correlates with $P_{\rm h}$.

[9] Hereafter, $\tau_{\rm ff}$ refers only to the free-fall time in a gas disk with a scale height set by hydrostatic equilibrium.

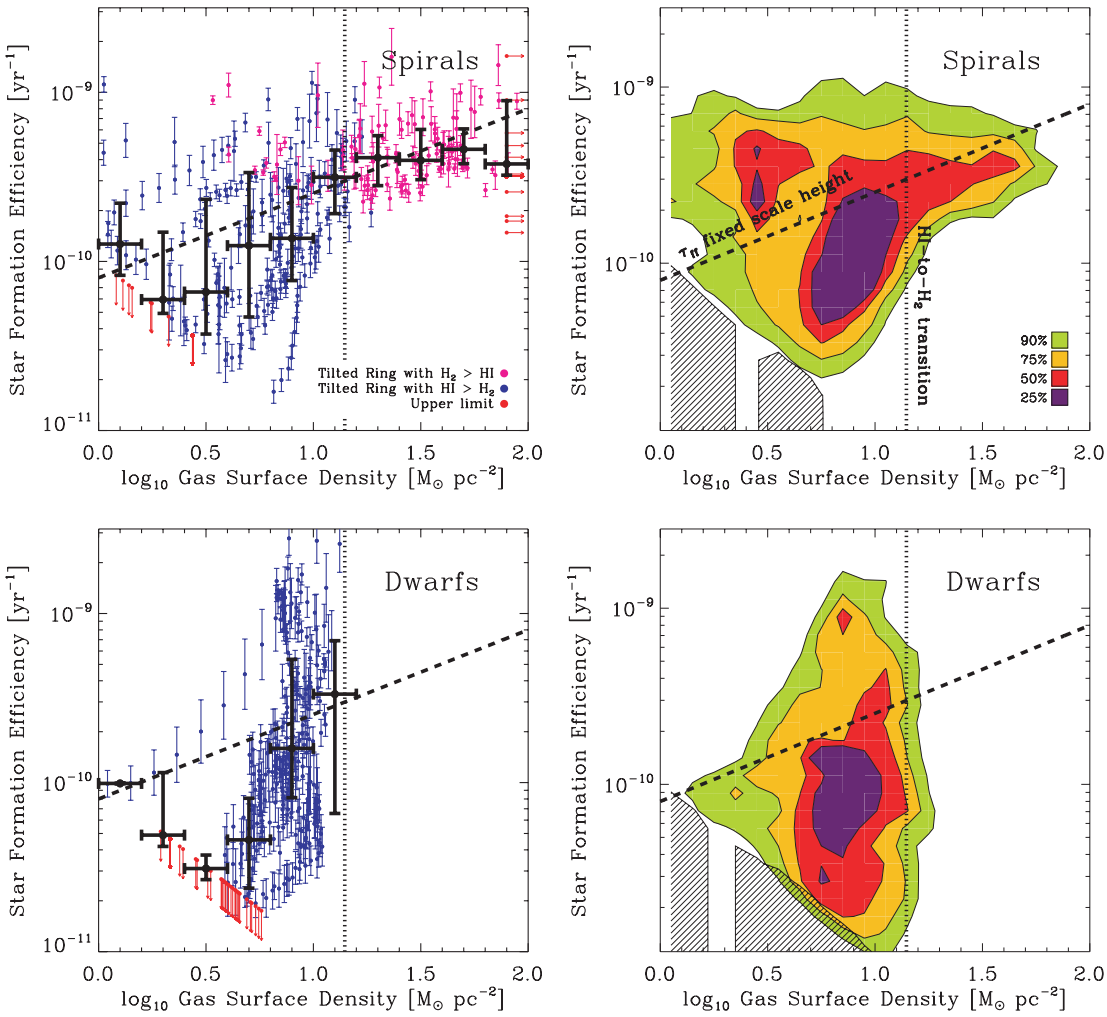

Figure 5. SFE as a function of Σ_{gas} in spiral (top row) and dwarf (bottom row) galaxies. Conventions and symbols are the same as in Figure 1. The vertical dotted line shows Σ_{gas} at the H I-to-H_2 transition in spirals (Section 5.2), $\Sigma_{gas} = 14 \pm 6\ M_\odot\ pc^{-2}$. The dashed line shows the SFE proportional to the free-fall time in a fixed scale height disk. Clearly, the line cannot describe both high and low SFE data, even if the normalization is adjusted, and so changes in this timescale cannot drive the radial decline that we observe in the SFE.

P_h predicts the SFE notably better than Σ_{gas} in this regime, supporting the idea that the volume density of gas (at least H I) is more relevant to star formation than surface density. Wong & Blitz (2002) and Blitz & Rosolowsky (2006) observed a continuous relationship between R_{mol} and P_h, mostly where $\Sigma_{H_2} \gtrsim \Sigma_{HI}$. Figure 6 suggests that such a relationship extends well into the regime where H I dominates the ISM.

The solid line in Figure 6 illustrates the case of 1% of the gas formed into stars per τ_{ff}(SFE $\propto \rho_{gas}^{0.5}$), a typical value at the H I-to-H_2 transition in spirals (Section 5.2). Adjusting the normalization slightly, such a line can intersect both the high and low ends of the observed SFE in spirals, but predicts variations in SFE (H_2) that we do not observe and is too shallow to describe dwarf galaxies.

The dash-dotted line shows $R_{mol} \propto \tau_{ff}^{-1} \propto P_h^{0.5}$, expected for GMC formation over a free-fall time. In dwarf galaxies, where we take $\Sigma_{gas} = \Sigma_{HI}$, this is equivalent to SFE$\propto \tau_{ff}^{-1}$. This description can describe spirals at high and intermediate P_h, but is too shallow to capture the drop in SFE at large radii in spirals and across dwarf galaxies. If τ_{ff} is the characteristic timescale for GMC formation, effects other than just an increasing timescale must suppress cloud formation in these regimes.

A dashed line shows the steeper dependence, $R_{mol} \propto P_h^{1.2}$, expected for low R_{mol} based on modeling by Elmegreen (1993). This may be a reasonable description of both spiral and dwarf galaxies (note that at high SFE, P_h may be underestimated in dwarf galaxies because we fail to account for H_2). We explore how P_h relates to R_{mol} more in Section 5.

4.2.3. Orbital Timescale

The orbital timescale, τ_{orb}, varies strongly with radius, and Kennicutt (1998a) found τ_{orb} to be a good predictor of disk-averaged SFE. In Figure 7, we plot SFE as a function of τ_{orb} in our sample.

The solid line shows 6% of the gas converted to stars per τ_{orb} and is a reasonable match to spirals near the H I-to-H_2 transition (vertical dotted line). This value agrees with the range of efficiencies found by Wong & Blitz (2002) and with Kennicutt (1998a), who found $\approx$ 7% of gas converted to stars per τ_{orb} averaged over galaxy disks (converted to our adopted initial mass function, IMF). Like Wong & Blitz (2002), we do not observe a clear correlation between SFE and τ_{orb} where the ISM is mostly H_2.

Where the ISM is mostly H I (blue points), the SFE clearly anticorrelates with τ_{orb} in both spiral and dwarf galaxies. However, we do not observe a constant efficiency per τ_{orb}. In both subsamples, SFE drops faster than τ_{orb} increases, so that data at large radii (longer τ_{orb}, lower SFE) show lower efficiency

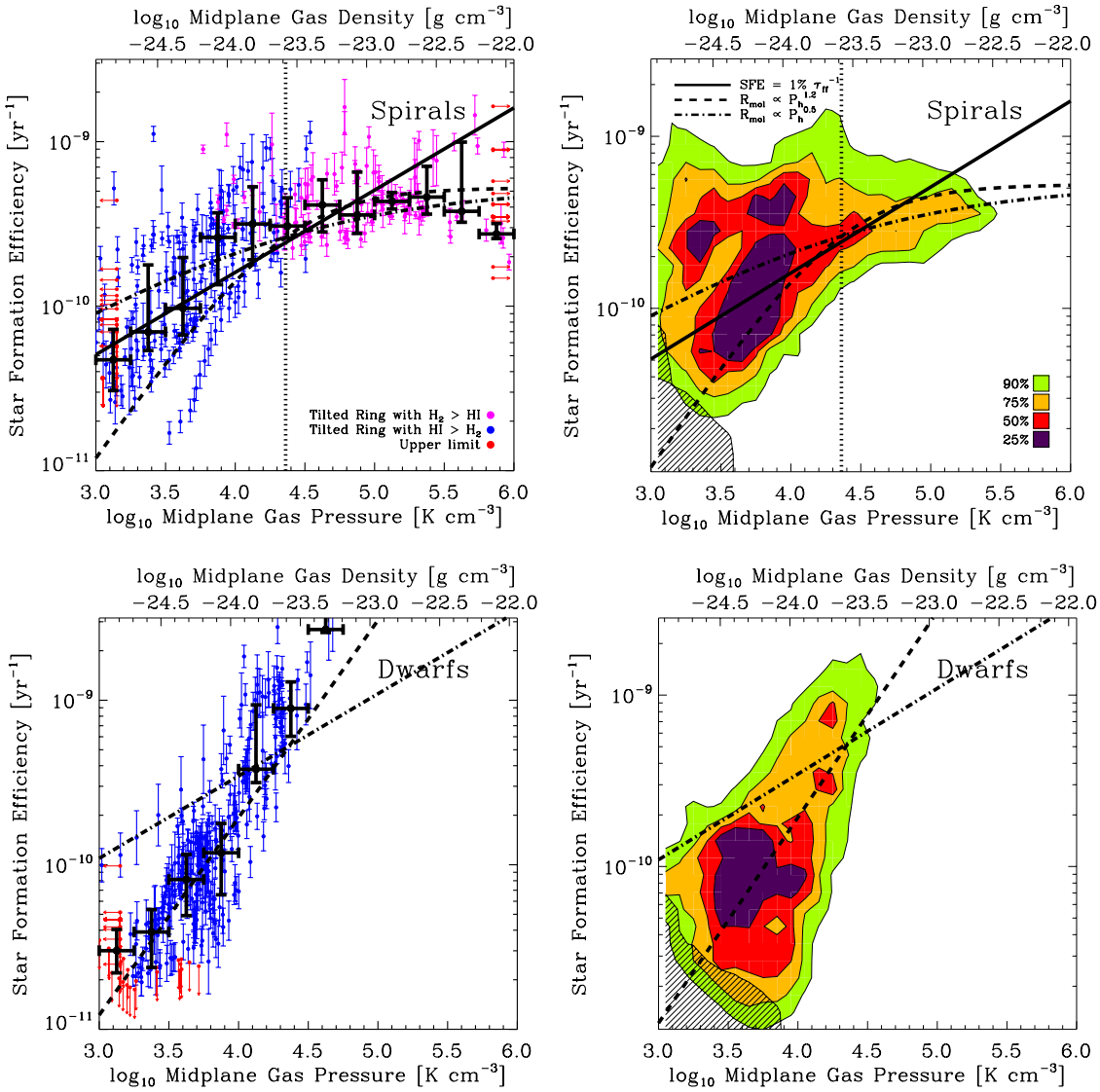

Figure 6. SFE as a function of midplane hydrostatic gas pressure, P_h (bottom x-axis), and equivalent volume density (top x-axis) in spiral (top row) and dwarf (bottom row) galaxies. Conventions follow Figure 1. The vertical line shows P_h at the H I-to-H_2 transition in spirals, $\log_{10} P_h/k_B(\mathrm{K\ cm^{-3}}) \approx 4.36$. The solid line illustrates 1% of gas converted to stars per disk free-fall time. Dash-dotted and dashed lines show $R_{mol} \propto P_h^{0.5}$ (τ_{ff}^{-1}) and $R_{mol} \propto P_h^{1.2}$ (Elmegreen 1993), respectively. For our adopted $\sigma_{gas} = 11$ km s^{-1} and including helium: $\rho(\mathrm{g\ cm^{-3}}) = 1.14 \times 10^{-28}(P_h/k_B)(\mathrm{K\ cm^{-3}})$ and $n(\mathrm{cm^{-3}}) = 4.4 \times 10^{23}\rho(\mathrm{g\ cm^{-3}})$.

per τ_{orb} than those from inner galaxies. Although τ_{orb} correlates with the SFE, the drop in τ_{orb} is not enough on its own to explain the drop in SFE.

We reach the same conclusion if we posit that τ_{orb} is the relevant timescale for GMC formation, so that $R_{mol} \propto \tau_{orb}^{-1}$. The dashed lines in Figure 7 show this relation combined with a fixed SFE (H_2) and normalized to $R_{mol} = 1$ at $\tau_{orb} = (1.8 \pm 0.4) \times 10^8$ yr, which we observe at the H I-to-H_2 transition in spirals (Section 5.2). This dependence is even shallower than SFE $\propto \tau_{orb}^{-1}$ and cannot reproduce the SFE in both inner and outer disks by itself. If τ_{orb} is the relevant timescale for cloud formation, then the fraction of gas that actively forms stars must substantially vary between the middle and the edge of the optical disk.

4.2.4. Derivative of the Rotation Curve, β

Tan (2000) suggested that cloud–cloud collisions regulate the SFE. The characteristic timescale for such collisions is τ_{orb} modified by the effects of galactic shear. In Figure 7, we saw that the SFE of molecular gas is not a strong function of τ_{orb}. Therefore, in Figure 8, we plot the SFE as a function of β, the logarithmic derivative of the rotation curve (we plot SFE against Q_{gas}, the other component of this timescale in Section 4.3.1). This isolates the effect of differential rotation; $\beta = 0$ for a flat rotation curve and $\beta = 1$ for solid body rotation (no shear).

Figure 8 shows a simple relationship between β and SFE in spirals: $\beta > 0$ is associated with high SFE. High β occurs almost exclusively at low radius (where the rotation curve rises steeply) and in these regions, the ISM is mostly H_2 with accordingly high SFE. However, the outer disks of spirals have $\beta \sim 0$ and a wide range of SFE. Beyond the basic relationship, it is unclear that β has utility predicting the SFE. In particular, we see no clear relationship between SFE and β where the ISM is mostly H_2 (magenta points). If collisions between bound clouds regulate the SFE, we would expect an anticorrelation between β and SFE because cloud collisions are more frequent in the presence of greater shear.

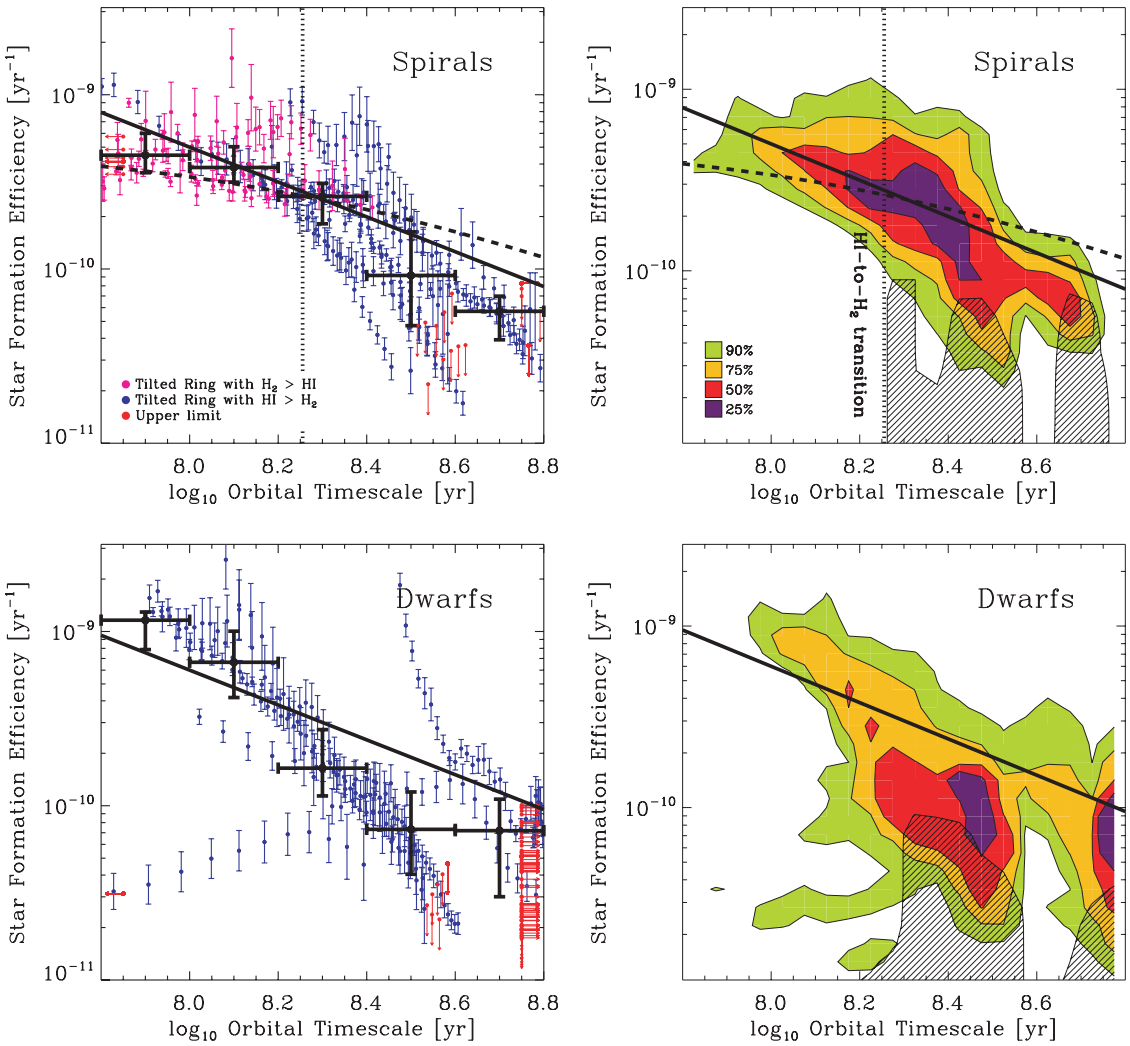

Figure 7. SFE as a function of the orbital timescale, $\tau_{\rm orb}$, in spiral (top row) and dwarf (bottom row) galaxies, following the conventions from Figure 1. The solid line shows 6% of gas converted into stars per $\tau_{\rm orb}$. The dashed line shows the expected SFE if $R_{\rm mol} = \Sigma_{\rm H_2}/\Sigma_{\rm H\,I} \propto \tau_{\rm orb}^{-1}$. The SFE is a well-defined function of $\tau_{\rm orb}$, but the decline in $\tau_{\rm orb}$ alone cannot reproduce the radial decline in SFE or $R_{\rm mol}$.

In dwarf galaxies, increasing β mostly corresponds to increasing SFE. This relationship has the sense of the shear threshold proposed by Hunter et al. (1998a) that where rotation curves are nearly solid body low shear allows clouds to form via instabilities aided by magnetic fields (also see Kim & Ostriker 2001). The rotation curves in dwarf galaxies rise more slowly than those in spirals, leading to $\beta > 0$ over a larger range of radii in dwarf galaxies and limiting $\beta = 0$ to the relative outskirts of the galaxy. A positive correlation between β and SFE is opposite the sense expected if cloud collisions are important: at high β, collisions should be less frequent.

4.3. SFE and Thresholds

The decline in the SFE where the ISM is mostly H I is too dramatic to be reproduced across our whole sample by changes in $\tau_{\rm orb}$ or $\tau_{\rm ff}$ alone. This may be because at large radii, a significant amount of gas is simply unrelated to star formation. If the fraction of gas that is unable to form GMCs increases with radius, the SFE will decline independent of any change in GMC formation time. Here we consider the SFE as a function of proposed star formation thresholds: gravitational instability in the gas alone ($Q_{\rm gas}$) in a disk of gas and stars ($Q_{\rm stars+gas}$), the ability of instabilities to develop before shear destroys them, and the ability of a cold gas phase to form.

First, we plot each threshold as a function of galactocentric radius in spiral (Figure 9) and dwarf galaxies (Figure 10). Individual points correspond to averages over 10″ wide tilted rings. For magenta points, $\Sigma_{\rm H_2} > \Sigma_{\rm H\,I}$ and for blue points, $\Sigma_{\rm H_2} < \Sigma_{\rm H\,I}$. The gray region in each plot shows the nominal condition for instability, that is, where we expect star formation to occur. Red arrows indicate data outside the range of the plot.

We proceed creating plots like Figure 1 for each threshold and comparing them with Figure 9. We expect supercritical gas to exhibit a (dramatically) higher SFE than subcritical gas, where star formation proceeds only in isolated pockets or does not proceed at all.

4.3.1. Gravitational Instability in the Gas Disk

Figure 11 shows SFE as a function of $Q_{\rm gas}$, Toomre's Q parameter for a thin gas disk; the top left panels in Figures 9 and 10 show $Q_{\rm gas}$ as a function of radius.

In each plot, a gray area indicates the theoretical condition for instability. We immediately see that almost no area in our sample is formally unstable. Rather, most LOSs are strikingly

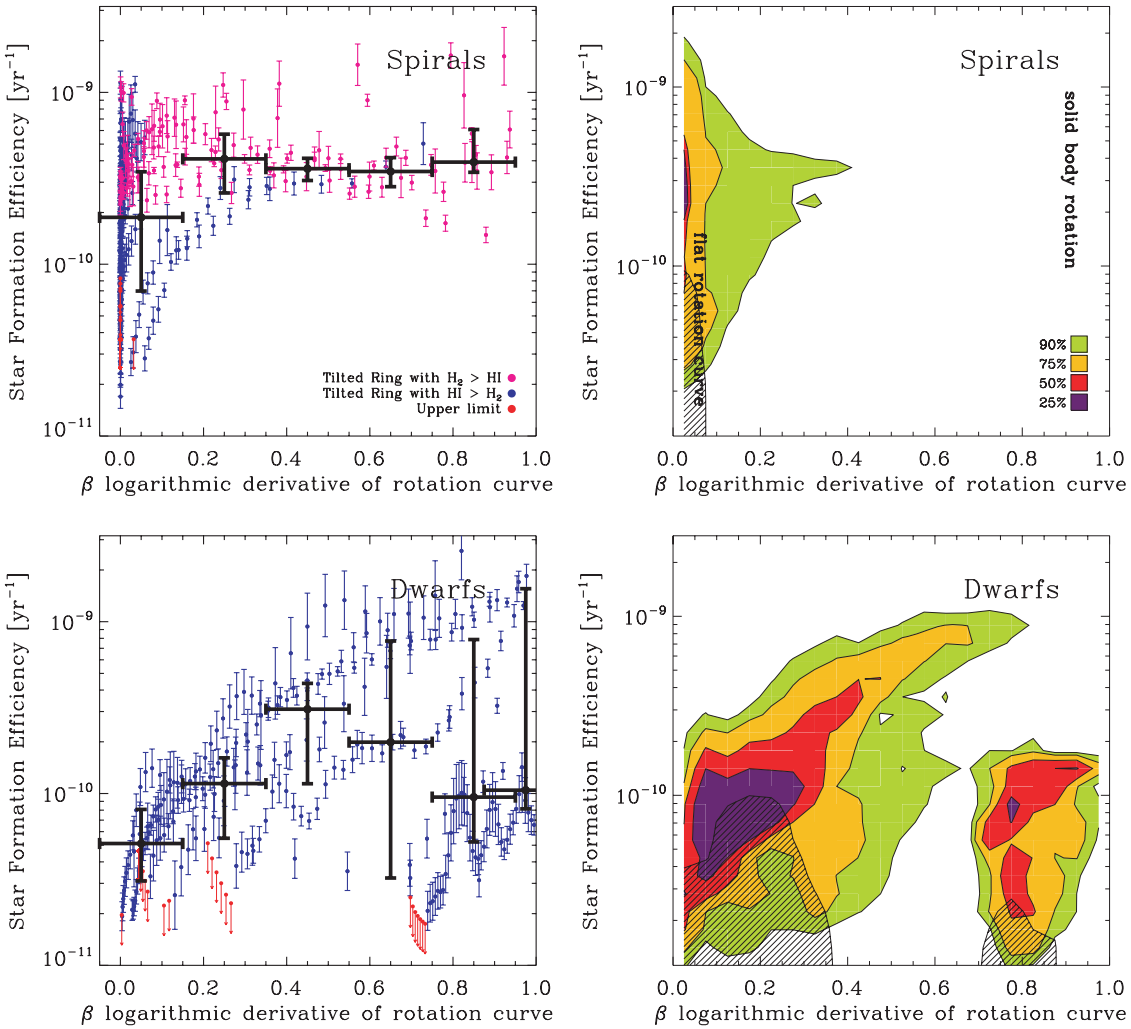

Figure 8. SFE as a function of β, the logarithmic derivative of the rotation curve in spiral (top row) and dwarf (bottom row) galaxies. $\beta = 1$ for solid body rotation and $\beta = 0$ for a flat rotation curve. If collisions between GMCs were important to triggering star formation, we would expect the SFE in the H_2 dominated (magenta) parts of spirals to be higher for low β (high shear), which is not apparent from the data.

stable, $Q_{\rm gas} \sim 4$ is typical inside $\sim 0.8 r_{25}$ and $Q_{\rm gas} > 10$ is common.

We find no clear evidence of a $Q_{\rm gas}$ threshold (at any value) that can unambiguously distinguish regions with high SFE from those with low SFE. In spirals, $Q_{\rm gas} \lesssim 2.5$ appears to be a sufficient, but by no means necessary, condition for high SFE; there are also areas where the ISM is mostly H_2, SFE is quite high, and $Q_{\rm gas} \gtrsim 10$. In dwarfs, $Q_{\rm gas}$ appears, if anything, anticorrelated with SFE, though this may partially result from incomplete estimates of $\Sigma_{\rm gas}$.

These conclusions appear to contradict the findings by Kennicutt (1989) and Martin & Kennicutt (2001), who found marginally stable gas ($Q_{\rm gas} \sim 1.5$) across the optical disk with a rise in $Q_{\rm gas}$ corresponding to dropping SFE at large radii. In fact, after correcting for different assumptions, our median $Q_{\rm gas}$ matches theirs quite well. Both Kennicutt (1989) and Martin & Kennicutt (2001) assumed $X_{\rm CO} = 2.8 \times 10^{20}$ cm^{-2} (K km s^{-1})$^{-1}$ and $\sigma_{\rm gas} = 6$ km s^{-1}, while we take $X_{\rm CO} = 2.0 \times 10^{20}$ cm^{-2} (K km s^{-1})$^{-1}$ and $\sigma_{\rm gas} = 11$ km s^{-1}, respectively. As a result, we estimate less H_2 and more kinetic support than they did for the same observations. If we match their assumptions, our median $Q_{\rm gas}$ in spirals and the outer parts of dwarfs agree quite well with their threshold value, though we find the central regions of dwarfs systematically above this value (as did Hunter et al. 1998a). We show this in Figures 9–11 by plotting the Martin & Kennicutt threshold converted to our assumptions ($Q_{\rm gas} \sim 3.9$) as a a dashed line.

The main observational difference between our result and Martin & Kennicutt (2001) is that $Q_{\rm gas}$ shows much more scatter in our analysis. As a result, a systematic transition from low to high $Q_{\rm gas}$ near the edge of the optical disk is not a universal feature of our data, though a subset of spiral galaxies does show increasing $Q_{\rm gas}$ at large radii (Figure 9).

This discrepancy in $Q_{\rm gas}$ derived from similar data highlights the importance of assumptions. The largest effect comes from $\sigma_{\rm gas}$, which we measure to be ≈ 11 km s^{-1} and roughly constant in H I-dominated outer disks (Appendix B). We assume $\sigma_{\rm gas}$ to be constant everywhere, an assumption that may break down on small scales and in the molecular ISM. In this case, we expect $\sigma_{\rm gas}$ to be locally lower than the average value, lowering $Q_{\rm gas}$ and making gas less stable. Black dots in the upper right panel of Figure 11 show the effect of changing $\sigma_{\rm gas}$ from 11 km s^{-1} (our value) to 6 km s^{-1} (the Martin & Kennicutt value) and then to 3 km s^{-1}, the value expected and observed for a cold H I component (e.g., Young et al. 2003; Schaye 2004; de Blok & Walter 2006). If most gas is cold, then $Q_{\rm gas}$ may easily be $\lesssim 1$

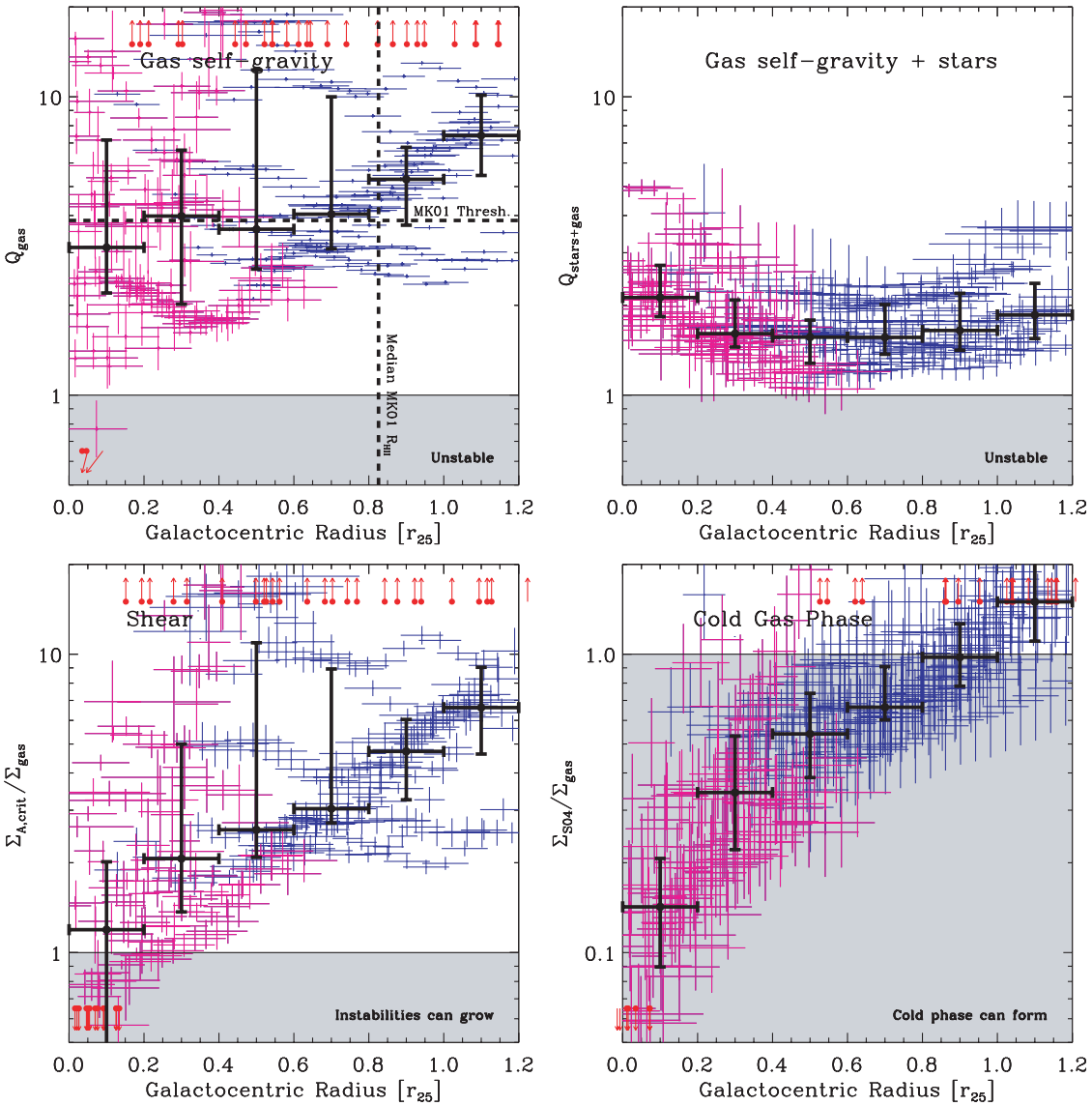

Figure 9. Radial behavior of thresholds in spiral galaxies: (top left) gravitational instability due to gas self-gravity, (top right) gravitational instability due to the combination of self-gravity and stellar gravity, (bottom left) competition between cloud formation and destruction by shear, and (bottom right) formation of a cold phase. Each point shows average $\Sigma_{\rm crit}/\Sigma_{\rm gas}$ over one 10″ tilted ring in one galaxy. In magenta rings, the ISM is mostly H_2 and in blue rings, the ISM is mostly H I. Gray regions show the condition required for star formation.

for this component (if only a small fraction of gas is cold, the situation is less clear).

4.3.2. Gravitational Instability Including Stars

Stars dominate the baryon mass budget over most of the areas we study and stellar gravity may be expected to affect the stability of the gas disk. In Section 2, we described a straightforward extension of $Q_{\rm gas}$ to the case of a disk containing gas and stars (Rafikov 2001). In Figure 12, we plot SFE as a function of this parameter, $Q_{\rm stars+gas}$, which we plot as a function of radius in the top right panels of Figures 9 and 10.

The gray region indicates where gas is unstable to axisymmetric collapse. Including stars does not render large areas of our sample unstable, but it does imply that most regions are only marginally stable, $Q_{\rm stars+gas} \sim 1.6$. This in turn suggests that it is not so daunting to induce collapse as one would infer from only $Q_{\rm gas}$.

In addition to lower values, $Q_{\rm stars+gas}$ exhibits a much narrower range of values than $Q_{\rm gas}$; mostly areas in both spiral and dwarf galaxies show $Q_{\rm stars+gas} = 1.3$–2.5. This may offer support to the idea of self-regulated star formation, but it also means that $Q_{\rm stars+gas}$ offers little leverage to predict the SFE. High SFE, mostly molecular regions show the same $Q_{\rm stars+gas}$ as low SFE regions from outer disks (indeed, the highest values we observe come from the central parts of spiral galaxies).

As with $Q_{\rm gas}$, our assumptions have a large impact on $Q_{\rm stars+gas}$. In addition to $\sigma_{\rm gas}$ and $X_{\rm CO}$(which affect the calculation via $Q_{\rm gas}$), the stellar velocity dispersion, σ_*, and the mass-to-light ratio, $\Upsilon_\star^K$, strongly affect our stability estimate. We assume that $\sigma_* \propto \Sigma_*^{0.5}$ in order to yield a constant stellar scale height. If we instead fixed σ_*, we would derive $Q_{\rm stars+gas}$, increasing steadily with radius. Radial variations in $\Upsilon_\star^K$ may create a similar effect.

Boissier et al. (2003) found results similar to our own when they incorporated stars in their stability analysis; they adopted a lower $\sigma_{\rm gas}$ than we did, but also lower $X_{\rm CO}$ and the effects roughly offset. Yang et al. (2007) recently derived $Q_{\rm stars+gas}$ across the LMC and found widespread instability that corresponded well

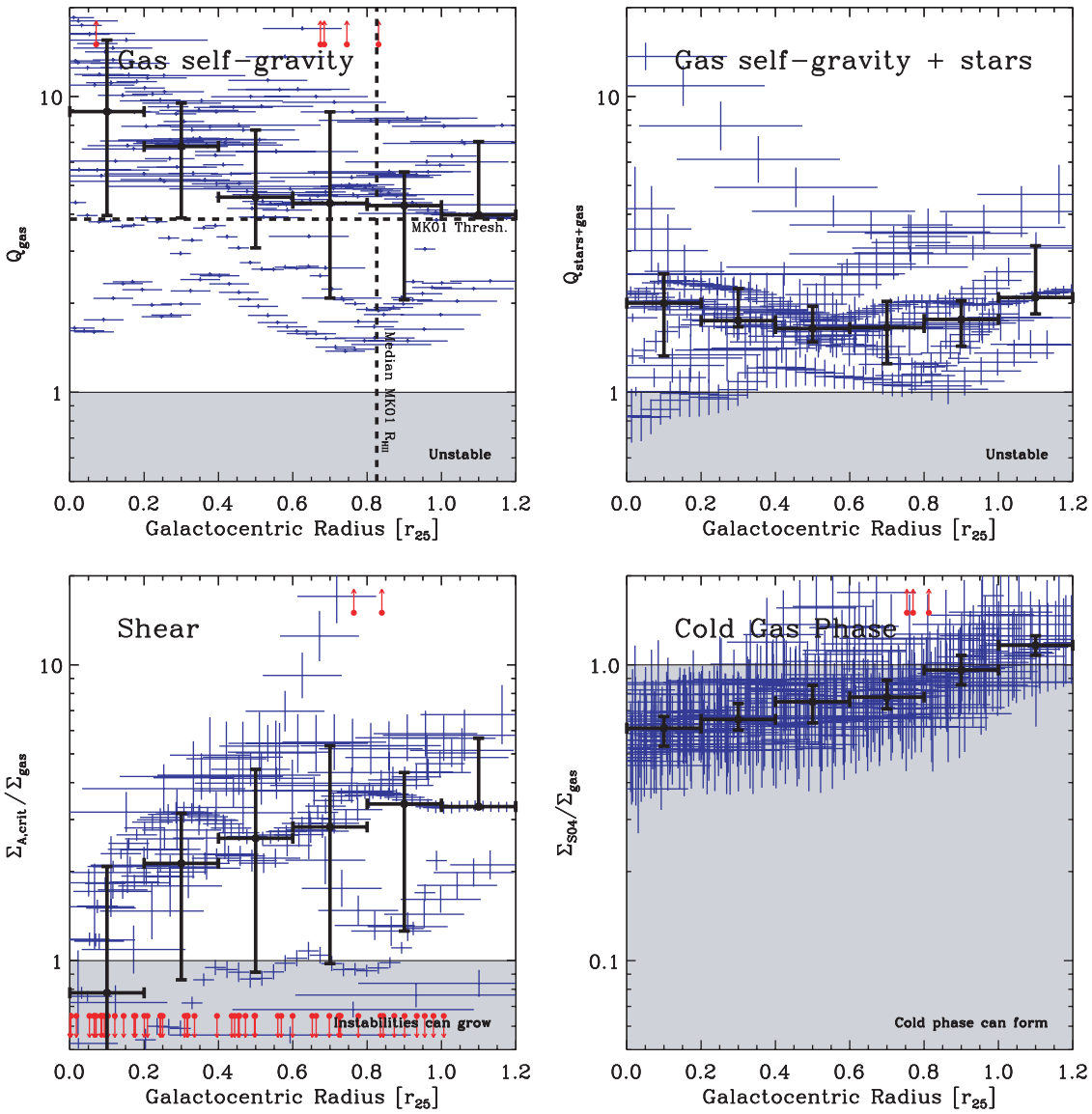

Figure 10. Radial behavior of thresholds in dwarf galaxies: (top left) gravitational instability due to gas self-gravity, (top right) gravitational instability due to the combination of self-gravity and stellar gravity, (bottom left) competition between cloud formation and destruction by shear, and (bottom right) formation of a cold phase. Each point shows average $\Sigma_{crit}/\Sigma_{gas}$ over one 10″ tilted ring in one galaxy. Gray regions show the condition required for star formation.

with the distribution of star formation. If we match their adopted σ_{gas} (5 km s^{-1}) and assumptions regarding σ_* (constant at 15 km s^{-1}), we also find widespread instability throughout our dwarf subsample, $Q_{stars+gas}$, decreasing with radius; we find a similar result for spirals if we fix σ_* at a typical outer disk value.

Our approach is motivated by observations of disk galaxies (see Appendix B), but direct observations of σ_* at large radii are still sorely needed.

4.3.3. Shear Threshold

If clouds form efficiently, for example, through the aid of magnetic fields to dissipate angular momentum, then Hunter et al. (1998a) suggest that the time available for a perturbation to grow in the presence of destructive shear may limit where star formation is widespread. Kim & Ostriker (2001) described a similar scenario where magneto-Jeans instabilities can grow in regions with weak shear or strong magnetic fields. In the bottom left panels of Figures 9 and 10, we plot this shear threshold as a function of radius, and in Figure 13, we compare it to the SFE.

The gray region shows the condition for instabilities to grow into GMCs, $\Sigma_{crit,A}/\Sigma_{gas} < 1$. This matches the condition $Q_{gas} < 1$ where $\beta = 0$, for example in outer disks of spirals. In the inner parts of spirals and in dwarf galaxies, however, $\Sigma_{crit,A}/\Sigma_{gas}$ is lower than Q_{gas}, that is, the conditions for star formation are more nearly supercritical (because shear is low in these regions). These areas harbor H_2 or widespread star formation, so supercritical values are expected.

This trend of more supercritical data at lower radii agrees with the steady increase of SFE with decreasing radius that we saw in Figure 1. However, the scatter in $\Sigma_{crit,A}/\Sigma_{gas} < 1$ is as large as that in Q_{gas} (as one would expect from their forms; see Table 1). As a result, a direct plot of SFE against $\Sigma_{crit,A}/\Sigma_{gas}$ does not yield clear threshold behavior or a strong correlation between $\Sigma_{crit,A}/\Sigma_{gas}$ and SFE. The strongest conclusion we can draw is that the inner parts of both spiral and dwarf galaxies are marginally stable for the shear threshold (an improvement over Q_{gas} and $Q_{stars+gas}$ in these regions).

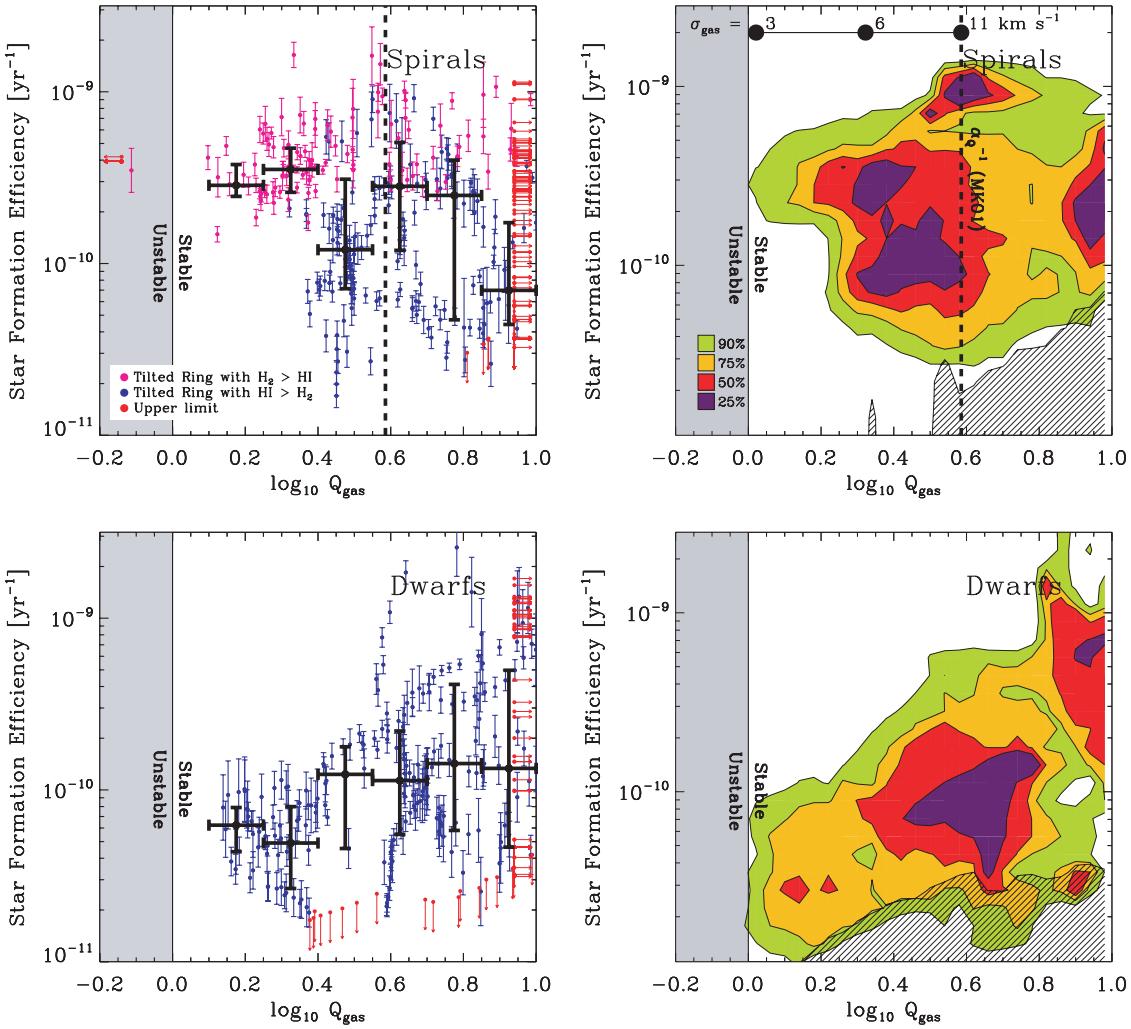

Figure 11. SFE as a function of $Q_{\rm gas}$, the Toomre Q parameter, which measures instability to axisymmetric collapse in a gas disk. Symbols and conventions follow Figure 1. The gray region shows where instability is expected. A dashed line in the top right panel shows the $Q_{\rm gas}$ threshold derived from Hα emission by Martin & Kennicutt (2001) converted to our assumptions. In the same panel, we show the effect on $Q_{\rm gas}$ of changing σ_g from our adopted 11 km s^{-1} to 6 km s^{-1} and then 3 km s^{-1}, expected for a cold phase.

4.3.4. Cold Phase Formation

Even where the ISM is stable against gravitational collapse on large scales, star formation may still proceed if a cold (narrow-line width) phase can form locally and thus induce gravitational instability in a fraction of the gas (recall the effect of lower $\sigma_{\rm gas}$ in Figure 11). Schaye (2004) argued that this is the usual path to star formation in the outer parts of galaxies and modeled the critical gas surface density for such a phase to form, $\Sigma_{\rm S04}$. The bottom right panels in Figures 9 and 10 show $\Sigma_{\rm S04}/\Sigma_{\rm gas}$ as a function of radius, and Figure 14 shows the SFE as a function of this ratio. The gray area in both figures shows where a cold phase can form.

We calculate $\Sigma_{\rm S04}$ from Equation (20), which depends on $I/(10^6$ cm^{-2} s$^{-1})$, the flux of ionizing photons. In outer disks, we assume $I = 10^6$ cm^{-2} s^{-1}, Schaye's fiducial value, and in inner disks, we take $I \propto \Sigma_{\rm SFR}$:

$$I \approx 10^6 \text{ cm}^{-2} \text{ s}^{-1} \left(\frac{\Sigma_{\rm SFR}}{5 \times 10^4 \ M_\odot \text{ yr}^{-1} \text{ kpc}^{-2}} \right). \quad (26)$$

The normalization is the average $\Sigma_{\rm SFR}$ between 0.8 and $1.0r_{25}$ in our spiral subsample.

Equation (20) also accounts for variations about Schaye's fiducial metallicity $Z = 0.1 \ Z_\odot$, typical for the outer disk of a spiral. We lack estimates of Z and so neglect this term but note the sense of the uncertainty. Inner galaxy disks will tend to have higher metallicities, which will lower $\Sigma_{\rm S04}$. We already find $\Sigma_{\rm gas} > \Sigma_{\rm S04}$ over most inner disks; therefore, missing Z seems unlikely to seriously bias our results.

Figures 9, 10, and 14 show that we expect a cold phase over most of the disk in both spiral and dwarf galaxies. In our spiral subsample, most data inside $r_{\rm gal} \sim 0.9r_{25}$ meet this criterion. Because most subcritical data come from large radii, we also find that most LOSs with $\Sigma_{\rm gas} < \Sigma_{\rm S04}$ exhibit low SFEs or upper limits.

Because most data are supercritical, the Schaye (2004) threshold is of limited utility for predicting the SFE *within* a galaxy disk. Schaye (2004) did not predict the ratio of H_2 to H I where cold gas formed; he was primarily concerned with the edges of galaxies. Figures 9 and 14 broadly confirm that his proposed threshold matches both the edge of the optical disk and the typical threshold found by Martin & Kennicutt (2001).

This relevance of this comparison to the SFE within the optical disk is that based on the Schaye (2004) model, we expect a widespread narrow-line phase throughout most of our galaxies (Wolfire et al. 2003 obtained a similar result for the Milky Way). This suggests that cold-phase formation followed by collapse

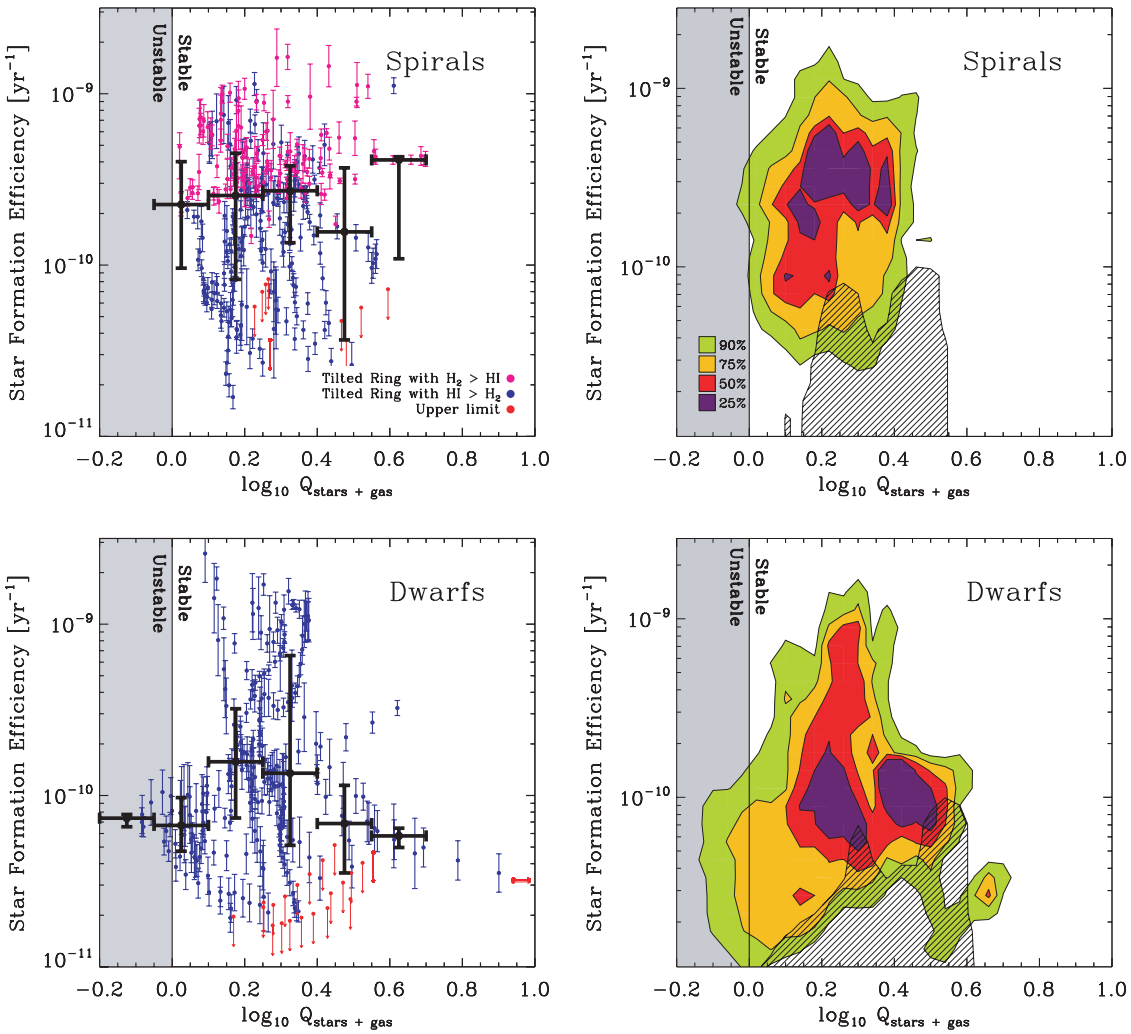

Figure 12. SFE as a function of $Q_{\rm stars+gas}$ (Rafikov 2001), which measures instability in a gas disk in the presence of a collisionless stellar disk. Symbols and conventions follow Figure 1. The gray region indicates where gas is unstable. Compared to $Q_{\rm gas}$, including stars renders the disk more nearly unstable and yields a much narrower range of values.

may be a common path to star formation and offers a way to form stars in our otherwise stable disks.

5. DISCUSSION

In Sections 4.1–4.3, we examined the SFE as a function of basic physical parameters, laws, and thresholds, respectively. Here we collect these results into general conclusions regarding the SFE in galaxies and identify key elements of a successful theory of star formation in galaxies.

5.1. Fixed SFE of H_2

Using a data set that overlaps the one presented here, Bigiel et al. (2008) found a linear relationship between $\Sigma_{\rm SFR}$ and $\Sigma_{\rm H_2}$. Here we extend that finding: *where the ISM is mostly H_2 in spiral galaxies, the SFE does not vary strongly with any of the quantities that we consider*, including radius, $\Sigma_{\rm gas}$, Σ_*, $P_{\rm h}$, $\tau_{\rm orb}$, and β. We plot SFE (H_2) as a function of each of these quantities in Figure 15. The median value for tilted rings from our spiral subsample is $\log_{10}{\rm SFE(H_2)} = -9.28 \pm 0.17$, that is,

$$\mathrm{SFE(H_2)} = (5.25 \pm 2.5) \times 10^{-10}\ \mathrm{yr}^{-1}. \quad (27)$$

Constant SFE (H_2) might be expected if (1) conditions within a GMC, rather than the larger-scale properties of the ISM, drive star formation (e.g., Krumholz & McKee 2005) and (2) GMC properties are relatively universal rather than, for example, a sensitive function of formation mechanism or environment. This appears to be the case in the inner Milky Way (excluding the Galactic center) and in M31 and M33, where GMC properties are largely a function of cloud mass alone (Solomon et al. 1987; Rosolowsky et al. 2003; Rosolowsky 2007; Blitz et al. 2007; Bolatto et al. 2008). The constancy of SFE (H_2) hints that a similar case holds in our spiral subsample.

Figure 6 illustrates why (relatively) universal GMC properties may be plausible in our sample. From Equation (9), the internal pressure of a starless GMC with $\Sigma_{\rm gas} \approx 170\ M_\odot\ \mathrm{pc}^{-2}$ (Solomon et al. 1987) is $P_{\rm h}/k_{\rm B} \sim 10^6\ \mathrm{K\ cm}^{-3}$. This is the highest value we plot in Figures 6 and 15, and only a small fraction of our data have higher $P_{\rm h}$ so that even where the ISM is mostly H_2, $P_{\rm h}$ is usually well below the typical internal pressure of a GMC. Thus, GMCs are not necessarily pressure-confined, which allows the possibility of bound, isolated GMCs out of pressure equilibrium with the rest of the ISM. In this case, the environmental factors that we consider may never be communicated to GMCs (though some mechanism may still be needed to damp out any imprint left by environment during GMC formation).

The range of $P_{\rm h}$ in our sample also underscores that one should not expect a constant SFE (H_2) to extend to starburst

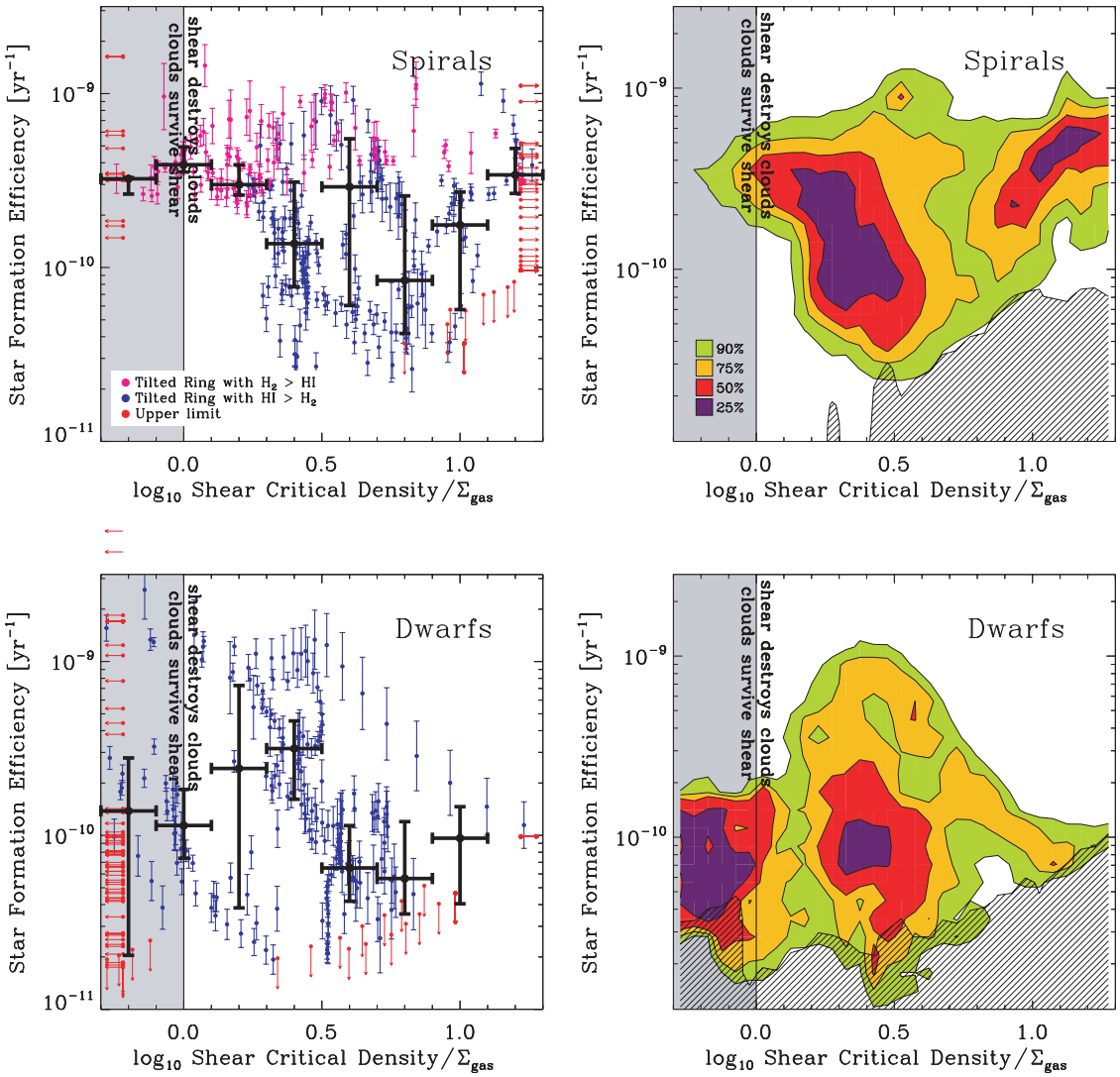

Figure 13. SFE as a function of $\Sigma_{crit,A}/\Sigma_{gas}$, the threshold for cloud growth in the presence of shear (Hunter et al. 1998a) for spiral (top row) and dwarf (bottom row) galaxies. Conventions and symbols follow Figure 1. The gray area shows where clouds should be able to survive distribution by shear.

conditions, where P_h and Σ_{gas} on kiloparsec scales exceed those found for individual Galactic GMCs, and SFE (H_2) is observed to strongly vary with local conditions (e.g., Kennicutt 1998a; Riechers et al. 2007).

Another important caveat is that the distribution of GMC masses is observed to vary with environment (Rosolowsky 2005), possibly as a result of varying formation mechanisms. This suggests that either the SFE of a GMC is only a weak function of its mass (and thus other properties) or that real variations in SFE (H_2) may exist in dwarf galaxies and the outskirts of spirals.

5.2. *Conditions at the H I-to-H_2 Transition in Spirals*

In spiral galaxies, the transition between an H I-dominated ISM and a mostly-H_2 ISM occurs at a characteristic value for most quantities. This can be seen from Figures 1, 3, 5–7, in which H I-dominated regions (blue points) typically occupy one region and H_2-dominated regions (magenta points) occupy another.

Table 5 gives our estimates of properties where $\Sigma_{HI} \approx \Sigma_{H_2}$ in spiral galaxies. For each galaxy, we measure the median of the property in question over all pixels where $\Sigma_{H_2} = 0.8$–$1.2\,\Sigma_{HI}$. Table 5 lists the median transition value in our spiral subsample, along with the (1σ) scatter and log scatter among galaxies. These values appear as dotted vertical lines in Figures 1, 3, 5–7. Note that methodology—the choice to use pixels or rings, to interpolate, use the mean or median, etc.—affects the values in Table 5 by ~20%.

From Table 5, we find that physical conditions at the H I-to-H_2 transition are fairly similar to those found in the solar neighborhood. The orbital time is $\approx 1.8 \times 10^8$ yr and the free-fall time in the gas disk is $\approx 4.2 \times 10^7$ yr. The midplane gas pressure is $P_h/k_B \approx 2.3 \times 10^4$ cm^{-3} K, corresponding to a particle density $n \sim 1$ cm^{-3}. The baryon mass budget in the disk is dominated by stars, $\Sigma_* \approx 81\,M_\odot$ pc^{-2} while $\Sigma_{gas} \approx 14\,M_\odot$ pc^{-2}. Accordingly, the gas is stable against large-scale gravitational collapse on its own ($Q_{gas} \approx 3.8$), but in the presence of stars, it is only marginally stable $Q_{stars+gas} \sim 1.6$.

Approximately 1% of gas is converted to stars per free-fall time at the transition, in agreement with expectations from Krumholz & McKee (2005). About 6% of gas is converted to stars per τ_{orb}. This agrees well with the disk-averaged value of ~7% derived by Kennicutt (1998a, adapted to our IMF and CO-to-H_2 conversion factor) and with the range of efficiencies found by Wong & Blitz (2002).

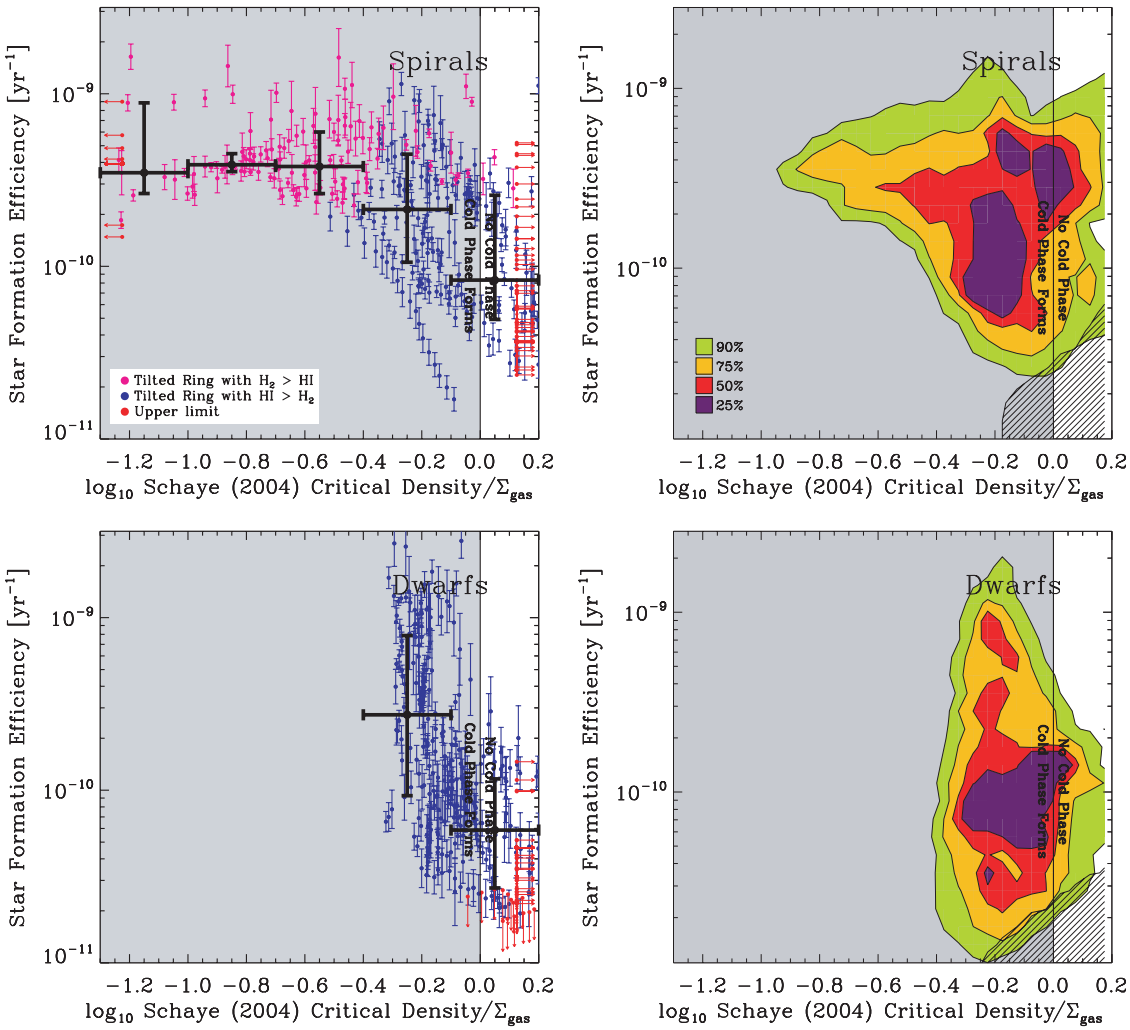

Figure 14. SFE as a function of $\Sigma_{S04}/\Sigma_{gas}$, the threshold for the formation of a cold phase (Schaye 2004), for spiral (top row) and dwarf galaxies (bottom row). Conventions and symbols follow Figure 1. The gray area indicates where Schaye (2004) estimates that a cold phase can form. Most areas where we observe star formation meet this criterion and the areas that do not tend to have low SFE.

Table 5
Conditions at the H I-to-H_2 Transition

Quantity	Median Value[a]	Scatter	Scatter in $\log_{10}$
r_{gal} (r_{25})	0.43	0.18	0.17
Σ_* ($M_\odot$ pc^{-2})	81	25	0.15
Σ_{gas} ($M_\odot$ pc^{-2})	14	6	0.18
P_h/k_B (cm^{-3} K)	2.3×10^4	1.5×10^4	0.26
τ_{ff} (yr)	4.2×10^7	1.2×10^7	0.14
τ_{orb} (yr)	1.8×10^8	0.4×10^8	0.09
Q_{gas}	3.8	2.6	0.31
$Q_{stars+gas}$	1.6	0.4	0.09

Note. [a] Median value in the spiral subsample.

5.3. H_2 in Dwarf Galaxies

Because of uncertainties in X_{CO}, we do not directly estimate the amount of H_2 in dwarf galaxies. However, indirect evidence suggests that a significant part of the ISM is H_2 in the central parts of these galaxies. Specifically, we observe very high SFE in the centers of dwarf galaxies—higher than SFE (H_2) in spirals—often under conditions associated with an H_2-dominated ISM in spirals (Section 5.2). It would be surprising if the SFE of H I in dwarfs indeed exceeds SFE (H_2) in spirals. We argue that an unaccounted-for reservoir of H_2 is a more likely explanation.

The SFE (H_2) that we observe in spiral galaxies offers an approximate way to estimate how much H_2 may be present. If we assume that SFE (H_2) is the same in dwarf and spiral galaxies, then we can calculate Σ_{H_2} from the observed Σ_{SFR} via

$$\Sigma_{H_2} \approx \frac{10^{-6}\ \Sigma_{SFR}}{5.25 \times 10^{-10}\ \mathrm{yr}^{-1}}. \quad (28)$$

This treatment suggests that in our typical dwarf galaxies, most of the ISM is H_2 within $\sim 0.25 r_{25}$. This may be directly seen from Equation (24), which translates our fit of SFE to radius to a relation between R_{mol} and radius assuming Equation (28). From Equation (24), Σ_{H_2}/Σ_{HI} in dwarf galaxies is 1–2 inside $\sim 0.25 r_{25}$, rising as high as ~ 3 at $r_{gal} = 0$.

5.4. Environment-Dependent GMC/H_2 Formation

Where the ISM is H I-dominated—in dwarf galaxies and outside the H I-to-H_2 transition in spirals—the SFE declines steadily with increasing radius. In this regime, the SFE is covariant with a number of environmental factors, including Σ_*, pressure, density, free-fall time, and orbital timescale. This observation, together with those in Sections 5.1 and 5.2, implies

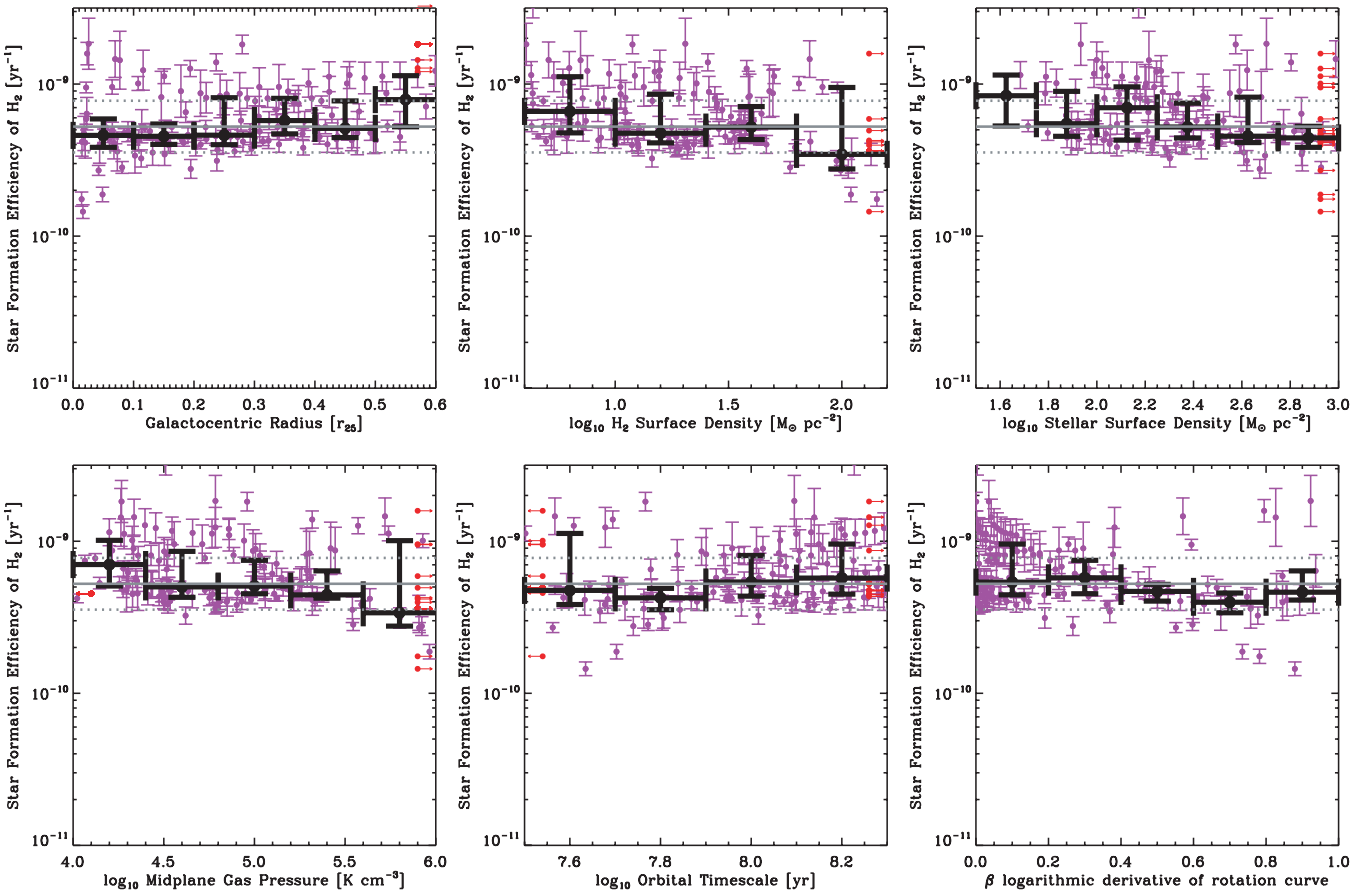

Figure 15. SFE (H_2) in individual tilted rings from spiral galaxies as a function of (top left) galactocentric radius, (top middle) H_2 surface density, (top right) stellar surface density, (bottom left) midplane pressure, (bottom middle) orbital timescale, and (bottom right) logarithmic derivative of the rotation curve. Gray lines show the median $\log_{10}$ SFE(H_2) $= -9.28 \pm 0.17$ for our data.

that while star formation *within* GMCs is largely decoupled from environment, the formation of H_2/GMCs from H I sensitively depends on local conditions.

In this case, we can break the SFE into two parts: star formation within GMCs and GMC formation, so that

$$\mathrm{SFE} = \mathrm{SFE}(H_2)\frac{\Sigma_{H_2}}{\Sigma_{\mathrm{gas}}} = \mathrm{SFE}(H_2)\frac{R_{\mathrm{mol}}}{R_{\mathrm{mol}}+1}, \qquad (29)$$

that is, the SFE is a product of a constant SFE (H_2) and $R_{\mathrm{mol}} = \Sigma_{H_2}/\Sigma_{H\,I}$, which is a function of local conditions.

We show this directly in Figure 16 and plot the same data, binned, in Figure 17. We plot $R_{\mathrm{mol}} = \Sigma_{H_2}/\Sigma_{H\,I}$ on the y-axis as a function of radius, Σ_*, P_h $\left(\propto \tau_{ff}^{-2}\right)$, and τ_{orb}. Red points show direct measurements of R_{mol} from CO and H I assembled following the methodology used by Blitz & Rosolowsky (2006) to compute R_{mol} as a function of P_h.

1. For each galaxy, we examine scatter plots to estimate a value of P_h above which our pixel-by-pixel measurements of Σ_{H_2} are approximately complete.
2. Where P_h is above this limit, we measure R_{mol} for each pixel.
3. We sort pixels into bins based on P_h and calculate the average and scatter in $\log_{10} R_{\mathrm{mol}}$ for the pixels in each bin.

A red point in Figure 16 corresponds to one P_h bin in one spiral galaxy; the x- and y-error bars indicate the width of the bin and the scatter in R_{mol} within the bin. We carry out analogous procedures to compute R_{mol} as a function of r_{gal}, Σ_*, and τ_{orb}.

Because of the limited sensitivity of the CO data, these direct measurements of R_{mol} seldom probe far below $R_{\mathrm{mol}} = 1$ and do not extend to dwarfs. Therefore, we also use Σ_{SFR} and $\Sigma_{H\,I}$ to estimate R_{mol} by assuming a fixed SFE (H_2). For each tilted ring in both subsamples, we convert Σ_{SFR} into Σ_{H_2} using Equation (28). We divide this by the observed $\Sigma_{H\,I}$ to estimate R_{mol} for that ring. We plot the results as green points for spirals and purple points for dwarf galaxies.[10] This approach—essentially plotting SFE (H I) in units of R_{mol}—allows us to estimate R_{mol} far below the sensitivity of our CO maps. While this extrapolation of SFE (H_2) may be aggressive, the quantity $\Sigma_{\mathrm{SFR}}/\Sigma_{H\,I}$ must be closely related to the ability of H I to assemble into star-forming clouds.

Figure 17 shows the data in Figure 16 binned by the quantity on the x-axis. Thin horizontal dashed lines show $R_{\mathrm{mol}} = 1$, that is, $\Sigma_{H\,I} = \Sigma_{H_2}$, and the value of the property on the x-axis that we estimate at the H I-to-H_2 transition (Section 5.2 and Table 5). Dashed and dotted lines, respectively, show fits and expectations that we discuss later in this section.

In spirals, the agreement between direct measurements of R_{mol} and estimates based on Σ_{SFR} and $\Sigma_{H\,I}$ is quite good. There is also general agreement between spirals and dwarf galaxies: the two subsamples sweep out similar, though slightly offset, trends in all four panels. The magnitude of the offsets between

[10] Because P_h depends on Σ_{gas}, we make a first-order correction to P_h in dwarf galaxies based on the estimated R_{mol}.

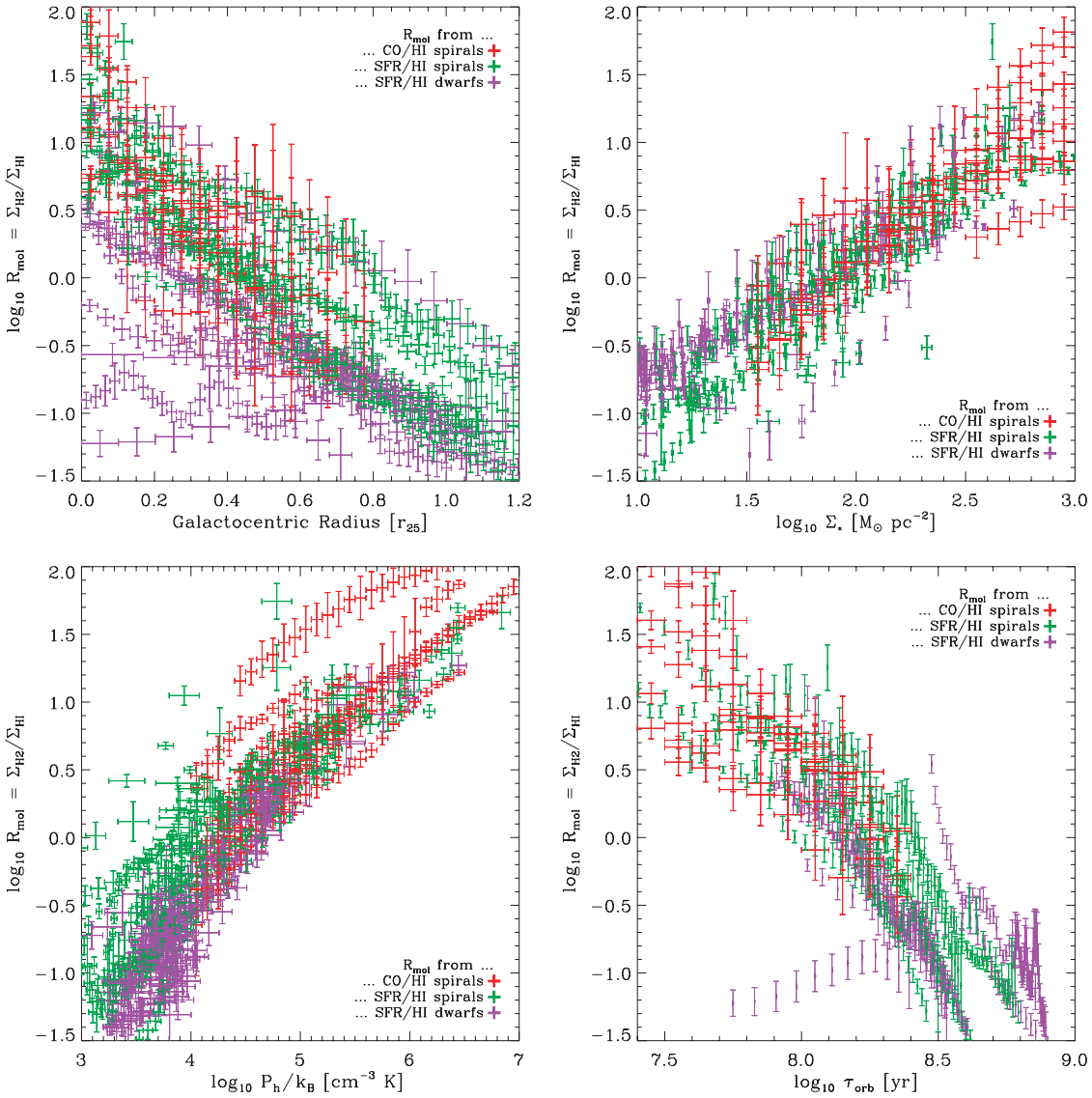

Figure 16. H_2-to-H I ratio, $R_{\rm mol} = \Sigma_{H_2}/\Sigma_{H\,I}$, as a function of (top left) radius, (top right) Σ_*, (bottom left) P_h ($\propto \tau_{ff}^{-2}$), and (bottom right) τ_{orb}. Red points are pixel-by-pixel measurements of $R_{\rm mol}$ in spirals, binned by the quantity on the x-axis. Green and purple points show tilted rings in spiral and dwarf galaxies with $R_{\rm mol}$ inferred from Σ_{SFR} and $\Sigma_{H\,I}$ assuming a fixed SFE (H_2). We show the same data, binned, in Figure 17.

dwarf and spiral galaxies that we see in Figure 17, typically 0.2–0.3 dex, offers indirect evidence that differences between the subsamples—metallicity, radiation fields, spiral structure (Section 3.1)—affect cloud formation or SFE (H_2) at the factor of the ~2–3 level.

Figures 16 and 17 explicitly show what we have already seen indirectly throughout Section 4. $R_{\rm mol}$ is a continuous function of environment spanning from the H_2-dominated ($R_{\rm mol} \sim 10$) to H I-dominated ($R_{\rm mol} \sim 0.1$) ISM, from inner to outer galaxy disks, and over a wide range of ISM pressures. This qualitatively confirms and extends similar findings by Wong & Blitz (2002) and Blitz & Rosolowsky (2006), which were mostly confined to the inner, molecule-dominated parts of spirals.

5.4.1. Cloud Formation Timescales

In Section 2, we discuss two basic ways that $R_{\rm mol}$ might be set by environment. First, the timescale to form GMCs may depend on local conditions. If H I and H_2 are in approximate equilibrium, with the entire neutral ISM actively cycling between these two phases, then

$$R_{\rm mol} = \frac{\Sigma_{H_2}}{\Sigma_{H\,I}} \approx \frac{\text{GMC lifetime}}{\tau(H\,I \rightarrow H_2)}. \quad (30)$$

For constant GMC lifetimes—perhaps a reasonable extension of fixed SFE (H_2)—$R_{\rm mol}$ is set by $\tau(H\,I \rightarrow H_2)$. In Sections 4.2.2 and 4.2.3, we saw that SFE anticorrelates with τ_{ff} and τ_{orb} where $\Sigma_{H\,I} > \Sigma_{H_2}$. If GMCs form over these timescales, then $R_{\rm mol} \propto \tau_{ff}^{-1}$ or $R_{\rm mol} \propto \tau_{orb}^{-1}$.

However, we found that the SFE decreased more steeply than one would expect if these timescales alone dictated $R_{\rm mol}$, so that increasing timescale for GMC formation cannot explain all of the decline in $R_{\rm mol}$. Figure 17 directly shows this: dotted lines in the bottom two panels illustrate $R_{\rm mol} \propto \tau_{ff}^{-1}$ and $R_{\rm mol} \propto \tau_{orb}^{-1}$, respectively. In both cases, the prediction is notably shallower than the data in both the H_2- and H I-dominated regimes.

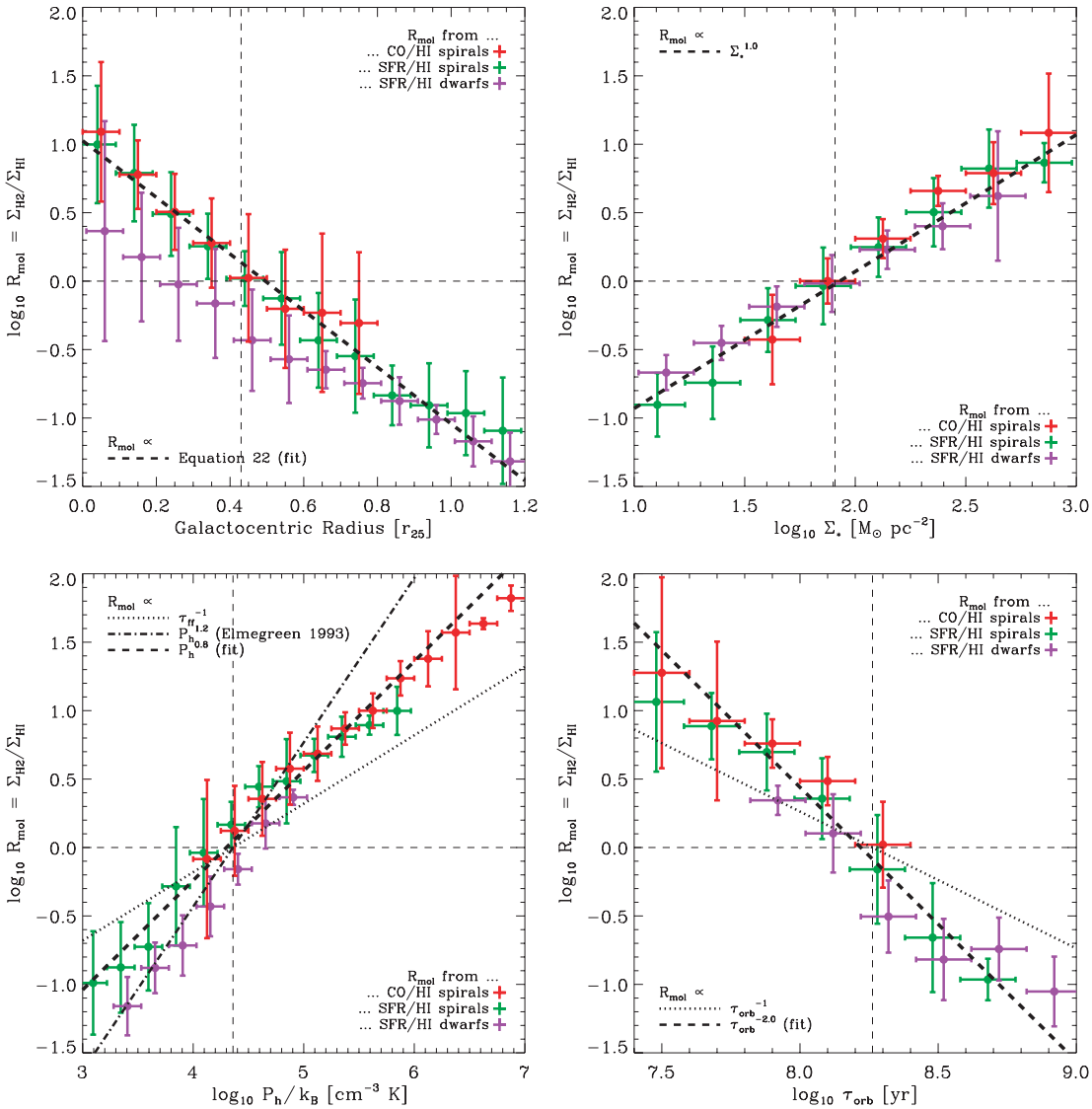

Figure 17. Data from Figure 16, binned by the quantity on the *x*-axis into three trends: $R_{\rm mol}$ measured pixel by pixel in spirals (red) and inferred from $\Sigma_{\rm SFR}$ and $\Sigma_{\rm H\,I}$ in (green) spiral and (purple) dwarf galaxies. Thin dashed lines show $R_{\rm mol} = 1$ (horizontal) and our estimate of each quantity at the H I-to-H_2 transition (vertical). Dotted lines show $R_{\rm mol} \propto \tau_{\rm ff}^{-1}$ (bottom left) and $R_{\rm mol} \propto \tau_{\rm orb}^{-1}$ (bottom right). Thick dashed lines show fits of $R_{\rm mol}$ to each quantity.

5.4.2. Disk Stability Thresholds

Of course, the entire ISM may not participate in cloud formation. Star formation thresholds are often invoked to explain the decrease in SFE between inner and outer galaxy disks. The amount of stable, warm H I may depend on environment, with a variable fraction of the disk actively cycling between H I and GMCs. This suggests a straightforward extension of Equation (30):

$$R_{\rm mol} = \frac{\Sigma_{\rm H_2}}{\Sigma_{\rm H\,I}} \approx \frac{\text{GMC lifetime}}{\tau(\text{H\,I} \rightarrow \text{H}_2)} \times f_{\rm GMC\,forming}, \qquad (31)$$

which again balances GMC formation and destruction but now includes the factor $f_{\rm GMC\,forming}$ to represent the fact that only a fraction of H I actively cycles between the molecular and atomic ISMs.

We considered three thresholds in which large-scale instabilities dictate $f_{\rm GMC\,forming}$—$Q_{\rm gas}$, $Q_{\rm stars+gas}$, and shear. One would naively expect these thresholds to correspond to $f_{\rm GMC\,forming} \sim 1$ for supercritical gas and $f_{\rm GMC\,forming} \ll 1$ for subcritical gas, yielding a step function in SFE or $R_{\rm mol}$. However, we do not observe such relationships between thresholds and SFE (Section 4.3); this agrees with Boissier et al. (2007) who also based their SFR profiles on extinction-corrected FUV maps and found no evidence for sharp star formation cutoffs.

If these instabilities regulate star formation but operate below our resolution, we still expect a correspondence between SFE and the average threshold value, which should indicate what fraction of the ISM is unstable. Despite this expectation, $Q_{\rm gas}$ shows little correspondence to the SFE and almost all of our sample is stable against axisymmetric collapse. Kim & Ostriker (2001, 2007) discussed $Q_{\rm gas}$ thresholds for the growth of nonaxisymmetric instabilities, but these are in the range $Q_{\rm gas} \sim$ 1–2, still lower than the typical values that we observe (Section 4.3.1). Even independent of the normalization, $Q_{\rm gas}$ shows little relation to the SFE, particularly in dwarf galaxies (also see Hunter et al. 1998a; Wong & Blitz 2002; Boissier et al. 2003).

Including the effects of stellar gravity reduces stability. Over most of our sample, $Q_{\rm stars+gas} \lesssim 2$ with a much narrower range than $Q_{\rm gas}$ (similar improvements were seen by Boissier et al. 2003; Yang et al. 2007). These values are roughly consistent with

the conditions for cloud formation found from simulations. Li et al. (2005) found that gas collapses where $Q_{\rm stars+gas} \lesssim 1.6$ and Kim & Ostriker (2001, 2007) found runaway instabilities where $Q_{\rm gas} \lesssim 1.4$ (though this is $Q_{\rm gas}$ and not $Q_{\rm stars+gas}$; for a region like the solar neighborhood, Kim & Ostriker 2007 argued that disk thickness, which tends to increase stability, approximately offsets the effect of stars on Q).

$Q_{\rm stars+gas}$ increases toward the central parts of spirals, so that although the ISM in these regions is usually dominated by H_2, they appear more stable than gas near the H I-to-H_2 transition. Hunter et al. (1998a) and Kim & Ostriker (2001) suggested that because of low shear, instabilities aided by magnetic fields may grow in these regions despite supercritical Q. Comparing to the shear threshold proposed by Hunter et al. (1998a), we find some support for this idea: at $\lesssim 0.2 r_{25}$, many dwarf and spiral galaxies appear unstable or marginally stable. As with $Q_{\rm gas}$, however, $\Sigma_{\rm crit,A}/\Sigma_{\rm gas}$ shows large scatter and no clear ability to predict the SFE.

Thus, we find no clear evidence that disk stability at large scales drives the observed variations in SFE and $R_{\rm mol}$. Improved handling of second-order effects (disk thickness, $\sigma_{\rm gas}$, $X_{\rm CO}$, σ_*, and $\Upsilon_\star^K$) may change this picture, but comparing our first-order analysis to expectations and simulations, disks appear marginally stable more or less throughout with little correlation between proposed thresholds and SFE.

5.4.3. Cold-Phase Formation

Timescales and thresholds computed at 400 (dwarfs) and 800 pc (spirals) scales do not offer a simple way to predict $R_{\rm mol}$. An alternative view is that physics on smaller scales regulates cloud formation. Comparison with models by Schaye (2004) suggests that a cold phase can form across the entire disk of most of our sample, which agrees with results from Wolfire et al. (2003) modeling our own Galaxy. High-density, narrow-linewidth clouds may easily be unstable or be rendered so by the passage of spiral arms or supernova shocks, even where the ISM as a whole is subcritical. Both Schaye (2004) and de Blok & Walter (2006) emphasized the effect of lower $\sigma_{\rm gas}$ on instability, and we have seen that a shift from the observed $\sigma_{\rm gas} = 11$ km s^{-1} to $\sigma_{\rm gas} = 3$ km s^{-1} would render most gas disks in our sample unstable or marginally stable (of course, a proper calculation requires estimating the density and fraction of the mass in this phase as well).

A narrow-line component is observed from high-velocity resolution H I observations of nearby irregular galaxies (Young et al. 2003; de Blok & Walter 2006), but an important caveat is the lack of direct evidence of such a component in THINGS. With ~2.5 or 5 km s^{-1} velocity resolution, one cannot distinguish a narrow component directly. Therefore, A. Usero et al. (2008, in preparation) followed up work by Braun (1997), who used the peak intensity along each LOS to estimate the maximum contribution from a cold phase and found pervasive networks of high brightness filaments. A. Usero et al. (2008, in preparation) found no clear evidence for a cold phase traced by networks of high brightness filaments, suggesting that a cold phase, if present, is mixed with the warm phase at the THINGS resolution of several times ~100 pc.

5.4.4. $R_{\rm mol}$ and Pressure

Despite this caveat, our results offer significant circumstantial support that ISM physics below our resolution dictates $R_{\rm mol}$: the lack of obvious threshold behavior, marginal stability of our disks, the ability of a cold phase to form, and the continuous variations in SFE and $R_{\rm mol}$ as a function of radius, Σ_*, and $P_{\rm h}$.

Table 6
Fits[a] of $R_{\rm mol} = \Sigma_{\rm H_2}/\Sigma_{\rm H\,I}$ to $(P_{\rm h}/P_0)^\alpha$

Source	$\log_{10} P_0/k_{\rm B}$ (cm^{-3} K)	α
Spiral subsample (CO/H I)	4.19	0.73
Spiral subsample (SFR/H I)[b]	4.30	0.79
Spiral subsample (combined)	4.23	0.80
Dwarf subsample (SFE/H I)[b]	4.51	1.05
Wong & Blitz (2002)	...	0.8
Blitz & Rosolowsky (2006)	4.54 ± 0.07	0.92 ± 0.07

Notes.
[a] Over the range $R_{\rm mol} = 0.1$–10.
[b] Estimating $\Sigma_{\rm H_2}$ from $\Sigma_{\rm SFR}$.

In particular, the relationship between $R_{\rm mol}$ and $P_{\rm h}$ has been studied before. Following theoretical work by Elmegreen (1993) and Elmegreen & Parravano (1994), Wong & Blitz (2002) and Blitz & Rosolowsky (2006) showed that $R_{\rm mol}$ and $P_{\rm h}$ correlate in nearby spiral galaxies (mostly at $R_{\rm mol} > 1$) and Robertson & Kravtsov (2008) recently produced a similar relationship from simulations that include cool gas and photodissociation of H_2; they emphasized the importance of the latter to reproduce the observed scaling.

The dash-dotted line in the bottom left panel of Figure 17 shows $R_{\rm mol} \propto P_{\rm h}^{1.2}$, predicted by Elmegreen (1993) from balancing H_2 formation and destruction in a model ISM. This is a reasonable description of dwarf galaxies, where we derive a best-fit power law with index ≈ 1.05. Spirals show a slightly shallower relation between $R_{\rm mol}$ and $P_{\rm h}$ with the best-fit power law index ≈ 0.80. The thick dashed line in the bottom left panel of Figure 17 shows our best fit to the spiral subsample (both CO/H I and SFR/H I) over the range $R_{\rm mol} = 0.1$–10. Table 6 lists this fit along with fits to dwarf galaxies and the results of Wong & Blitz (2002) and Blitz & Rosolowsky (2006).

The entry "spiral subsample (combined)" in Table 6 lists the best-fit power law like Equation (11) for our spiral subsample. This fit has an index $\alpha = 0.80$ and normalization $\log_{10} P_0/k_{\rm B} = 4.23$ (this is an ordinary least squares bisector fit over the range $0.1 < R_{\rm mol} < 10$ giving equal weight to each of the red and green points in Figure 16). Formally, the uncertainty in the fit is small because it includes a large number of data points. However, both $\log_{10} P_0/k_{\rm B}$ and α scatter by several tenths when fitted to individual galaxies. This agrees well with $\alpha = 0.8$ derived by Wong & Blitz (2002) and with $\alpha = 0.92 \pm 0.07$ obtained by Blitz & Rosolowsky (2006), given the uncertainties. Fitting the dwarf subsample in the same manner yields $\log_{10} P_0/k_{\rm B} = 4.51$, the pressure at the H I-to-H_2 transition. This is 0.2–0.3 dex higher than $\log_{10} P_0/k_{\rm B} = 4.23$ in spirals, suggesting that at the same pressure (density), GMC/H_2 formation in our dwarf subsample is a factor of ~2 less efficient than in spirals.

5.4.5. $R_{\rm mol}$ and Environment

The fits between $R_{\rm mol}$ and $P_{\rm h}$ in Table 6 are reasonable descriptions of the data, but do not represent a "smoking gun" regarding the underlying physics; radius, Σ_*, $P_{\rm h}$, and $\tau_{\rm orb}$ are all covariant and each could be used to predict $R_{\rm mol}$ with reasonable accuracy in spirals. Therefore, we close our discussion by noting a set of four scaling relations between $R_{\rm mol}$ and environment that

describe our spiral subsample:

$$R_{\rm mol} = 10.6 \exp(-r_{\rm gal}/0.21 r_{25}), \quad (32)$$

$$R_{\rm mol} = \Sigma_*/81\ M_\odot\ {\rm pc}^{-2}, \quad (33)$$

$$R_{\rm mol} = (P_{\rm h}/1.7 \times 10^4\ {\rm cm}^{-3}\ {\rm K}\ k_{\rm B})^{0.8}, \quad (34)$$

$$R_{\rm mol} = (\tau_{\rm orb}/1.8 \times 10^8\ {\rm yr})^{-2.0}. \quad (35)$$

These appear as thick dashed lines in Figure 17.

In particular, we stress the relationship between $R_{\rm mol}$ and Σ_* (also see Figure 3). This has several possible interpretations, the most simple of which is that stars form where they have formed in the past. However, there are physical reasons to think that the relationship may be causal. Considering a similar finding in dwarf irregular galaxies, Hunter et al. (1998a) suggested that stellar feedback may play a critical role in triggering cloud formation. Recently, the importance of the stellar potential well has been highlighted, either to triggering large-scale instabilities (Li et al. 2005, 2006; Yang et al. 2007) or in bringing gas to high densities in order for small-scale physics to operate more effectively (Elmegreen 1993; Elmegreen & Parravano 1994; Wong & Blitz 2002; Blitz & Rosolowsky 2004, 2006).

5.5. A Note on Systematics: X_{CO}, $\sigma_{\rm gas}$, σ_*, $\Upsilon_\star^K$

In this paper, we work "to first order," using the simplest well-motivated assumptions to convert observations to physical quantities. These assumptions are described in Section 3 and Appendices A–D. These are not always unique, and here we note differences with the literature and the effect that they may have on our analysis.

$X_{\rm CO}$. In spirals, we adopt a fixed $X_{\rm CO} = 2 \times 10^{20}$ cm^{-2} (K km s^{-1})$^{-1}$. Wong & Blitz (2002) and Blitz & Rosolowsky (2006) adopted the same value. Kennicutt (1989, 1998a), Martin & Kennicutt (2001), and Kennicutt et al. (2007) also used a fixed value, but a slightly higher one, $X_{\rm CO} = 2.8 \times 10^{20}$ cm^{-2} (K km s^{-1})$^{-1}$. Boissier et al. (2003) tested the effects of a metallicity-dependent $X_{\rm CO}$ that tends to yield lower $\Sigma_{\rm H_2}$ than our values in the inner parts of spirals, but higher in the outer parts.

Variations in the normalization of $X_{\rm CO}$ will affect the location of the H I-to-H$_2$ transition and the value of SFE (H$_2$), but not the observations of fixed SFE (H$_2$) or steadily-varying $R_{\rm mol}$. A strong dependence of $X_{\rm CO}$ on environment in spirals would affect many of our results, but leave the basic observation of environment-dependent SFE (H I) intact. Variations in the CO $J = 2 \rightarrow 1/1 \rightarrow 0$ line ratio (Appendix A) will manifest as changes in $X_{\rm CO}$.

$\sigma_{\rm gas}$. We adopt $\sigma_{\rm gas} = 11$ km s^{-1} based on the THINGS second moment maps (Appendix B). This is almost twice the commonly-used $\sigma_{\rm gas} = 6$ km s^{-1} (Kennicutt 1989, 1998a; Martin & Kennicutt 2001; Boissier et al. 2003) and also higher than $\sigma_{\rm gas} = 8$ km s^{-1}, adopted by Blitz & Rosolowsky (2006). In Section 4.3.1, we emphasize the importance of $\sigma_{\rm gas}$ to the stability analysis; observations with velocity and spatial resolution capable of distenangling different H I components and a multiphase analysis are needed to move forward on this topic.

σ_*. We assume an isothermal stellar disk with a fixed scale height, as did Boissier et al. (2003) and Blitz & Rosolowsky (2006). Wong & Blitz (2002) and Yang et al. (2007) assumed a fixed stellar velocity dispersion. This has a moderate effect on $P_{\rm h}$ and a strong effect on $Q_{\rm stars+gas}$ (Section 4.3.2).

$\Upsilon_\star^K$. We adopt $\Upsilon_\star^K = 0.5\ M_\odot/L_{\odot,K}$ (Appendix C), consistent with our adopted IMF and Bell et al. (2003), the same value used by Blitz & Rosolowsky (2004, 2006). $\Upsilon_\star^K$ directly affects Σ_*, $P_{\rm h}$, $\tau_{\rm ff}$, and $Q_{\rm stars+gas}$. It may vary by ∼30% both within and among galaxies (Bell & de Jong 2001), with larger variations in the bluest galaxies or from changes to the assumed IMF (Bell et al. 2003).

SFR tracer. We use FUV + 24 μm to estimate recent $\Sigma_{\rm SFR}$, discussed in detail in Appendix D. This is similar to Boissier et al. (2007) but in contrast to Kennicutt (1989, 1998a), Martin & Kennicutt (2001), Wong & Blitz (2002), and Boissier et al. (2003), who each used Hα emission with various extinction corrections. Boissier et al. (2007) considered differences between Hα and FUV profiles in detail, suggesting that stochasticity leads Hα to show signs of knees and turnoffs while FUV remains smooth. We work pixel by pixel and in radial profile (similar to Martin & Kennicutt 2001; Wong & Blitz 2002; Boissier et al. 2003; Blitz & Rosolowsky 2006) rather than attempting to isolate individual star-forming regions (e.g., Kennicutt et al. 2007). Both differences mean that we measure "recent" rather than "present" $\Sigma_{\rm SFR}$, which may account for some of the smoothness in the trends seen in Section 4.

6. STAR FORMATION RECIPES

As a final exercise, we compare our galaxies to simple star formation recipes based on the laws and thresholds discussed in Section 2 and normalized to the H I-to-H$_2$ transition in spirals (Section 5.2). We predict the SFE in this way.

1. We assume SFE (H$_2$) = 5.25×10^{-10} yr^{-1}.
2. We calculate $R_{\rm mol} = \Sigma_{\rm H_2}/\Sigma_{\rm H\,I}$, either
   (a) by setting $R_{\rm mol} = \tau_{\rm ff,0}/\tau_{\rm ff}$ or $\tau_{\rm orb,0}/\tau_{\rm orb}$, or
   (b) from our fits of $R_{\rm mol}$ to radius, Σ_*, $P_{\rm h}$, and $\tau_{\rm orb}$ in spiral galaxies (Equation 32).
3. We derive $\Sigma_{\rm SFR}$ from SFE (H$_2$), $R_{\rm mol}$, and $\Sigma_{\rm H\,I}$.
4. We calculate the predicted SFE, dividing $\Sigma_{\rm SFR}$ by $\Sigma_{\rm gas}$ in spirals and $\Sigma_{\rm H\,I}$ in dwarf galaxies.
5. We combine $R_{\rm mol} \propto \tau_{\rm ff}^{-1}$ or $\tau_{\rm orb}^{-1}$ with thresholds. In subcritical areas, we set SFE = 5×10^{-11} yr^{-1}, roughly the observed value at r_{25} in both subsamples.

Figure 18 illustrates the procedure for $R_{\rm mol} \propto \tau_{\rm ff}^{-1}$ and the $Q_{\rm stars+gas}$ threshold in the spiral galaxy NGC 3184.

We set $\tau_{\rm ff,0}$ and $\tau_{\rm orb,0}$ equal to the timescale at the H I-to-H$_2$ transition in spirals (Section 5.2; Table 5), that is, we predict $R_{\rm mol}$ by using the dotted lines in Figure 16. The predictions will, therefore, intersect our data where $R_{\rm mol} = \Sigma_{\rm H_2}/\Sigma_{\rm H\,I} \approx 1$ in spirals.

We adopt the same approach to normalize thresholds. For shear and $Q_{\rm stars+gas}$, we define the boundary between supercritical and subcritical data as 2.3 and 1.6, respectively, approximately the values at the H I-to-H$_2$ transition in spirals. For the Schaye (2004) cold phase threshold, we use a critical value of 1.

We implement thresholds pixel by pixel and present our results in radial average. Within a tilted ring, some LOSs can be supercritical and some can be subcritical, allowing the threshold to damp the average SFE in a ring without setting it to the minimum value.

The choice to normalize the recipes for both dwarf and spiral galaxies using values measured for spirals is meant to highlight differences between the subsamples.

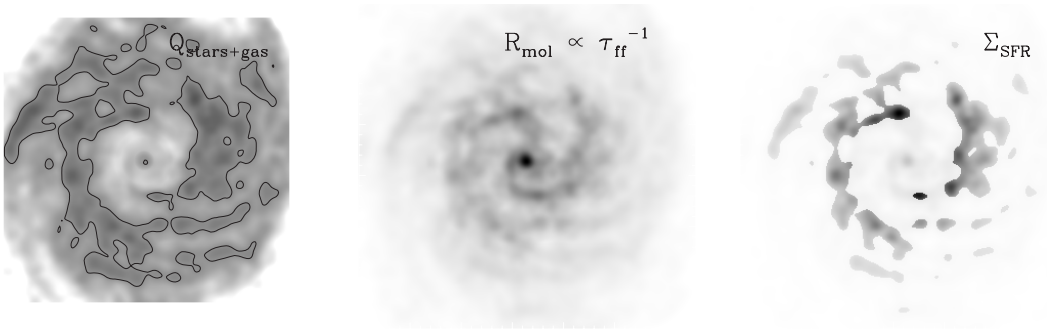

Figure 18. Prediction of $\Sigma_{\rm SFR}$, illustrated for NGC 3184. We calculate the threshold value (left; here $Q_{\rm stars+gas}$) and identify supercritical areas (solid contour). In parallel, we estimate $R_{\rm mol} = \Sigma_{\rm H_2}/\Sigma_{\rm H\,I}$ (middle), here from $R_{\rm mol} \propto \tau_{\rm ff}^{-1}$. We combine these with the assumption of a fixed SFE (H_2) and a (fixed) low SFE in subcritical areas to predict $\Sigma_{\rm SFR}$ (right).

6.1. Results

Figure 19 shows the results of these calculations. The observed SFE as a function of radius appears as a shaded gray region (based on Figure 1). Radial profiles of SFE compiled from predictions appear in color (these follow the same methodology used to make the bins in Figure 1). The top row shows results for spiral (left) and dwarf (right) galaxies setting $R_{\rm mol} \propto \tau_{\rm ff}^{-1}$ combined with several thresholds, the middle row shows results for $R_{\rm mol} \propto \tau_{\rm orb}^{-1}$ combined with the same stable of thresholds, and the bottom row shows the $R_{\rm mol}$ set by fits to radius, Σ_*, $P_{\rm h}$, and $\tau_{\rm orb}$.

Figure 19 illustrates much of what we discussed in Sections 4 and 5. First, adopting fixed SFE (H_2) ensures that we match the observed SFE with reasonable accuracy in the inner parts of spirals regardless of how we predict $R_{\rm mol}$. Using fits to predict $R_{\rm mol}$ (bottom row) offers a small refinement over the timescales in this regime, but as long as $R_{\rm mol} \gtrsim 1$, then SFE $\sim$ SFE (H_2). As a result, the available gas reservoir sets the SFR in this regime.

Setting $R_{\rm mol} \propto \tau_{\rm ff}^{-1}$ or $\tau_{\rm orb}^{-1}$ smoothly damps the SFE with increasing radius, but not by enough to match observations. Without a threshold, $\tau_{\rm ff}$ and $\tau_{\rm orb}$ overpredict the SFE at large radii in spiral galaxies and at $r \gtrsim 0.4 r_{25}$ in dwarf galaxies (black bins, top two rows).

Thresholds damp the SFE with mixed success (green, magenta, and blue bins in the top two panels). Each somewhat lowers the SFE in the outer parts of galaxies. In the process, however, both $Q_{\rm stars+gas}$ and shear predict suppressed star formation at low or intermediate radii in both dwarf and spiral galaxies, areas where we observe ongoing star formation (the vertical error bars show that the 50% range includes completely subcritical galaxies in both cases). In Section 4.3, we saw that the radial variation in these thresholds is often less than the scatter among galaxies at a given radius and that the step function behavior that we implement here is not clear in our data.

The Schaye (2004) threshold predicts that a cold phase can form almost everywhere in our sample and so only comes into play in the outer parts of spirals and in dwarf galaxies, where it damps the predicted SFE, but not by enough to match observations.

The bottom left panel shows that the fits mostly do a good job of reproducing the SFE in spirals, which is expected because they are fits to these data.

The same fits (to spirals) yield mixed results when applied to dwarf galaxies. The fits to Σ_* and $\tau_{\rm orb}$ show very large scatter and fits to radius, $P_{\rm h}$, and $\tau_{\rm orb}$ all overpredict SFE by varying amounts (similar discrepancies are evident comparing spirals and dwarfs in the top two panels). The scaling relations relating $R_{\rm mol}$ to environment in spirals apparently do not apply perfectly to dwarfs. Likely drivers for the discrepancy are the lower abundance of metals and dust and more intense radiation fields, which affect phase balance in the ISM and the rate of H_2 formation and destruction. Focusing on the pressure fit (green), we can phrase the observation this way: for the same pressure (density), cloud formation in our dwarf subsample is suppressed relative to that in spirals by a factor of $\sim$2.

7. SUMMARY

We combine THINGS, SINGS, the *GALEX* NGS, HERACLES, and BIMA SONG to study what sets the SFE in 12 nearby spirals and 11 nearby dwarf galaxies.

We use these data to estimate the SFR surface density, gas kinematics, and the mass surface densities of H I, H_2, and stars (Appendices A and C). To trace recent star formation, we use a linear combination of *GALEX* FUV and *Spitzer* 24 μm (Appendix D). We suggest that this combination represent a useful tool given the outstanding legacy data sets now available from these two observatories (e.g., SINGS and the *GALEX* NGS).

We focus on the SFE, $\Sigma_{\rm SFR}/\Sigma_{\rm gas}$, and the H_2-to-H I ratio, $R_{\rm mol}$. These quantities remove the basic scaling between gas and SFR, allowing us to focus on where gas forms stars quickly/efficiently (SFE) and the phase of the neutral ISM ($R_{\rm mol}$). We measure the SFE out to $\sim 1.2 r_{25}$, compare it to a series of variables posited to influence star formation, and test the ability of several predictions to reproduce the observed SFE.

7.1. Structure of Our Typical Spiral and Dwarf Galaxy

We deliberately avoid discussing individual galaxies in the main text (these data appear in Appendices E and F). Instead, we study "stacked" versions of a spiral and dwarf galaxy. We sketch their basic structure here.

The spiral galaxy has a roughly constant distribution of H I, $\Sigma_{\rm H\,I} \sim 6\ M_\odot\ {\rm pc}^{-2}$ out to $\sim r_{25}$. H I surface densities seldom exceed $\Sigma_{\rm H\,I} \sim 10\ M_\odot\ {\rm pc}^{-2}$; gas in excess of this surface density tends to be molecular. We observe no analogous saturation in $\Sigma_{\rm H_2}$, finding $\Sigma_{\rm H_2} \gtrsim 100\ M_\odot\ {\rm pc}^{-2}$ in the very central parts of many galaxies.

Molecular gas, star formation, and stellar surface density all decline with nearly equal exponential scale lengths, $\sim 0.2 r_{25}$, giving the appearance of a long-lived star-forming disk embedded in a sea of H I. The ISM is mostly H_2 within $\sim 0.5 r_{25}$ and where $\Sigma_* \gtrsim 80\ M_\odot$.

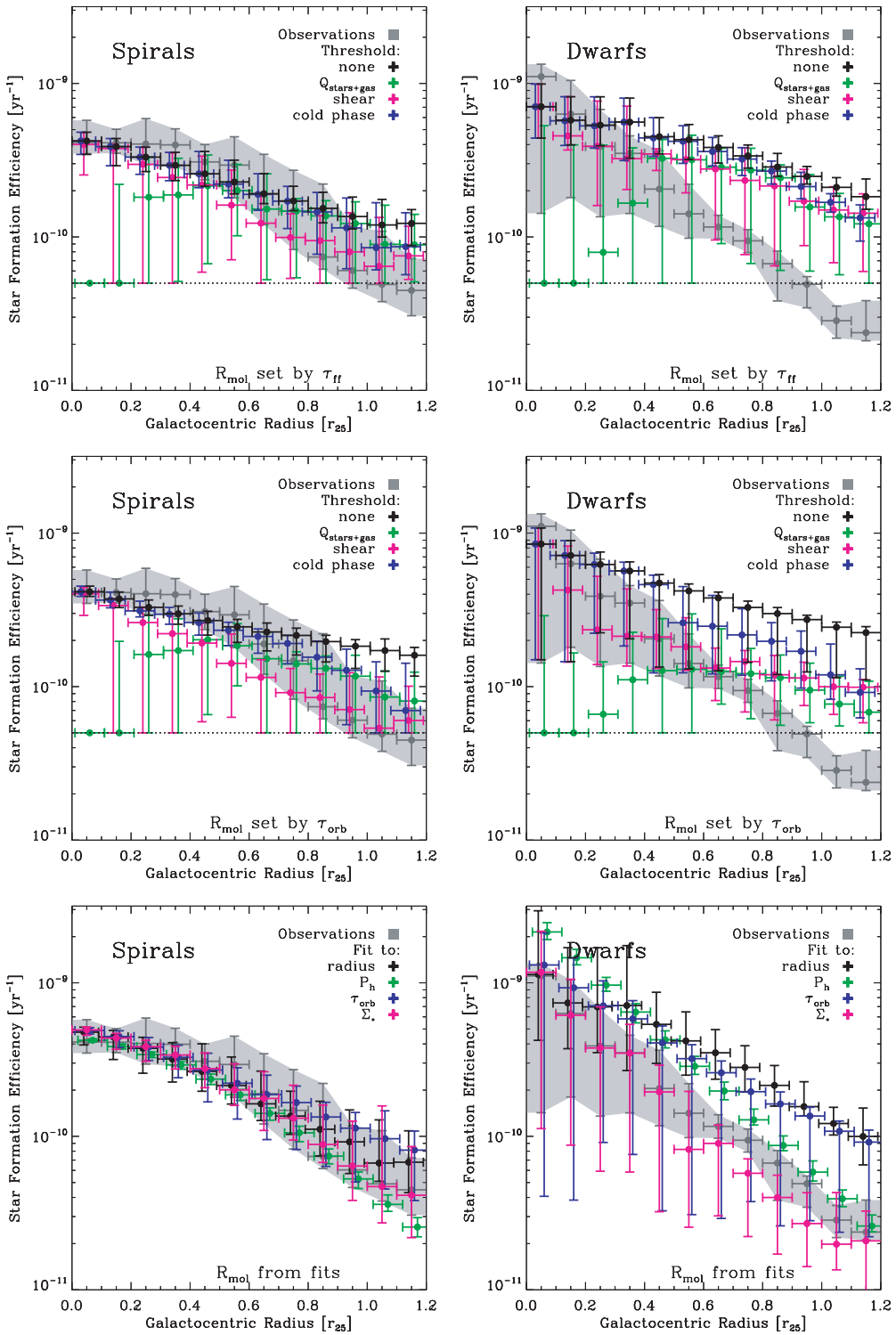

Figure 19. Comparison of predicted (color bins) to observed (gray region) SFE in spiral (left) and dwarf (right) galaxies. We adopt fixed SFE (H_2) and predict R_{mol} from τ_{ff}^{-1} (top row) and τ_{orb}^{-1} (middle panel) combined with thresholds. We also show four fits of R_{mol} to other quantities in spirals (bottom row). The dotted horizontal line in the top two rows shows the SFE that we adopt for subcritical data.

Over a wide range of conditions, the SFR per unit H_2, SFE (H_2), is equal to $(5.25 \pm 2.5) \times 10^{-10}$ yr^{-1} at scales of 800 pc. This is a "limiting efficiency" in the sense that we do not observe the average SFE in spirals to climb above this value. Where the ISM is mostly H I, the SFE is lower than this limiting value and declines radially with an exponential scale length of ~0.2–0.25r_{25}. In this regime, the SFR per unit stellar mass remains nearly fixed at a value about twice the cosmologically average rate (i.e., the stellar assembly time is approximately twice the Hubble time).

Dwarf galaxies also exhibit flat H I distributions, declining SFE with increasing radius, and a nearly constant stellar assembly time. Normalized to r_{25}, the scale length of the decline in the SFE is identical to that observed in spirals within the

uncertainties. The stellar assembly time is half of that found in spirals, corresponding to roughly a Hubble time. Dwarfs exhibit only the crudest relationship between Σ_{SFR} and $\Sigma_{H\,I}$ and, as a result, Σ_* is a much better predictor of the SFR than Σ_{gas} (in good agreement with Hunter et al. 1998a). The lack of a clear relationship between Σ_{SFR} and Σ_{gas} is at least partially due to an incomplete census of the ISM: conditions in the central parts of dwarf galaxies often match those where we find H_2 in spirals, and in these same regions, the SFE is (unexpectedly) higher than we observe anywhere in spirals (where H_2 is included).

7.2. Conclusions for Specific Laws and Thresholds

We compare the observed SFE to proposed star formation laws and thresholds described in Section 2. For star formation laws, we find the following.

1. The SFE dramatically varies over a small range of $\Sigma_{H\,I}$ and very little with changing Σ_{H_2}. Therefore, the *disk free-fall time for a fixed scale height disk* or any other weak dependence of SFE on Σ_{gas} is of little use to predict the SFE (Section 4.2.1).
2. *The disk free-fall time accounting for a changing scale height*, τ_{ff}, correlates with both SFE and R_{mol} (Section 4.2.2). Setting SFE proportional to τ_{ff} broadly captures the drop in SFE in spirals, but predicts variations in SFE (H_2) that we do not observe and is a poor match to dwarf galaxies. Taking τ_{ff} to be the relevant timescale for H I to form GMCs (i.e., $R_{mol} \propto \tau_{ff}^{-1}$) fails to capture the full drop in the SFE in either subsample.
3. The *orbital timescale*, τ_{orb}, also correlates with both SFE and R_{mol}, but in outer spirals and dwarf galaxies, both SFE and R_{mol} drop faster than τ_{orb} increases (Section 4.2.3). As with τ_{ff}, τ_{orb} alone cannot describe cloud or star formation in our sample.
4. In spirals, we observe no clear relationship between SFE (H_2) and the logarithmic derivative of the rotation curve, β (Section 4.2.3). In dwarf galaxies, SFE correlates with β. Both observations are in contrast to the anticorrelation between SFE and β expected if *cloud–cloud collisions* set the SFE (Tan 2000).
5. *Fixed GMC efficiency* appears to be a good description of our spiral subsample (Section 4.1; Bigiel et al. 2008). SFE (H_2) is constant as a function of a range of environmental parameters. This observation applies only to the disks of spiral galaxies, and not starbursts or low metallicity dwarf galaxies.
6. We observe a correspondence between hydrostatic *pressure and ISM phase* (Sections 4.2.2 and 5.4.4). In spirals, our results are consistent with previous work (Wong & Blitz 2002; Blitz & Rosolowsky 2006). In dwarf galaxies and the outer parts of spirals, inferring R_{mol} from SFE (H I) yields results roughly consistent with predictions by Elmegreen (1993).

For thresholds, we find the following.

1. Despite a suggestion of increased stability at large radii in spirals, there is no clear relation between Q_{gas}—which measures stability against axisymmetric collapse due to *self-gravity in the gas disk alone*—and SFE. Most regions are quite stable and Q_{gas} has large scatter, even appearing weakly anticorrelated with the SFE in dwarfs (Section 4.3.1).
2. When the effect of stars are included, most disks are only marginally stable: $Q_{stars+gas}$ (Rafikov 2001), which measures *gravitational instability in a disk of gas and stars*, lies mostly in the narrow range 1.3–2.5, increasing slightly toward the centers and edges of galaxies. We emphasize that adopted parameters—X_{CO}, σ_{gas}, $\Upsilon_\star^K$, and σ_*—strongly affect both Q_{gas} and $Q_{stars+gas}$ (Section 4.3.2).
3. The ability of instabilities to survive *competition with shear* (Hunter et al. 1998a) shows the same large scatter and high stability as Q_{gas} in the outer disks of spirals, but identifies most areas in dwarf galaxies and inner spirals as only marginally stable, an improvement over Q_{gas} (Section 4.3.3).
4. Most areas in both dwarf and spiral galaxies meet the condition needed *for a cold phase to form* (Section 4.3.4) (Schaye 2004). Regions that do not meet this criterion tend to come from outer disks and have low SFE. Because this criterion is met over such a large area, it is of little use on its own to predict variation in the SFE within galaxy disks.

Finally, we distinguish three different *critical surface densities*. First, in spirals $\Sigma_{gas} \sim 14\,M_\odot$ pc^{-2} at the H I-to-H_2 transition. We find no evidence that this is a real threshold for cloud formation: $R_{mol} = \Sigma_{H_2}/\Sigma_{H\,I}$ continuously varies across $R_{mol} = 1$ as a function of other quantities. However, it is useful to predict the SFE, which will be nearly constant above this Σ_{gas}. A related (but not identical) value, $\Sigma_{H\,I} \sim 10\ M_\odot$ pc^{-2}, is the surface density at which H I "saturates." Gas in excess of this surface density is in the molecular phase (Martin & Kennicutt 2001; Wong & Blitz 2002; Bigiel et al. 2008). This presumably drives the observation that most vigorous star formation takes place where $\Sigma_{H\,I} \gtrsim 10\ M_\odot$ pc^{-2} (e.g., Skillman 1987). Last, lower values, $\Sigma_{gas} \sim$ 3–4 $M_\odot$ pc^{-2} (e.g., Kennicutt 1989; Schaye 2004), may correspond to the edge of the star-forming disk. At our resolution, such values are relatively rare inside $1.2r_{25}$ and we draw no conclusion regarding whether this "outer disk threshold" corresponds to a real shift in the mode of star formation.

7.3. General Conclusions

Our general conclusions are as follows.

1. In the disks of spiral galaxies, the SFE of H_2 is roughly constant as a function of galactocentric radius, Σ_*, Σ_{gas}, P_h, τ_{orb}, Q_{gas}, and β (Section 5.1). This fixed SFE (H_2)= $(5.25 \pm 2.5) \times 10^{-10}$ yr^{-1} ($\tau_{Dep}(H_2) = 1.9 \times 10^9$ yr) sets the SFE of total gas across the H_2-dominated inner parts ($r_{gal} \lesssim 0.5r_{25}$) of spiral galaxies.
2. In spiral galaxies, the transition between a mostly-H I and a mostly-H_2 ISM is a well-defined function of local conditions (Section 5.2). It occurs at a characteristic radius ($0.43 \pm 0.18r_{25}$), Σ_* ($81 \pm 25\ M_\odot$ pc^{-2}), Σ_{gas} ($14 \pm 6\ M_\odot$ pc^{-2}), P_h ($2.3 \pm 1.5 \times 10^4 k_B$ cm^{-3} K), and τ_{orb} ($1.8 \pm 0.4 \times 10^8$ yr).
3. We find indirect evidence for abundant H_2 in the central parts of many dwarf galaxies, where SFE (H I) exceeds SFE (H_2) found in spirals. The simplest explanation is that H_2 accounts for a significant fraction of the ISM along these LOSs (Sections 4.1.1 and 5.3). The implied central $\Sigma_{H_2}/\Sigma_{H\,I}$ is ~2.5 with $\Sigma_{H_2} = \Sigma_{H\,I}$ at $\sim 0.25r_{25}$.
4. Where $\Sigma_{H\,I} > \Sigma_{H_2}$—in the outer parts of spirals and throughout dwarf galaxies (by assumption)—we observe the SFE to decline steadily with increasing radius, with

the scale length $\sim 0.2 r_{25}$–$0.25 r_{25}$ in both subsamples (Section 4.1). We also observe a decline in SFE with decreasing Σ_*, decreasing P_h, and increasing τ_{orb}, which are all covariant with radius.

5. Where $\Sigma_{H\,I} > \Sigma_{H_2}$, we find little relation between SFE and Σ_{gas} (Section 4.1.3) but a strong relationship between SFE and Σ_* (Section 4.1.2). The simplest explanation is that present-day star formation roughly follows past star formation. A more aggressive interpretation is that the stellar potential well or feedback is critical to bring gas to high densities.
6. The H_2-to-H I ratio, $R_{mol} = \Sigma_{H_2}/\Sigma_{H\,I}$, and by extension cloud formation, strongly depends on environment. R_{mol} correlates with radius, P_h, τ_{ff}, τ_{orb}, and Σ_* in spirals. We find corresponding correlations between these quantities and $\Sigma_{SFR}/\Sigma_{H\,I}$, a proxy for the efficiency of cloud formation in dwarfs and the outer parts of spirals. At our resolution, R_{mol} appears to be a continuous function of environment from the H I-dominated ($R_{mol} \sim 0.1$) to H_2-dominated ($R_{mol} \sim 10$) regime (Section 5.4).
7. The variation in R_{mol} is too strong to be reproduced only by varying τ_{orb} or τ_{ff} (Sections 4.2 and 5.4.1). Physics other than these timescales must also play an important role in cloud formation (points 8–11).
8. Thresholds for large-scale stability do not offer an obvious way to predict R_{mol}. We find no clear relationship (continuous or step function) between SFE and Q_{gas}, $Q_{stars+gas}$, or the shear threshold. The threshold values we find suggest disks that are stable or marginally stable throughout once the effects of stars are included (Sections 4.3 and 5.4.2).
9. We derive a power-law relationship between R_{mol} and hydrostatic pressure (Elmegreen 1989) that is roughly consistent with expectations by Elmegreen (1993), observations by Wong & Blitz (2002) and Blitz & Rosolowsky (2006), and simulations by Robertson & Kravtsov (2008). In its simplest form, this is a variation on the classical Schmidt law, that is, R_{mol} set by gas volume density (Sections 4.2 and 5.4.4).
10. Power-law fits of R_{mol} to P_h (τ_{ff}), radius, τ_{orb}, and Σ_* reproduce observed SFE reasonably in spiral galaxies but yield large scatter or higher-than-observed SFE in the outer parts of dwarf galaxies, offering indirect evidence that the differences between our two subsamples—metallicity (dust), radiation field, and strong spiral shocks—play a role in setting these relations (Sections 5.4.5 and 6).
11. Our data do not identify a unique driver for the SFE, but suggest that ISM physics below our resolution—balance between warm and cold H I phases, H_2 formation, and perhaps shocks and turbulent fluctuations driven by stellar feedback—govern the ability of the ISM to form GMCs out of marginally stable galaxy disks (Section 5.4.5).

We thank the anonymous referee for helpful suggestions that improved the paper. We thank D. Calzetti, R. Kennicutt, E. Rosolowsky, T. Wong, L. Blitz, and H. Roussel for suggestions and discussions during this project. We gratefully acknowledge the hard work of the SINGS, *GALEX* NGS, and BIMA SONG teams and thank them for making their data publicly available. E.B. gratefully acknowledges financial support through an EU Marie Curie International Reintegration Grant (contract no. MIRG-CT-6-2005-013556). F.B. acknowledges support from the Deutsche Forschungsgemeinschaft (DFG) Priority Program 1177. The work of W.J.G.dB is based upon research supported by the South African Research Chairs Initiative of the Department of Science and Technology and National Research Foundation. We have made use of the NASA/IPAC Extragalactic Database (NED), which is operated by the Jet Propulsion Laboratory, California Institute of Technology, under contract with the National Aeronautics and Space Administration; the HyperLeda catalog, located on the World Wide Web at http://www-obs.univ-lyon1.fr/hypercat/intro.html; NASA's Astrophysics Data System (ADS); and data products from the Two Micron All Sky Survey, which is a joint project of the University of Massachusetts and the Infrared Processing and Analysis Center/California Institute of Technology, funded by the National Aeronautics and Space Administration and the National Science Foundation.

APPENDICES

These appendices describe how we assemble the database of radial profiles and maps that are used in the main text. We discuss the data and methods that we use to derive gas surface densities (Appendix A), kinematics (Appendix B), stellar surface densities (Appendix C), and SFR surface densities (Appendix D). Finally, we present a table containing radial profiles of key quantities (Appendix E) and an atlas showing maps, profiles, and basic results for each galaxy (Appendix F).

APPENDIX A

MAPS OF H I AND H_2 SURFACE DENSITY

A.1. $\Sigma_{H\,I}$ *from THINGS 21 cm Maps*

THINGS (Walter et al. 2008) mapped 21 cm line emission from all of our sample galaxies using the VLA. We calculate atomic gas mass surface density, Σ_{HI}, from natural-weighted data that have a mean angular resolution of 11″ and a mean velocity resolution of 5 km s^{-1}. THINGS includes data from the most compact VLA configuration and, therefore, comfortably recovers extended structure (up to 15′) in our sources. At 30″ resolution, THINGS maps are sensitive to $\Sigma_{H\,I}$ as low as $\sim 0.5\,M_\odot$ pc^{-2}; here we adopt a working sensitivity of $\Sigma_{H\,I} = 1\ M_\odot$ pc^{-2}. In practice, the sensitivity and field of view (FOV) of the THINGS maps are sufficient to measure $\Sigma_{H\,I}$ to $\gtrsim r_{25}$ in almost every galaxy. For detailed description and presentation of THINGS, we refer the reader to Walter et al. (2008).

To convert from integrated intensity to $\Sigma_{H\,I}$, we use

$$\Sigma_{H\,I}(M_\odot\ \mathrm{pc}^{-2}) = 0.020 \cos i\, I_{21\,cm}(\mathrm{K\ km\ s}^{-1}), \qquad \text{(A1)}$$

which accounts for inclination and includes a factor of 1.36 to reflect the presence of helium.

A.2. Σ_{H_2} *from HERACLES (IRAM 30 m) and BIMA SONG CO Maps*

We estimate the surface density of molecular hydrogen, Σ_{H_2}, from CO emission, the most commonly-used tracer of H_2. Along with Bigiel et al. (2008), this study presents the first scientific results from HERACLES, a large project that used the HERA focal plane array (Schuster et al. 2004) on the IRAM 30 m telescope to map CO $J = 2 \rightarrow 1$ emission from the full optical

disk in 18 THINGS galaxies (Leroy et al. 2008). These data have an angular resolution of 11″ and a velocity resolution of 2.6 km s^{-1}. The typical noise in an individual channel map is 40–80 mK, yielding (masked) integrated intensity maps that are sensitive to $\Sigma_{H_2} \gtrsim 4\,M_\odot$ pc^{-2} at our working resolution and adopted conversion factor.

HERA maps are not available for NGC 3627 and NGC 5194. In these galaxies, we use CO $J = 1 \rightarrow 0$ maps from the BIMA SONG (Helfer et al. 2003) to estimate Σ_{H_2}. These data have an angular resolution of ∼7″ and include zero-spacing data from the Kitt Peak 12 m, ensuring sensitivity to extended structure.

We derive Σ_{H_2} from integrated CO intensity, I_{CO}, by adopting a constant CO-to-H_2 conversion factor, $X_{CO} = 2 \times 10^{20}$ cm^{-2} (K km s^{-1})$^{-1}$. Based on comparison to γ-ray and FIR observations, this value is appropriate in the Solar Neighborhood (Strong & Mattox 1996; Dame et al. 2001). For CO $J = 1 \rightarrow 0$ emission, the conversion to Σ_{H_2} is

$$\Sigma_{H_2}(M_\odot \text{ pc}^{-2}) = 4.4 \cos i\, I_{CO}(1 \rightarrow 0)(\text{K km s}^{-1}). \quad \text{(A2)}$$

In order to relate CO $J = 2 \rightarrow 1$ to CO $J = 1 \rightarrow 0$ intensity, we further assume a line ratio of $I_{CO}(2 \rightarrow 1) = 0.8 I_{CO}(1 \rightarrow 0)$. Based on direct comparison of HERACLES and previous surveys, this is a typical value in our sample (Leroy et al. 2008) and is intermediate in the range (∼0.6–1.0) observed for the Milky Way and other spiral galaxies (e.g., Braine et al. 1993; Sawada et al. 2001; Schuster et al. 2007). Thus, for the HERACLES maps, we derive Σ_{H_2} via

$$\Sigma_{H_2}(M_\odot \text{ pc}^{-2}) = 5.5 \cos i\, I_{CO}(2 \rightarrow 1)(\text{K km s}^{-1}). \quad \text{(A3)}$$

A.3. The CO-to-H_2 Conversion Factor

The CO-to-H_2 conversion factor is presumably a source of significant systematic uncertainty in Σ_{H_2}. X_{CO} almost certainly varies: it is likely to be lower than Galactic (yielding lower Σ_{H_2}) in overwhelmingly molecular, heavily-excited regions; it is likely to be higher (yielding higher Σ_{H_2}) in regions with low dust content and intense radiation fields, such as dwarf irregular galaxies. There is compelling evidence for both senses of variation, but it is our assessment that no reliable calibration of X_{CO} as a function of metallicity, radiation field, and Σ_{H_2} yet exists. A useful calibration must reflect all of these quantities, which all affect X_{CO} and are not universally covariant.

In light of this uncertainty, our approach is (1) to treat X_{CO} as unknown in low-mass, low-metallicity galaxies, where different approaches to measure Σ_{H_2} yield results that differ by an order of magnitude or more, and (2) to assume that variations in X_{CO} within spiral galaxies are relatively small. The second point might be expected based on theoretical modeling of GMCs (Wolfire et al. 1993) and the observed uniformity of GMC properties across a wide range of environments (Bolatto et al. 2008). We emphasize that even if present, the most extreme variations are likely to primarily contribute to the central resolution element, which is not the focus of this study, and the far outer disk, where Σ_{H_2} is not the dominant mass component.

Variations aside, estimates of "typical" values of X_{CO} in the Milky Way and other spiral galaxies span the range ∼1.5–4×10^{20} cm^{-2} (K km s^{-1})$^{-1}$ (e.g., Blitz et al. 2007; Draine et al. 2007, in addition to the references already given). The choice of mean X_{CO} within this range can have a large impact on, for example, assessing gravitational stability or conditions at the H_2-to-H I transition. We refer the reader to Boissier et al. (2003) for a quantitative exploration of how different assumptions regarding X_{CO} affect a stability analysis.

A.4. Masking the H I and CO Data Cubes

The H I and CO data cubes have large bandwidth, only a small part of which contains the spectral line. In order to produce integrated intensity maps with a good signal-to-noise ratio (S/N), we blank signal-free regions of the H I and CO cubes. Walter et al. (2008) described this process for THINGS. We apply an analogous procedure to the HERACLES and BIMA SONG data. We convolve the cubes to 30″ resolution, identify regions with significant emission, and then blank the original data cubes outside these regions. We integrate these blanked cubes to create intensity maps. For HERACLES, we require $I_{CO} > 2\sigma_{RMS}$ in three consecutive (2.6 km s^{-1}) channels at 30″ resolution. Note that our use of masking leads to small (∼10%) numerical differences with the HERACLES survey paper (which uses a different approach to create integrated intensity maps). For BIMA SONG, we require either $I_{CO} > 3\sigma_{rms}$ in a single (10 km s^{-1}) channel at 30″ resolution or $I_{CO} > 2\sigma_{rms}$ in consecutive velocity channels, similar to the original masking by Helfer et al. (2003). In both cases, we consider only CO emission within ∼100 km s^{-1} of the mean H I velocity.

APPENDIX B

KINEMATICS

B.1 Rotation Curves from THINGS

We approximate all galaxies to have rotation curves with the following functional form (Boissier et al. 2003):

$$v_{rot}(r) = v_{flat}\left[1 - \exp\left(\frac{-r}{l_{flat}}\right)\right], \quad \text{(B1)}$$

where v_{rot} is the circular rotation speed of the galaxy at a radius r and v_{flat} and l_{flat} are free parameters that represent the velocity at which the rotation curve is flat and the length scale over which it approaches this velocity, respectively. For a continuously rising rotation curve, common for low-mass galaxies, we expect large l_{flat}, while the almost flat rotation curves of massive spiral galaxies will have small l_{flat} and then remain nearly constant at v_{flat}.

In most cases, Equation (B1) captures the basic behavior of the rotation curve well. Small-scale variations are lost, but these may be due to streaming motions near spiral arms or warps in the gas disk as easily as real variations in the circular velocity. On the other hand, Equation (B1) offers the distinct advantage of having a smooth, analytic derivative. Our analysis uses the rotation curve to estimate the orbital timescale, shear, and coriolis force (see Section 2). The former is quite reasonably captured by Equation (B1) and the latter two critically depend on the derivative of the rotation curve $\beta = d \log v(r_{gal})/d \log r_{gal}$.

For each galaxy, we derive v_{flat} and l_{flat} from a nonlinear least-squares fit using Equation (B1) and profiles of v_{rot} measured from the THINGS data cubes. We calculate v_{rot} from the intensity-weighted first moment, v_r, via

$$v_{rot} = \frac{v_r - v_{sys}}{\sin i \cos\theta}. \quad \text{(B2)}$$

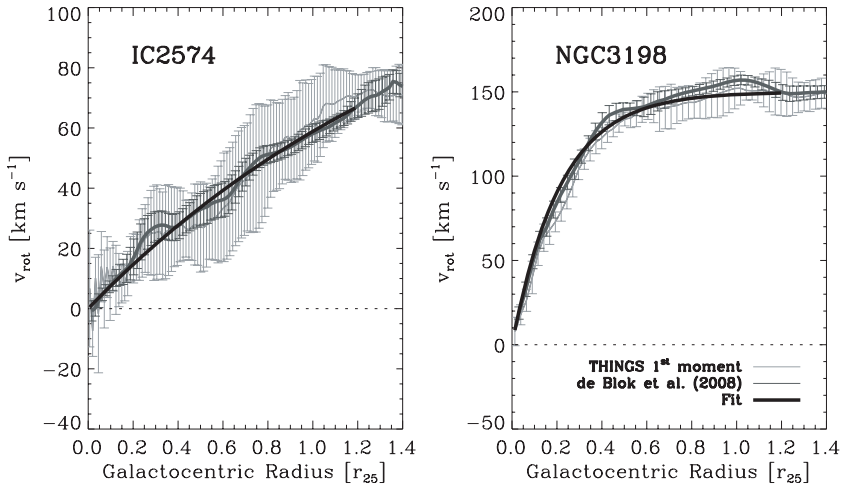

Figure 20. Illustration of our rotation curve treatment. Light gray profiles show median rotation velocity and scatter measured directly from the THINGS first moment maps; dark gray profiles and scatter show the higher quality (de Blok et al. 2008) rotation curves. The thick black lines show the fit that we use to approximate the rotation curve. This simple function (Equation B1) does a good job of capturing both the steadily rising rotation curves typical of dwarf galaxies (e.g., IC 2574, left panel) and the rapidly rising then flat curves seen in more massive spiral galaxies (e.g., NGC 3198, right panel).

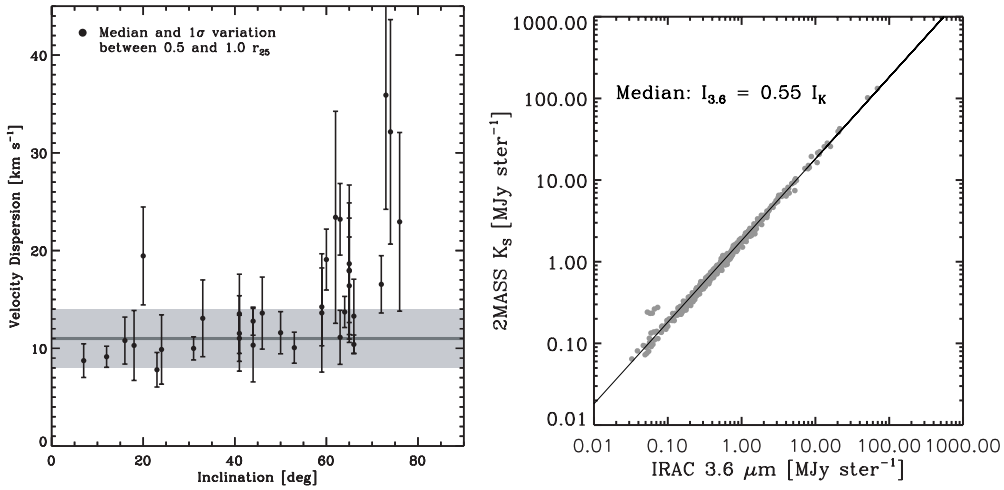

Figure 21. (Left) Motivation for our adopted gas velocity dispersion, σ_{gas}. We plot the median and 1σ range of σ_{gas} over the outer disk (0.5–1.0r_{25}) of each THINGS galaxy (including galaxies that are not part of this study) as a function of inclination. We see that variations within a galaxy are relatively small and that $\sigma_{gas} = 11 \pm 3$ km s^{-1} is a good description of galaxies with inclination $i \lesssim 60°$. Above this inclination, σ_{gas} is systematically higher with more scatter as a likely consequence of projection effects in these systems. We adopt a fixed σ_{gas} (gray line) throughout this work. (right) Median *K*-band intensity vs. median 3.6 μm intensity in 10″ wide tilted rings. A single scaling, $I_{3.6} = 0.55 I_K$ (shown by the solid line), relates the two well.

Here, v_{sys} is the systemic velocity, i is the inclination, and θ is the azimuthal angle relative to the receding major axis measured in the plane of the galaxy. We calculate maps of v_{rot} and then convert these into profiles of the median and 1σ scatter in v_{rot} within 60° of the major axis in a series of 5″ wide tilted rings. We fit Equation (B1) to the profile of median v_{rot} weighted by the scatter in that ring.

For many of our galaxies, high-quality rotation curves are available from the analysis of (see Table 2; de Blok et al. 2008). Wherever possible, we include these in our fit with very high weight, so that they drive the best-fit v_{flat} and l_{flat} for these galaxies. For the seven low-inclination galaxies in our sample that are not part of the study by (de Blok et al. 2008; see Column 4 of Table 2), we only fit the first moment data.

Figure 20 shows examples of this procedure for two galaxies: the dwarf irregular IC 2574, which has a steadily rising rotation curve, and the spiral galaxy NGC 3198, which has a quickly rising rotation curve that remains flat over most of the disk. We plot v_{rot} and associated scatter, the de Blok et al. (2008) rotation curve, and the best-fit version of Equation (B1). The best-fit values of v_{flat} and l_{flat} for all galaxies are given in Table 4; for the three galaxies that overlap the sample of Boissier et al. (2003), we match their fitted parameters well.

The dynamics of the irregular galaxies NGC 3077 and NGC 4449 are not well described by Equation (B1); the former is disturbed by an ongoing interaction with M81 and the latter has a counter-rotating core, perhaps due to a recent interaction (Hunter et al. 1998b). We neglect both galaxies in the kinematic analyses.

B.2 Gas Velocity Dispersion

Throughout this paper, we adopt a single gas velocity dispersion, $\sigma_{gas} = 11$ km s^{-1}. This is typical of the outer (H I-dominated) parts of THINGS galaxies and agrees well with values derived by Tamburro et al. (2008a), who conducted a thorough study of σ_{gas} in THINGS. The left panel in Figure 21 motivates this choice. We plot the median and 1σ range of σ_{gas} over the range 0.5r_{25}–1.0r_{25} for each galaxy in

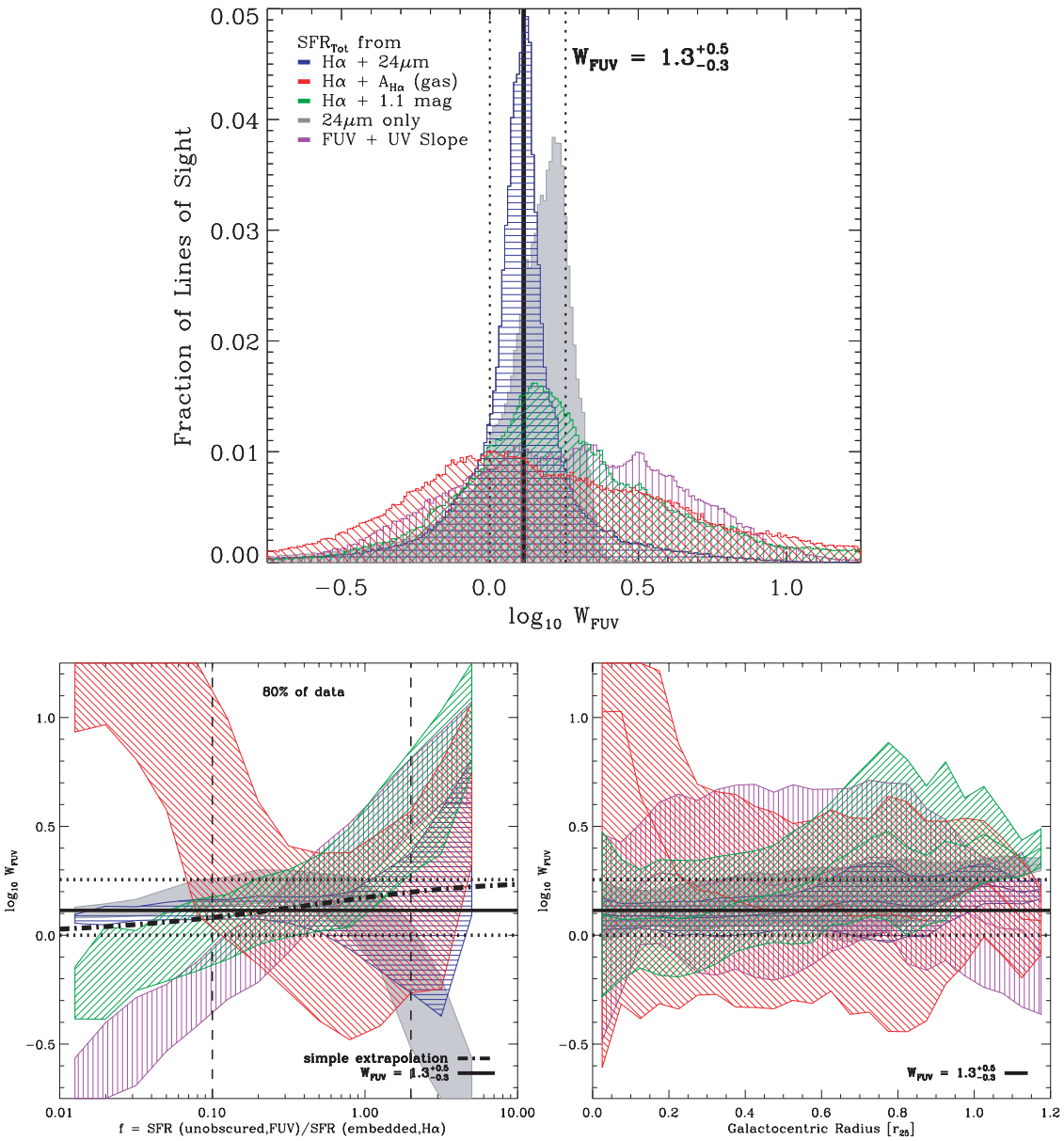

Figure 22. $W_{\rm FUV}$, the calibration of the 24 μm term to estimate the SFR from a linear combination of FUV and 24 μm emission. We measure $W_{\rm FUV}$ pixel by pixel by comparing FUV and 24 μm intensity to $\Sigma_{\rm SFR}$ estimated in five ways: (blue) combining Hα and 24 μm; (gray) using only 24 μm; (red) using Hα, estimating extinction from the gas; (green) using Hα, assuming a typical extinction; and (purple) using FUV emission, estimating $A_{\rm FUV}$ from the UV color. We plot the resulting $W_{\rm FUV}$ in three ways: (top) as normalized histograms; (bottom left) as a function of f, the ratio of FUV to 24 μm emission along a LOS (see Equation D9); and (bottom right) as a function of galactocentric radius normalized by r_{25}. The hatched regions in the bottom panels show the median trend $\pm 1\sigma$ for each case. In each panel, we indicate our adopted $W_{\rm FUV} = 1.3^{+0.5}_{-0.3}$. The dash-dotted curve in the bottom left panel shows the expectation for a typical extinction law and nebular-to-stellar extinction ratio, and the vertical dashed lines show the range of f that includes 80% of the data.

THINGS as a function of the inclination of the galaxy. We restrict ourselves to the outer disk because over this regime, H I usually dominates the ISM. This figure shows that a fixed $\sigma_{\rm gas} = 11 \pm 3$ km s^{-1} is a good description of the outer disk for galaxies with $i < 60°$; variations both within and among galaxies are comparatively small, typically 25%. However, highly inclined galaxies show large scatter and systematically high velocity dispersions, likely because the velocity dispersion is significantly affected by projection effects.

Variations in the gas velocity dispersion inside $0.5r_{25}$ could be expected to take two forms: $\sigma_{\rm gas}$ in the warm neutral medium may increase in regions of active star formation due to stellar feedback (e.g., Dib et al. 2006) and the fraction of gas in a narrow-line width (cold) H I phase may increase toward the centers of galaxies (e.g., Schaye 2004). The first effect is observed in THINGS: the second moment maps show a gradual increase in $\sigma_{\rm gas}$ from the outskirts to the centers of galaxies (Tamburro et al. 2008a). The second effect can, in principle, be observed using 21 cm line observations (de Blok & Walter 2006), but doing so is very challenging, requiring better spatial and velocity resolution and a higher S/N than is achieved in most THINGS targets. Further, we know that a large fraction of the ISM is H_2 in the central parts of our spiral galaxies, making it even more complicated to interpret measurements based only on H I. Because measuring the detailed behavior of $\sigma_{\rm gas}$ inside $\sim 0.5r_{25}$ is beyond the limit of our current data, and because $\sigma_{\rm gas}$

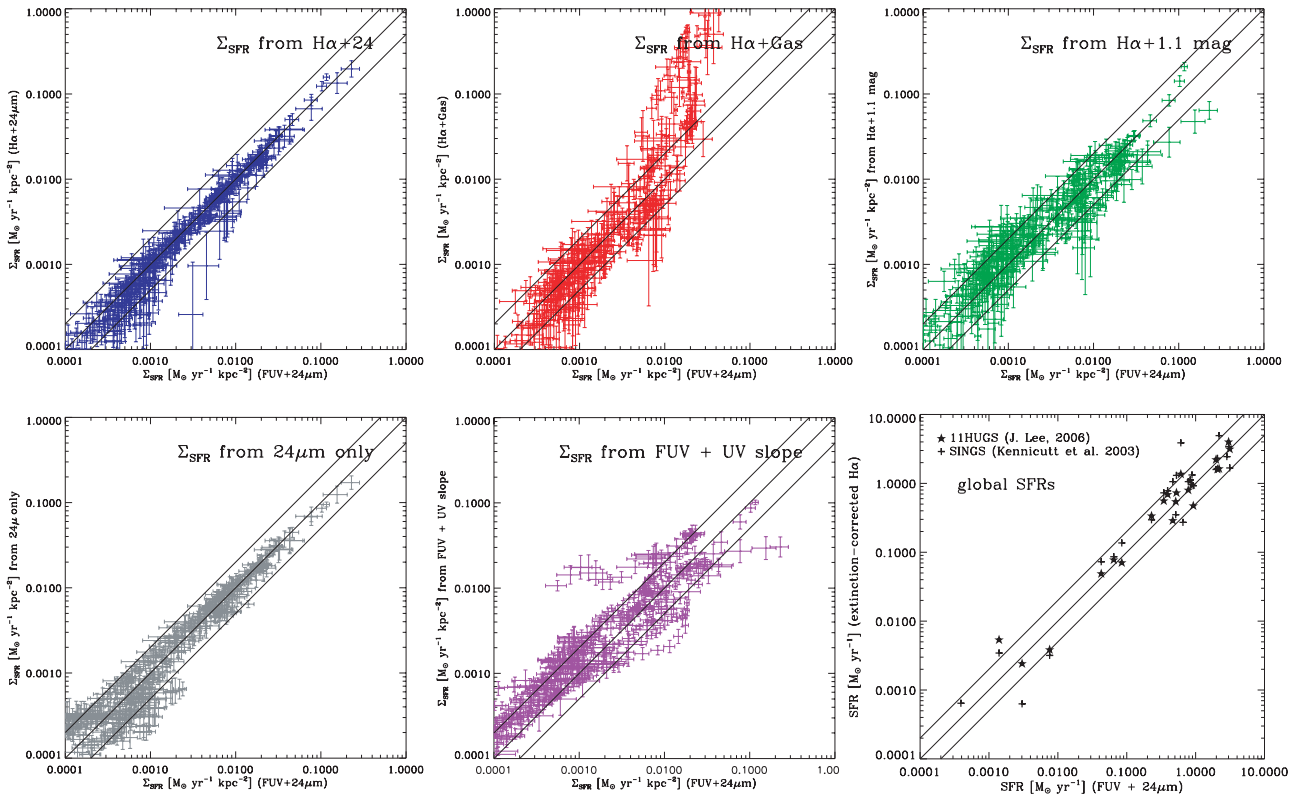

Figure 23. Five estimates of $\Sigma_{\rm SFR}$ (y-axis) as a function of $\Sigma_{\rm SFR}$ predicted by our combination of FUV and 24 μm. The color scheme is the same as Figure 22 and the methodology used to derive $\Sigma_{\rm SFR}$ for comparison is labeled in each plot. In the bottom right panel, each point shows the integrated SFR for a galaxy derived from Hα as a function of the SFR derived from FUV+24 μm emission. In all plots, solid lines show slopes of 0.5, 1, and 2.

varies only gradually in the outer parts of galaxies, we adopt a fixed $\sigma_{\rm gas}$ (an almost universal approach in this field, following Kennicutt 1989; Hunter et al. 1998a; Martin & Kennicutt 2001; Wong & Blitz 2002; Boissier et al. 2003).

B.3 Stellar Velocity Dispersion

Direct measurements of the stellar velocity dispersion, σ_*, across the disks of nearby galaxies are extremely scarce. In lieu of such observations for our sample, we make four assumptions to estimate σ_*. First, we assume that the exponential stellar scale height, h_*, of a galaxy does not vary with radius. This is generally observed for edge-on disk galaxies (van der Kruit & Searle 1981; de Grijs & Peletier 1997; Kregel et al. 2002). Second, we assume that h_* is related to the stellar scale length, l_*, by $l_*/h_* = 7.3 \pm 2.2$, the average flattening ratio measured by Kregel et al. (2002). Because we measure l_*, this yields an estimate of h_*. Third, we assume that our disks are isothermal in the z-direction, so that hydrostatic equilibrium yields $h_* = 1/2\left(\sigma_{*,z}^2/2\pi G\rho_*\right)^{0.5}$ (van der Kruit & Searle 1981), where ρ_* is the midplane stellar volume density and $\Sigma_* = 4\rho_* h_*$ (van der Kruit 1988). Eliminating ρ_* in terms of measured quantities, $\sigma_{*,z} = \sqrt{2\pi G\Sigma_* h_*}$ (van der Kruit 1988) and

$$\sigma_{*,z} = \sqrt{\frac{2\pi G l_*}{7.3}}\Sigma_*^{0.5}. \quad \text{(B3)}$$

Finally, we assume a fixed ratio $\sigma_{*,z} = 0.6\sigma_{*,r}$ to relate the radial and vertical velocity dispersions, which is reasonable for most late-type galaxies based on the limited available evidence (e.g., Shapiro et al. 2003).

These assumptions yield disk-averaged $Q_{\rm stars}$ (Equation 15) mostly in the range ~2–4, in reasonable agreement with estimates in the Milky Way (Jog & Solomon 1984; Rafikov 2001) and the expectation that stellar disks are marginally stable against collapse, $Q_{\rm stars} \sim 2$ (Kregel & van der Kruit 2005, and references therein). Our fixed flattening ratio yields results nearly identical to the fit used by Blitz & Rosolowsky (2006) to derive h_* from l_*. The scaling between σ_* and maximum rotation velocity observed by Bottema (1993) and Kregel & van der Kruit (2005) yields roughly similar scale heights but is more sensitive to adopted structural parameters (a problem for several face-on galaxies). The scatter among the various methods to estimate σ_* or h_* and observations remains ~50%, and this is clearly an area where more observations are needed (particularly measuring σ_* as a function of radius, though see Ciardullo et al. 2004; Merrett et al. 2006).

APPENDIX C

STELLAR SURFACE DENSITIES FROM THE INFRARED ARRAY CAMERA 3.6 μm BAND

SINGS (Kennicutt et al. 2003) imaged most of our sample using the IRAC instrument on *Spitzer* (Fazio et al. 2004). Emission from old stellar photospheres accounts for most of the emission seen in the Infrared Array Camera (IRAC) 3.6 μm band (e.g., Pahre et al. 2004), although we note that there may be some contribution from very hot dust and polycyclic aromatic hydrocarbon (PAH) features. Therefore, we use these data to estimate radial profiles of the stellar surface density, Σ_*. To convert from 3.6 μm intensity, $I_{3.6}$,

to Σ_*, we apply an empirical conversion from 3.6 μm to K-band intensity and then adopt a standard K-band mass-to-light ratio.

We work with median profiles of $I_{3.6}$, taken over a series of 10″ wide tilted rings using the structural parameters in Table 4. Real azimuthal variations, for example, due to bars or spiral arms, are lost. This is balanced by three major advantages from the median: (1) we avoid contamination by hot dust or PAH emission near star-forming regions, a potential issue with the 3.6 μm band; (2) we filter out foreground stars; and (3) we increase our sensitivity by averaging over the ring. The first advantage avoids a serious possible bias due to confusing Σ_* and $\Sigma_{\rm SFR}$. The latter two allow us to measure Σ_* out to large radii.

To calibrate the ratio of $I_{3.6}$ to K-band intensity, I_K, we compare $I_{3.6}$ profiles with I_K profiles from the Two Micron All Sky Survey (2MASS) Large Galaxy Atlas (LGA; Jarrett et al. 2003). The profiles from the LGA are not sensitive enough to reach $\gtrsim r_{25}$ in most cases, but they yield sufficient data to measure a typical I_K-to-$I_{3.6}$ ratio. The right panel in Figure 21 shows this measurement. We plot I_K as a function of $I_{3.6}$; each point gives median intensities in one 10″ wide tilted ring in one galaxy. The solid line shows a fixed ratio $I_{3.6} = 0.55 I_K$ (both in MJy ster^{-1}), which matches the data very well. This agrees with results from Oh et al. (2008), who investigated the K-to-3.6 μm ratio using stellar population modeling and found only very weak variations.

To convert I_K to Σ_* we apply a fixed K-band mass-to-light ratio, $\Upsilon_\star^K = 0.5\ M_\odot/L_{\odot,K}$. This is near the mean expected for our sample: applying the Bell et al. (2003) relation between $B-V$ color and mean $\Upsilon_\star^K$, we find $\Upsilon_\star^K = 0.48$–$0.60\ M_\odot/L_{\odot,K}$ (using global $B-V$ colors and assuming a Kroupa 2001 IMF to match our SFR). This small range in mean $\Upsilon_\star^K$ motivates our decision to adopt a constant value.

With our K-to-3.6 μm ratio, $\Upsilon_\star^K = 0.5\ M_\odot/L_{\odot,K}$, and the K-band magnitude of the Sun = 3.28 mag (Binney & Merrifield 1998), the conversion from 3.6 μm intensity to stellar surface density is

$$\Sigma_* = \Upsilon_\star^K \left\langle \frac{I_K}{I_{3.6}} \right\rangle \cos i\, I_{3.6} = 280 \cos i\, I_{3.6}, \qquad \text{(C1)}$$

with Σ_* in $M_\odot$ pc^{-2} assuming a Kroupa (2001) IMF and $I_{3.6}$ in MJy ster^{-1}.

The major uncertainty in Equation (C1) is the mass-to-light ratio, which depends on the star formation history, metallicity, and IMF. The mass-to-light ratio varies less in the NIR than in the optical but it does vary, showing ~ 0.1 dex scatter for redder galaxies and 0.2 dex for bluer galaxies (Bell & de Jong 2001; Bell et al. 2003). Because metallicity and star formation history exert different influences on galaxy colors and $\Upsilon_\star^K$, these variations are not readily inferred from colors (unlike in the optical; e.g., Bell et al. 2003).

In their analysis of the THINGS rotation curves, de Blok et al. (2008) also derived Σ_* from $I_{3.6}$. They used $J-K$ colors from the 2MASS LGA to estimate variations in $\Upsilon_\star^K$. Their Figure 21 compares our integrated masses to those that they derived using color-dependent $\Upsilon_\star^K$ for both a Kroupa (2001) and "diet Salpeter" (see Bell & de Jong 2001) IMF. Because they used the Bell & de Jong (2001) results, which have a fairly strong dependence on the NIR color, they found $\Upsilon_\star^K \sim 30\%$–$40\%$ higher than we did in massive (red) spiral galaxies, even for matched Kroupa (2001) IMFs.

APPENDIX D

SFR SURFACE DENSITY MAPS

We combine *GALEX* FUV and *Spitzer* 24 μm maps to estimate the SFR surface density, $\Sigma_{\rm SFR}$, along each LOS. FUV maps mostly show photospheric emission from O and B stars, and thus trace unobscured star formation over a timescale of $\tau_{\rm FUV} \sim 10$–100 Myr (e.g., Kennicutt 1998b; Calzetti et al. 2005; Salim et al. 2007). Emission at 24 μm originates from small dust grains mainly heated by UV photons from young stars. It has been shown to directly relate to ongoing star formation over a timescale of $\tau_{24} \sim 10$ Myr (e.g., Calzetti et al. 2005; Pérez-González et al. 2006; Calzetti et al. 2007). We adopt this tracer because (1) the resolution and sensitivity of the *GALEX* FUV and *Spitzer* 24 μm maps are both good (and well-matched), (2) these data are available for our whole sample, and (3) the combination is directly sensitive to both exposed and embedded star formation.

In this section, we take a practical approach, calibrating our tracer by comparing it to other estimates of $\Sigma_{\rm SFR}$. For a more thorough discussion of the relationship between extinction, UV, and IR emission, we refer the reader to, for example, Calzetti et al. (1995), Buat et al. (2002), Bell (2003), Cortese et al. (2006), and Boissier et al. (2007). Our tracer mainly builds on two recent results: (1) for entire galaxies, Salim et al. (2007) showed that FUV emission can be used to accurately measure SFRs (with typical $\tau_{\rm FUV} \sim 20$ Myr) if extinction is properly accounted for and (2) Calzetti et al. (2007) and Kennicutt et al. (2007) demonstrated that 24 μm data could be used to accurately correct Hα for extinction. We combine these results using a method similar to that of Calzetti et al. (2007): via comparisons to other estimates of extinction-corrected $\Sigma_{\rm SFR}$, we derive a linear combination of FUV and 24 μm intensity that we use to estimate $\Sigma_{\rm SFR}$:

$$\Sigma_{\rm SFR} = \left(8.1 \times 10^{-2} I_{\rm FUV} + 3.2^{+1.2}_{-0.7} \times 10^{-3} I_{24}\right) \cos i. \qquad \text{(D1)}$$

Here, $\Sigma_{\rm SFR}$ has units of $M_\odot$ kpc^{-2} yr^{-1} and FUV and 24 μm intensity are each in MJy ster^{-1}. The first term measures unobscured SFR using the FUV-to-SFR calibration found by Salim et al. (2007); the second term measures embedded SFR from 24 μm and is 30% higher than the matching term in the Hα+24 μm calibration of Calzetti et al. (2007). The additional weight reflects the fact that FUV is more heavily absorbed than Hα.

Following Calzetti et al. (2007), Equation (D1) assumes the default IMF of STARBURST99 (Leitherer et al. 1999), the broken power law given by Kroupa (2001) with a maximum mass of 120 $M_\odot$. This yields $\Sigma_{\rm SFR}$ a factor of 1.59 lower than a 0.1–100 $M_\odot$ Salpeter (1955) IMF (e.g., Kennicutt 1989, 1998a). Our FUV term is Equation (10) from Salim et al. (2007) divided by this value (1.59); the calibration is the same found for the Chabrier (2003) IMF over the range 0.1–100 $M_\odot$ (their Equations 7 and 8).

D.1 Data

D.1.1. GALEX NGS FUV Maps

We use FUV maps obtained by the *GALEX* satellite (Martin et al. 2005) as part of the *GALEX* Nearby Galaxies Survey (NGS; Gil de Paz et al. 2007). The *GALEX* FUV band covers $\lambda = 1350$–1750 Å with a resolution of 5.″6 and a 1.°25 diameter FOV. These maps have excellent sensitivity and well-behaved

backgrounds over a large FOV. *GALEX* simultaneously observes in a near-UV (NUV) band ($\lambda = 1750$–2750 Å). We use these data to measure UV colors and to identify foreground stars.

We correct the FUV maps for Galactic extinction using the dust map of Schlegel et al. (1998). We subtract a small background, measured away from the galaxy. We identify and remove foreground stars using their UV color: any pixel with a NUV-to-FUV intensity ratio of $\gtrsim 15$ (varying ± 5 from galaxy to galaxy) that is also detected in the NUV map with greater than 5σ significance is blanked. In convolution to our working resolution, blank pixels are replaced with the average of nearby data. We also blank a few regions with obvious artifacts. These include bright stars (e.g., in NGC 3198 and NGC 6946) that are usually beyond the optical radius of the galaxy and NGC 5195, the companion of NGC 5194.

D.1.2. SINGS 24 μm Maps

We use maps of 24 μm emission obtained as part of the SINGS Legacy program (Kennicutt et al. 2003), using the Multiband Imaging Photometer for *Spitzer* (MIPS) instrument (Rieke et al. 2004). Gordon et al. (2005) described the reduction of these scan maps, which have $6''$ resolution. The sensitivity and background subtraction are both very good, and it is typical to find 3σ emission at $\sim r_{25}$ in a spiral. The MIPS point-spread function (PSF) at 24 μm is complex at low levels, but our working resolution of $\sim 20''$ makes this only a minor concern.

NGC 3077, NGC 4214, and NGC 4449 are not part of SINGS. For these galaxies, we use 24 μm (and IRAC) maps from the *Spitzer* archive. We use the post basic calibrated data produced by the automated *Spitzer* pipeline.

As with the FUV maps, we subtract a small background from the 24 μm maps, which we measure away from the galaxy. We blank the same set of foreground stars as in the FUV maps. In convolution to our working resolution, these pixels are replaced with the average of nearby data. We also blank the edges of the 24 μm maps perpendicular to the scan, which are noisy (and outside the optical radius) and the same artifacts blanked in the FUV maps.

D.1.3. SINGS Hα

The SINGS fourth data release includes Hα maps, which we use to compare $\Sigma_{\rm SFR}$ derived from Hα, FUV, and 24 μm emission in 13 galaxies. We convert Hα to $\Sigma_{\rm SFR}$ following Calzetti et al. (2007) and the SINGS data release documentation. We correct for [N II] contamination following Calzetti et al. (2005) and Lee (2006) and correct for Galactic extinction using the Schlegel et al. (1998) dust maps. We check the flat-fielding by eye and mask regions or fit backgrounds where necessary.

D.2. Motivation for the FUV+24 to $\Sigma_{\rm SFR}$ Relation

Because 24 μm lies well short of the FIR peak for a typical galaxy spectral energy distribution (SED) (e.g., Dale & Helou 2002), a measurement in this band does not directly trace the total IR luminosity. Therefore, using 24 μm to measure embedded SFR relies on modeling of the IR SED or empirical calibration against other estimates of extinction. Calzetti et al. (2007) compared Hα and 24 μm with Paschen α (Paα) emission, a tracer of ionizing photons largely unaffected by extinction. They showed that a linear combination of Hα and 24 μm,

$$\begin{aligned} {\rm SFR_{Tot}} &= {\rm SFR_{H\alpha}^{unobscured}(H\alpha) + SFR_{H\alpha}^{embedded}(24\ \mu m)} \\ {\rm SFR_{Tot}} &= 5.3\times10^{-42}(L(H\alpha) + 0.031L(24\ \mu{\rm m})), \end{aligned} \tag{D2}$$

matches $\rm SFR_{Tot}$ inferred from Paα for 220 individual star-forming regions in 33 nearby galaxies and that the same calibration also works well when integrated over a large fraction of a galaxy disk. Here, $L(H\alpha)$ is the luminosity of Hα emission from the region in erg s^{-1} and $L(24\ \mu{\rm m}) = \nu_{24\ \mu{\rm m}} L_\nu(24\ \mu{\rm m})$, also in erg s^{-1}, is the specific luminosity of the region times the frequency at 24 μm. SFR is the SFR in that region in $M_\odot$ yr^{-1}.

We require an analogous formula to combine FUV and 24 μm data:

$${\rm SFR_{Tot}} = {\rm SFR_{FUV}^{unobscured}(FUV) + SFR_{FUV}^{embedded}(FUV, 24\ \mu m)}. \tag{D3}$$

The first term is the SFR implied by a particular FUV luminosity taking no account of internal extinction. The second term is the SFR that can be attributed to FUV light that does not reach us—that is, the extinction correction for the first term—which we infer from the 24 μm luminosity and may also depend on the ratio of FUV to 24 μm intensity.

We adopt the first term in Equation (D3) from Salim et al. (2007), who studied the relationship between FUV emission and SFR in ~50,000 galaxies, combining multiband photometry with population synthesis modeling and comparing to Hα emission. They found

$${\rm SFR_{FUV}^{unobscured}} = 0.68\times10^{-28} L_\nu({\rm FUV}), \tag{D4}$$

with SFR in $M_\odot$ yr^{-1} and L_ν(FUV) in erg s^{-1} Hz^{-1}. This yields SFRs ~30% lower than the relation given by Kennicutt (1998b) because of metallicity, model, and star formation history differences between their sample and Kennicutt's model.

We calibrate the second term in Equation (D3) in two ways: (1) we use simple assumptions to extrapolate $\rm SFR_{FUV}^{embedded}(FUV, 24\,\mu m)$ from $\rm SFR_{H\alpha}^{embedded}(24\,\mu m)$, which was measured by Calzetti et al. (2007), and (2) we make several independent estimates of $\rm SFR_{Tot}$—by comparing $\rm SFR_{Tot}$ with FUV emission, we directly measure the second term in Equation (D3). We phrase both analyses in terms of the factor $W_{\rm FUV}$, defined as

$$W_{\rm FUV}({\rm FUV}, 24\ \mu{\rm m}) = \frac{{\rm SFR_{FUV}^{embedded}}}{{\rm SFR_{H\alpha}^{embedded}}(24\ \mu{\rm m})}. \tag{D5}$$

The numerator is the second term in Equation (D3) and the denominator is the relation between embedded Hα and 24 μm emission measured by Calzetti et al. (2007, Equation (D2)). To measure $W_{\rm FUV}$, we combine Equations (D3) and (D5) to obtain

$$\begin{aligned} {\rm SFR_{Tot}} = {\rm SFR_{FUV}^{unobscured}(FUV)} &+ W_{\rm FUV}({\rm FUV}, 24\ \mu{\rm m}) \\ &\times {\rm SFR_{H\alpha}^{embedded}}(24\ \mu{\rm m}), \end{aligned} \tag{D6}$$

and solve for $W_{\rm FUV}$ in terms of measurable quantities:

$$W_{\rm FUV} = \frac{{\rm SFR_{Tot}} - {\rm SFR_{FUV}^{unobscured}(FUV)}}{{\rm SFR_{H\alpha}^{embedded}}(24\ \mu{\rm m})}. \tag{D7}$$

In order to estimate $W_{\rm FUV}$ over a LOS, we require FUV and 24 μm intensities and an estimate of $\rm SFR_{Tot}$.

D.2.1. Simple Extrapolation

In conjunction with a direct measurement, it is helpful to have a basic expectation for $W_{\rm FUV}$. We calculate this by combining a Galactic extinction law and a typical nebular-to-stellar extinction ratio. In terms of Hα extinction, $A_{\rm H\alpha}$, and FUV extinction, $A_{\rm FUV}$, Equations (D2) and (D3) are

$$\begin{aligned} {\rm SFR_{Tot}} &= {\rm SFR_{H\alpha}^{unobscured}} 10^{A_{\rm H\alpha}/2.5}, \\ {\rm SFR_{Tot}} &= {\rm SFR_{FUV}^{unobscured}} 10^{A_{\rm FUV}/2.5}. \end{aligned} \quad \text{(D8)}$$

For a Galactic extinction law, $A_{\rm FUV}/A_R \approx 8.24/2.33$ (Cardelli et al. 1989; Wyder et al. 2007). We may also expect that FUV originates from a slightly older and more dispersed population than Hα. If we assume a typical nebular-to-stellar extinction ratio of $A_{\rm H\alpha}/A_R \approx 2$ (Calzetti et al. 1994; Roussel et al. 2005), then we expect $A_{\rm FUV}/A_{\rm H\alpha} \approx 1.8$ (if FUV comes mostly from a very young population coincident with Hα, we instead expect $A_{\rm FUV}/A_{\rm H\alpha} \sim 3.6$). Combined with Equations (D3)–(D8), these assumptions yield

$$\begin{aligned} &\frac{1}{f + W_{\rm FUV} - 1} + 1 = \left(\frac{W_{\rm FUV}}{f} + 1\right)^{1/1.8} \text{ where} \\ &f = \frac{{\rm SFR_{FUV}^{unobscured}(FUV)}}{{\rm SFR_{H\alpha}^{embedded}}(24\ \mu{\rm m})}, \end{aligned} \quad \text{(D9)}$$

which we may solve for $W_{\rm FUV}$ given f, the ratio of observed FUV to 24 μm intensities (in SFR units).

For $A_{\rm H\alpha} = 1.1$ mag, a typical value in disk galaxies (Kennicutt 1998b), $f \approx 0.26$ and Equation (D9) suggests $W_{\rm FUV} \approx 1.3$. For higher $A_{\rm H\alpha}$, expected for the inner parts of spiral galaxies or arms, f will be lower and we expect lower values of $W_{\rm FUV}$, approaching $W_{\rm FUV} = 1$ where both FUV and Hα are almost totally absorbed (and $\rm SFR_{Tot}$ is totally determined from 24 μm emission). For lower $A_{\rm H\alpha}$, for example, expected in dwarf galaxies or the outer parts of spirals, we expect $W_{\rm FUV}$ to approach the ratio of extinctions, 1.8, in the optically thin case.

D.2.2. Measuring W_{FUV}

We measure $W_{\rm FUV}$ directly from observations by comparing FUV and 24 μm emission to various estimates of $\rm SFR_{Tot}$. We perform these tests in the 13 galaxies with SINGS Hα data. Over a common set of LOSs where we estimate Hα, FUV, and 24 μm to all be complete, we estimate $\Sigma_{\rm SFR}$ and $W_{\rm FUV}$ (from Equation (D7)) in five ways, as follows.

1. Combining Hα+24 μm using Equation (D2) (Calzetti et al. 2007).
2. From 24 μm emission alone, using the (nonlinear) relation found by Calzetti et al. (2007, their Equation 8).
3. From Hα alone, taking $A_{\rm H\alpha} = 1.1$ mag, a typical extinction averaged over disk galaxies, though not necessarily a good approximation for each LOS (Kennicutt 1998b).
4. From Hα emission, estimating $A_{\rm H\alpha}$ from $\Sigma_{\rm H\,I}$ and $\Sigma_{\rm H_2}$ following Wong & Blitz (2002). We assume a Galactic dust-to-gas ratio and treat dust associated with H I as a foreground screen obscuring Hα while treating dust associated with H_2 as evenly mixed with Hα emission.
5. From FUV emission, estimating $A_{\rm FUV}$ for every LOS by applying the relationship between FUV-to-NUV color and $A_{\rm FUV}$ measured for nearby galaxies by Boissier et al. (2007).

In principal, the first method is superior to the others because Calzetti et al. (2007) directly calibrated it against Paα, and because it incorporates both Hα and IR emission, offering direct tracers of both ionizing photons and dust-absorbed UV light. The other four methods offer checks on $\rm SFR_{Tot}$ that are variously independent of 24 μm, FUV, or Hα emission, allowing us to estimate the plausible range of both $W_{\rm FUV}$ and the uncertainty in $\Sigma_{\rm SFR}$.

D.2.3. Derived Relation

Figure 22 shows the results of these calculations. In the top panel, we plot the normalized distribution of $W_{\rm FUV}$ for each estimate of $\Sigma_{\rm SFR}$. The bottom left panel shows how each distribution of $W_{\rm FUV}$ depends on the FUV-to-24 μm ratio, f (Equation D9). The bottom right panel shows how $W_{\rm FUV}$ varies with normalized galactocentric radius.

The median $W_{\rm FUV}$ derived in various ways spans a range from ~1.0–1.8. The two 24 μm-based methods (blue and gray) both yield $W_{\rm FUV} \sim 1.3$ with relatively narrow distributions. Using FUV and UV colors yields the highest expected $W_{\rm FUV}$, ~1.8; estimating $A_{\rm H\alpha}$ from gas yields the lowest $W_{\rm FUV}$, peaked near ~1.0, though the distribution is very wide. This range of values reasonably agrees with our extrapolation (seen as a dash-dotted curve in the top right panel), which also lead us to expect a typical $W_{\rm FUV}$ of 1.3 and a reasonable range of 1.0–1.8.

The bottom panels show that while individual methods to estimate $W_{\rm FUV}$ do exhibit significant systematics (particularly at very high and low f), simply fixing $W_{\rm FUV} = 1.3$ is a reasonable description of most data (the dashed lines in the center panel bracket ~80% of the measured f). $W_{\rm FUV}$ does not have to be constant. Indeed, we expect it to vary with f based on simple assumptions and very basic arguments. However, a constant $W_{\rm FUV}$ is consistent with the data and is also the simplest, most conservative approach. Therefore, this is how we proceed: taking $W_{\rm FUV} = 1.3^{+0.5}_{-0.3}$, Equation (D3) becomes

$$\begin{aligned} {\rm SFR_{Tot}} = 0.68 \times 10^{-28} L_\nu({\rm FUV}) + 2.14^{+0.82}_{-0.49} \\ \times 10^{-42} L(24\ \mu{\rm m}). \end{aligned} \quad \text{(D10)}$$

We convert Equation (D10) from luminosity to intensity units using $\nu_{24\,\mu{\rm m}} = 1.25 \times 10^{13}$ Hz, 1 MJy $= 10^{-17}$ erg s^{-1} Hz^{-1} cm^{-2}, and $L_\nu = 4\pi A I_\nu$, where A is the physical area subtended by the patch of sky being considered. This yields Equation (D1),

$$\Sigma_{\rm SFR} = 8.1 \times 10^{-2} I_{\rm FUV} + 3.2^{+1.2}_{-0.7} \times 10^{-3} I_{24}, \quad \text{(D11)}$$

with $I_{\rm FUV}$ and I_{24} in units of MJy ster^{-1} and $\Sigma_{\rm SFR}$ in units of $M_\odot$ kpc^{-2} yr^{-1}.

D.2.4. Uncertainty in $\Sigma_{\rm SFR}$

In Figure 23, we plot our five alternate estimates of $\Sigma_{\rm SFR}$ (y-axis) as a function of $\Sigma_{\rm SFR}$ derived from Equation (D11) (x-axis). Each point corresponds to a 10″ wide tilted ring. In the bottom right panel, we plot the SFR integrated over the disk (over $r_{\rm gal} < r_{25}$) as a function of SFR estimated from nebular line emission by Kennicutt et al. (2003) and Hα by Lee (2006). Solid lines in all six panels show the line of equality plus or minus a factor of 2.

If we adopt the naive tack of treating all approaches as equal, the aggregate data in Figure 23 yield a median ratio

Σ_{SFR}(other)/Σ_{SFR}(FUV + 24) $\approx$ 1.05 with $\approx$ 0.22 dex (i.e., ~65%) 1σ scatter. The dominant sources of this scatter are the choice of "other" Σ_{SFR} and galaxy-to-galaxy variations. Once a galaxy and methodology are chosen, the data tend to follow a fairly well-defined and often nearly linear relation. For comparison, the 24 μm part of the Hα+24 μm calibration has $\approx$ 20%–30% uncertainty (Calzetti et al. 2007; Kennicutt et al. 2007), considering only star-forming peaks. In light of the wider range of star formation histories and geometries encountered working pixel by pixel or averaging over whole rings, the estimate of ~65% seems quite reasonable. Comparing our *integrated* SFRs (Figure 23, bottom right) with those estimated by 11HUGS (Lee 2006) and SINGS (Kennicutt et al. 2003) bears out this estimate; we match these estimates with a similar scatter. Another view of this comparison may be seen in Appendix F, where we present radial profiles of Σ_{SFR} based on Hα in the same plots as our FUV+24 μm profiles.

Despite the overall good agreement between our Σ_{SFR} and other estimates, Figures 22 and 23 do show systematic differences among tracers. We note several of these before moving on.

1. Using only 24 μm emission (gray) yields a low estimate of Σ_{SFR} for the two low metallicity galaxies in our comparison sample: Holmberg II and IC 2574. Dust is known to be deficient in these galaxies (Walter et al. 2007), which is likely to lead to a breakdown in the fit between 24 μm emission and Paα. This effect, already recognized by Calzetti et al. (2007), highlights the importance of including a non-IR component in a SFR tracer.
2. Estimating $A_{H\alpha}$ from gas (red; Wong & Blitz 2002) yields very high Σ_{SFR} (and high W_{FUV}) in the inner parts of galaxies. This underscores the complexity of the geometry and timescale effects at play; it is extremely challenging to reverse engineer the true luminosity of a heavily obscured source knowing only the amount of nearby interstellar matter. These high values are almost certainly overestimates; stellar feedback, turbulence, or simply favorable geometry likely always allow at least some light from deeply-embedded H II regions to escape.
3. Particularly at low Σ_{SFR}, inferring A_{FUV} from UV colors (purple) yields higher embedded SFR than using 24 μm emission (and this method appears to completely fail in NGC 6946, the horizontal row of points). A possible explanation is that where Σ_{SFR} is relatively low, the UV originates from a somewhat older (and thus redder) population (e.g., Calzetti et al. 2005); the FUV–NUV color relation depends on the recent star formation history (e.g., differing between starbursts and more quiescent galaxies; Boissier et al. 2007; Salim et al. 2007).

   This discrepancy (and the close association between our SFR tracer and stellar mass seen in the main text) argues for a comparison among metallicity, stellar populations, and mid-IR emission that is beyond the scope of this paper. We restrict ourselves to a first-order check: we compare the ratio of 24 μm-to-3.6 μm and FUV-to-3.6 μm emission in our sample with those in elliptical galaxies, which should be good indicators of how much an old population contributes to 24 μm or FUV emission. Very approximately, in ellipticals $I_{24}/I_{3.6} \sim 0.1$ (Temi et al. 2005; Dale et al. 2007; Johnson et al. 2007), with $\sim$ 0.03 expected from stellar emission alone (Helou et al. 2004), while $I_{FUV}/I_{3.6} \sim 2\text{–}4 \times 10^{-3}$ (Dale et al. 2007; Johnson et al. 2007, taking the oldest bin from the latter). We measure $I_{24}/I_{3.6}$ and $I_{FUV}/I_{3.6}$ for each ring in our sample galaxies and compare these to the elliptical colors. In both cases, only ~5% of individual tilted rings have ratios lower than those seen in elliptical galaxies and the mean color is ~10 times that found in elliptical galaxies, though the ratio $I_{FUV}/I_{3.6}$ shows large scatter due to the effects of extinction. Both the 24 μm and FUV bands do appear to be dominated by a young stellar population almost everywhere in our sample. Discrepancies among various tracers thus likely seem to arise from the different geometries and age sensitivities of FUV ($\tau \sim 100$ Myr), Hα ($\tau \sim 10$ Myr), and 24 μm (likely intermediate) emission.

Finally, we emphasize that uncertainties estimated via these comparisons mainly reflect the ability to accurately infer the total UV light or ionizing photon production from young stars. They do not include uncertainty in the IMF, ionizing photon production rate (e.g., at low metallicity), or any of the other factors involved in converting an ionizing photon count or FUV intensity into a SFR.

APPENDIX E

RADIAL PROFILES

Table 7 presents radial profiles of $\Sigma_{H\,I}$, Σ_{H_2}, Σ_*, and Σ_{SFR}. Combined with kinematics, which may be calculated by using Equation (B1) taking v_{flat} and l_{flat} from Table 4, these profiles are intended to provide a database that can be used to test theories of galaxy-wide star formation or to explore the effects of varying our assumptions. Results for all galaxies are available in an electronic table online. Table 7 in the print edition shows the results for our lowest-mass spiral galaxy, NGC 628, as an example.

The individual columns are as follows. *Ring identifiers:* (1) galaxy name; galactocentric radius of ring center (2) in kpc and (3) normalized by r_{25}. *Mass surface densities* (in $M_\odot$ pc^{-2}) along with associated uncertainty of (4–5) H I; (6–7) H_2; and (8–9) stars. *SFR surface density*, Σ_{SFR}, with associated uncertainty (10–11) from combining FUV and 24 μm emission in units of 10^{-4} $M_\odot$ yr^{-1} kpc^{-2}; and the individual contributions to Σ_{SFR} from (12) FUV and (13) 24 μm emission (i.e., the left and right terms in Equation (D1)) in the same units.

We derive radial profiles from maps using the mean (for $\Sigma_{H\,I}$, Σ_{H_2}, Σ_{SFR}) or median (Σ_*) value within 10″ wide tilted rings (so that the rings are spaced by half of our typical working resolution). The rings use the position angle and inclination in Table 4, adopted from Walter et al. (2008). We adopt the THINGS center for each galaxy (Trachternach et al. 2008; Walter et al. 2008) except for Holmberg I, where we use the dynamical center derived by Ott et al. (2001) rather than the photometric center. We consider only data within 60° of the major axis, measured in the plane of the galaxy. This minimizes our sensitivity to the adopted structural parameters, which most strongly affect the deprojection along the minor axis. Where there are no data, we take $\Sigma_{H\,I} = 0$ and $\Sigma_{H_2} = 0$. These are regions that have been observed but masked out because no signal was identified. We ignore pixels with no measurement of Σ_{SFR}; these are simply missing data.

We take the uncertainty in a quantity averaged over a tilted ring to be

$$\sigma = \frac{\sigma_{rms}}{\sqrt{N_{pix,ring}/N_{pix,beam}}}, \quad \text{(E1)}$$

Table 7
Table of Radial Profiles

Galaxy	r_{gal} (kpc)	r_{gal} (r_{25})	$\Sigma_{H\,I}$ ($M_\odot$ pc^{-2})	Σ_{H_2} ($M_\odot$ pc^{-2})	Σ_* ($M_\odot$ pc^{-2})	FUV+24	FUV Part	24 μm Part
						(10^{-4} $M_\odot$ yr^{-1} kpc^{-2})		
NGC 0628	0.2	0.02	1.6 ± 0.3	22.7 ± 1.2	1209.4 ± 18.3	105.1 ± 14.0	19.3	85.8
NGC 0628	0.5	0.05	2.1 ± 0.3	20.2 ± 1.3	557.8 ± 4.8	92.3 ± 9.9	17.1	75.1
NGC 0628	0.9	0.08	2.6 ± 0.4	16.1 ± 1.2	313.6 ± 1.0	76.7 ± 5.1	15.1	61.6
NGC 0628	1.2	0.12	3.1 ± 0.4	12.7 ± 0.8	231.9 ± 0.5	65.5 ± 4.2	14.2	51.3
NGC 0628	1.6	0.15	3.7 ± 0.3	11.4 ± 1.1	194.3 ± 0.5	62.2 ± 3.7	13.8	48.4
NGC 0628	1.9	0.19	4.6 ± 0.3	11.1 ± 1.2	163.5 ± 0.7	72.4 ± 12.2	15.3	57.1
NGC 0628	2.3	0.22	5.3 ± 0.4	11.1 ± 1.7	143.9 ± 0.8	90.2 ± 23.5	18.0	72.2
NGC 0628	2.7	0.25	5.8 ± 0.5	10.6 ± 1.9	123.5 ± 0.5	90.7 ± 21.3	19.1	71.6
NGC 0628	3.0	0.29	6.1 ± 0.5	8.9 ± 1.5	107.5 ± 0.4	71.9 ± 11.9	17.7	54.2
NGC 0628	3.4	0.32	6.5 ± 0.5	7.2 ± 1.2	151.0 ± 10.5	57.9 ± 8.5	15.7	42.2
NGC 0628	3.7	0.36	7.3 ± 0.7	6.2 ± 1.5	81.6 ± 0.4	55.8 ± 11.3	14.3	41.6
NGC 0628	4.1	0.39	7.9 ± 0.8	5.9 ± 1.7	68.0 ± 0.4	59.6 ± 14.1	13.5	46.1
NGC 0628	4.4	0.42	8.1 ± 0.8	5.4 ± 1.5	61.6 ± 0.4	59.9 ± 15.2	13.9	46.0
NGC 0628	4.8	0.46	7.9 ± 0.9	4.3 ± 1.1	48.3 ± 0.2	48.8 ± 11.0	13.6	35.2
NGC 0628	5.1	0.49	8.2 ± 1.0	3.1 ± 0.8	41.8 ± 0.2	37.4 ± 6.6	12.7	24.7
NGC 0628	5.5	0.53	8.5 ± 1.0	2.1 ± 0.7	37.0 ± 0.2	33.5 ± 8.7	12.3	21.2
NGC 0628	5.8	0.56	8.6 ± 0.8	1.2 ± 0.5	33.2 ± 0.4	30.2 ± 10.0	11.9	18.4
NGC 0628	6.2	0.59	8.6 ± 0.7	<1.0	37.0 ± 2.3	23.5 ± 6.5	10.1	13.5
NGC 0628	6.5	0.63	8.8 ± 0.6	<1.0	52.9 ± 6.1	17.4 ± 3.1	8.0	9.4
NGC 0628	6.9	0.66	8.8 ± 0.5	<1.0	19.5 ± 0.1	13.6 ± 1.9	6.6	7.0
NGC 0628	7.3	0.69	8.6 ± 0.5	<1.0	18.9 ± 0.1	11.6 ± 2.3	5.7	5.9
NGC 0628	7.6	0.73	8.2 ± 0.6	<1.0	18.7 ± 0.7	9.8 ± 2.2	5.1	4.8
NGC 0628	8.0	0.76	7.6 ± 0.6	<1.0	12.9 ± 0.1	7.5 ± 1.5	4.1	3.4
NGC 0628	8.3	0.80	7.1 ± 0.6	<1.0	17.6 ± 1.3	5.4 ± 0.9	3.1	2.3
NGC 0628	8.7	0.83	6.7 ± 0.5	<1.0	17.0 ± 1.6	4.1 ± 0.6	2.4	1.7
NGC 0628	9.0	0.86	6.5 ± 0.4	<1.0	10.8 ± 0.4	3.2 ± 0.4	2.0	1.3
NGC 0628	9.4	0.90	6.0 ± 0.5	<1.0	8.0 ± 0.1	2.5 ± 0.3	1.7	0.8
NGC 0628	9.7	0.93	5.2 ± 0.4	<1.0	7.5 ± 0.2	1.8 ± 0.3	1.3	0.5
NGC 0628	10.1	0.97	4.5 ± 0.4	<1.0	5.0 ± 0.1	1.2 ± 0.2	0.9	0.3
NGC 0628	10.4	1.00	4.1 ± 0.3	<1.0	4.1 ± 0.0	<1.0	...	...
NGC 0628	10.8	1.03	3.9 ± 0.3	<1.0	3.6 ± 0.0	<1.0	...	...
NGC 0628	11.1	1.07	3.9 ± 0.4	<1.0	3.9 ± 0.1	1.0 ± 0.4	0.7	0.3
NGC 0628	11.5	1.10	4.0 ± 0.4	<1.0	4.4 ± 0.2	<1.0	...	...
NGC 0628	11.9	1.13	4.3 ± 0.5	<1.0	9.5 ± 0.9	<1.0	...	...
NGC 0628	12.2	1.17	4.6 ± 0.5	<1.0	5.8 ± 0.2	<1.0	...	...

(This table is available in its entirety in machine-readable and Virtual Observatory (VO) forms in the online journal. A portion is shown here for guidance regarding its form and content.)

where σ_{rms} is the rms scatter within the tilted ring, $N_{pix,ring}$ is the number of pixels in the ring, and $N_{pix,beam}$ is the number of pixels per resolution element. This σ captures both random scatter in the data and variations due to the azimuthal structure within the ring. It does not capture systematic uncertainties, for example, due to a choice of X_{CO} or star formation tracer, discussed in these appendices.

APPENDIX F

ATLAS OF MAPS AND PROFILE PLOTS

In Figures 24–46, we present maps, profiles, and calculations for individual galaxies. Each page shows results for one galaxy. The top row shows maps of atomic gas ($\Sigma_{H\,I}$), molecular gas (Σ_{H_2}), and total gas ($\Sigma_{gas} = \Sigma_{H\,I} + \Sigma_{H_2}$). The second row shows unobscured (FUV), dust-embedded (24 μm), and total star formation surface density (Σ_{SFR}). These maps use a color scheme based on the modified magnitude system described by Lupton et al. (1999); a bar to the right of each row of plots illustrates the scheme. The gas maps and star formation rate maps for each galaxy use a single color scheme, but the scheme does vary from galaxy to galaxy, so care should be taken when comparing different galaxies. Also note that we construct the table to show empty values below our working sensitivity (i.e., any data below $\Sigma_{gas} = 1\,M_\odot$ pc^{-2} or $\Sigma_{SFR} = 10^{-4}\,M_\odot$ yr^{-1} kpc^{-2} appear as white) but the data (especially THINGS) often show evidence of real emission below this value. We refer the readers to the original data papers for more information on each data set.

The dotted circle indicates the optical radius, r_{25}, in the plane of the galaxy for the structural parameters given in Table 4. A small black circle in the bottom right panel shows our working resolution.

In the left panel on the third row, we plot mass surface density profiles. We show H I (blue), H_2 (magenta, where available), stars (red stars), and total gas (thick gray profile). Vertical dotted lines indicate 0.25, 0.5, 0.75, and 1.0 times r_{25}. Horizontal dotted lines show fixed mass surface density.

In the right panel on the third row, we plot SFR surface density profiles. We show the total Σ_{SFR} (thick gray profile) and the separate contributions from dust-embedded (green, 24 μm) and unobscured (blue, FUV) star formation, which add up to Σ_{SFR}. Where they are available, we plot Σ_{SFR} from the SINGS DR4 Hα (red) and points measured from the Hα profiles of

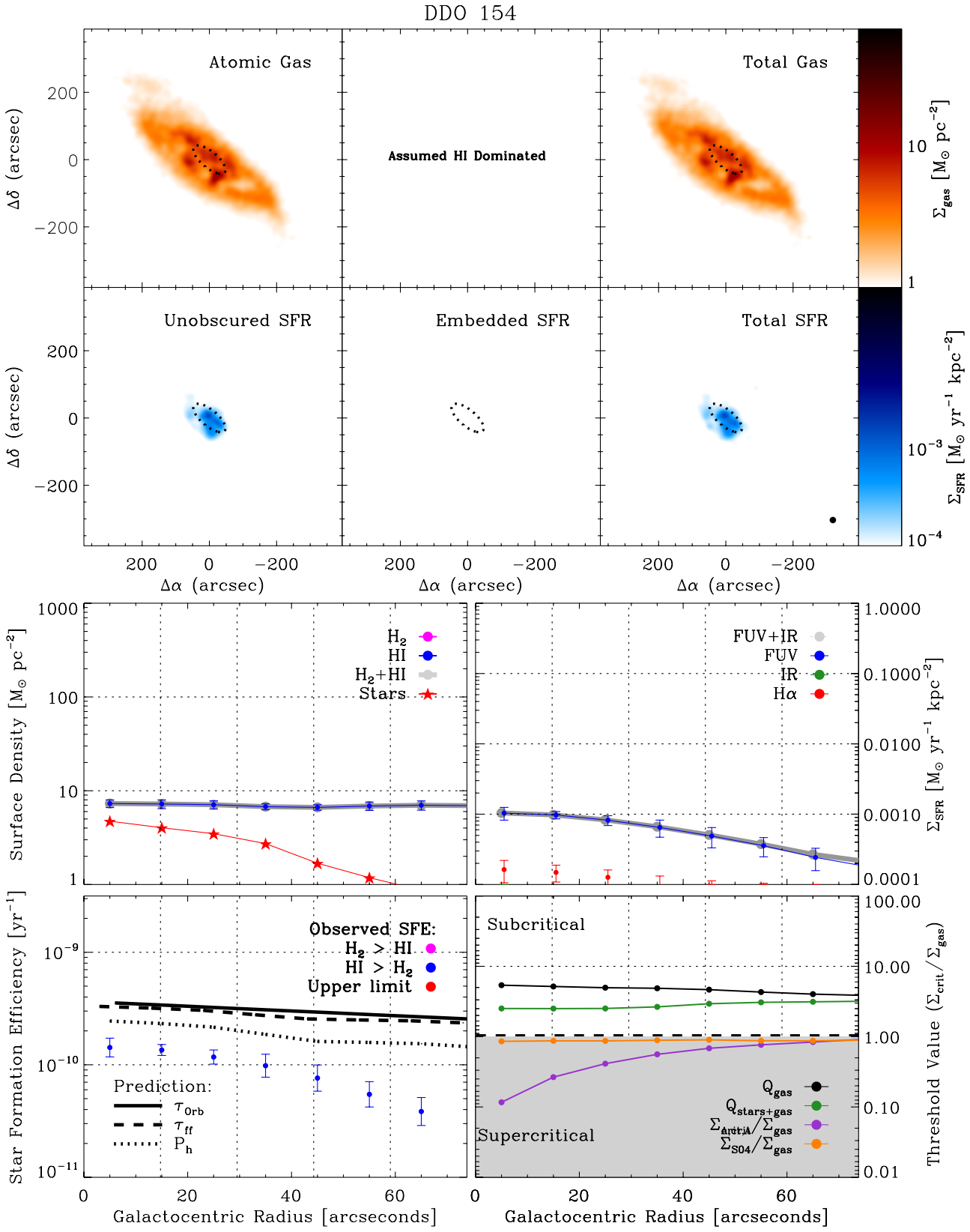

Figure 24. Atlas of data and calculations for DDO 154.

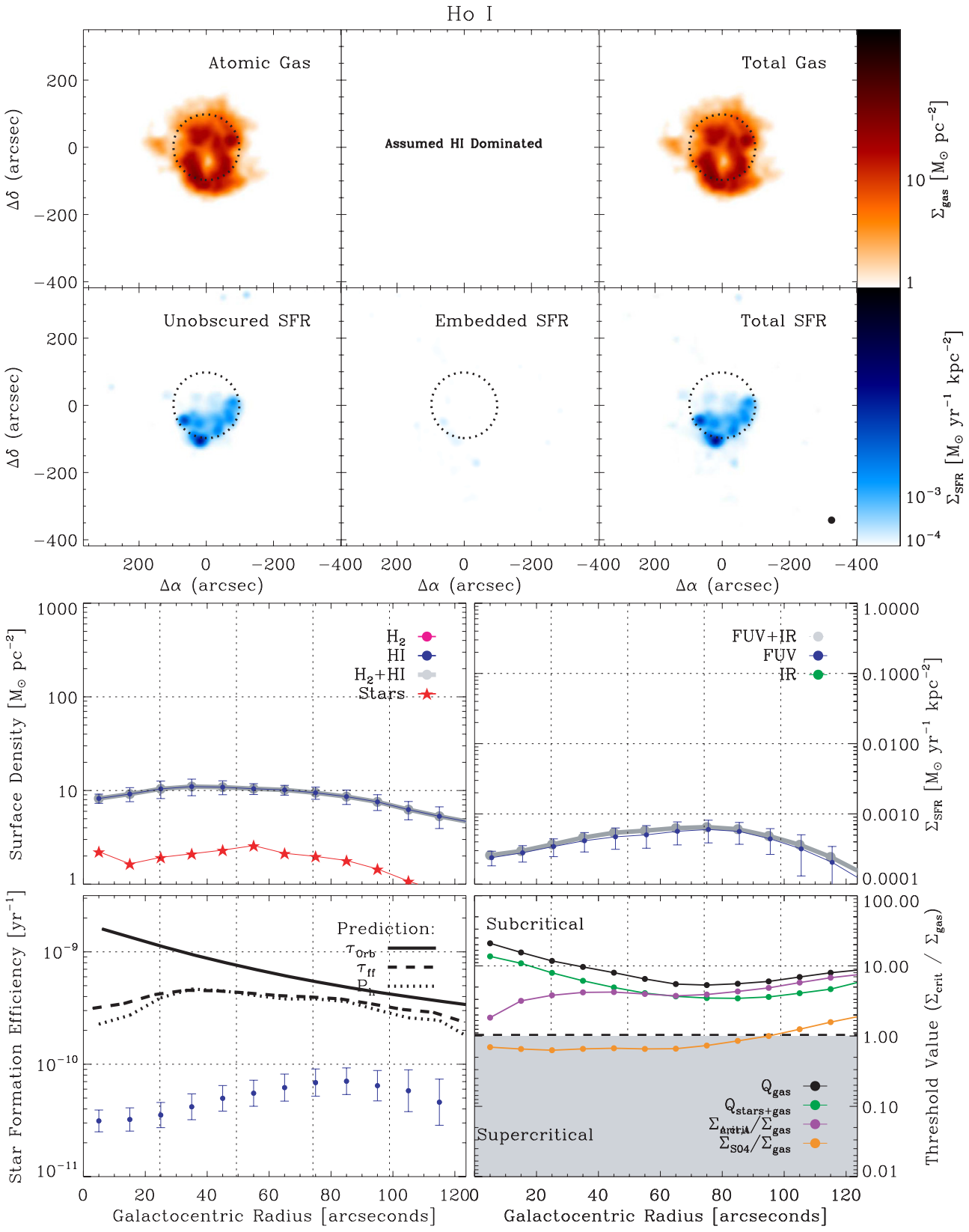

Figure 25. Atlas of data and calculations for Holmberg I.

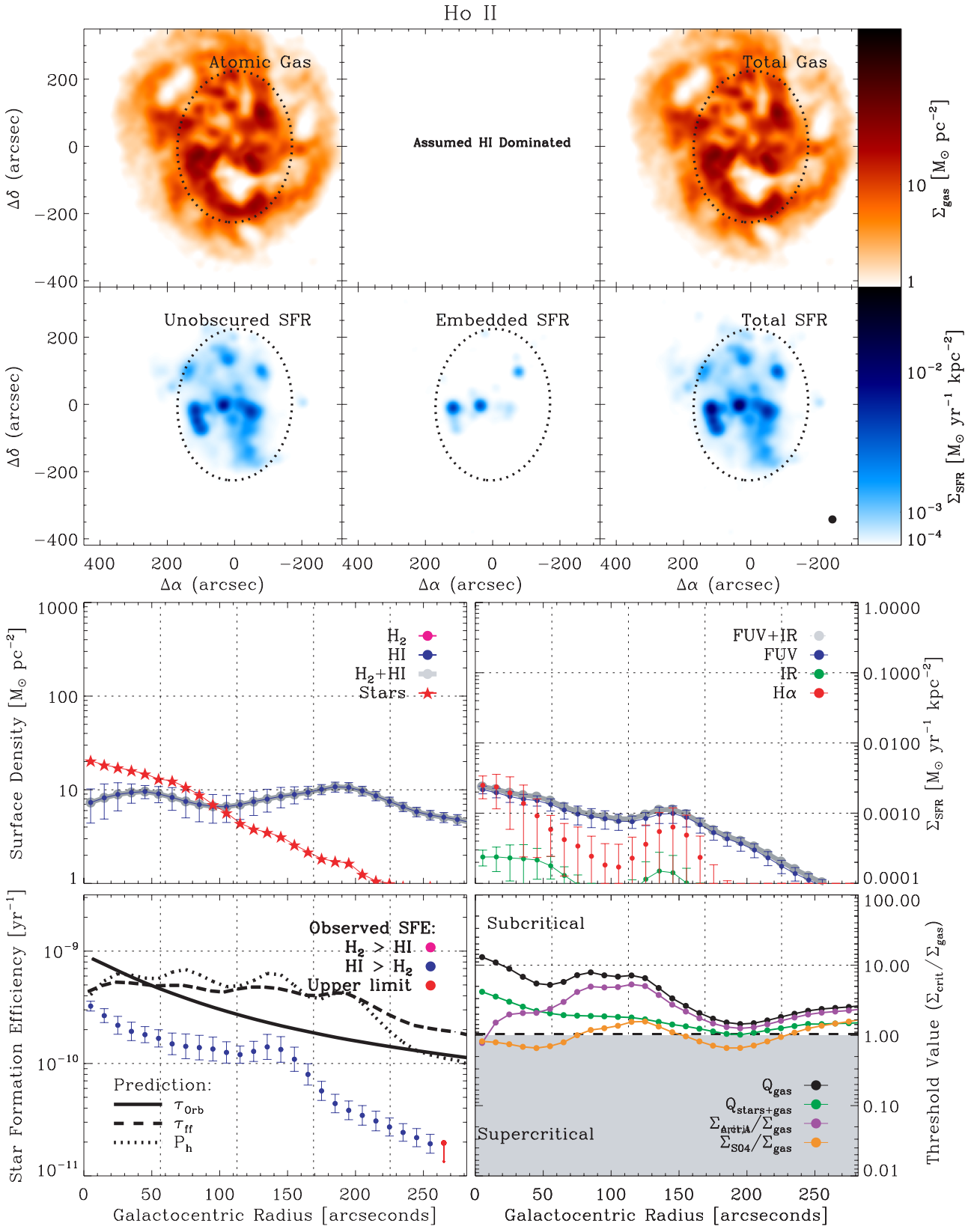

Figure 26. Atlas of data and calculations for Holmberg II.

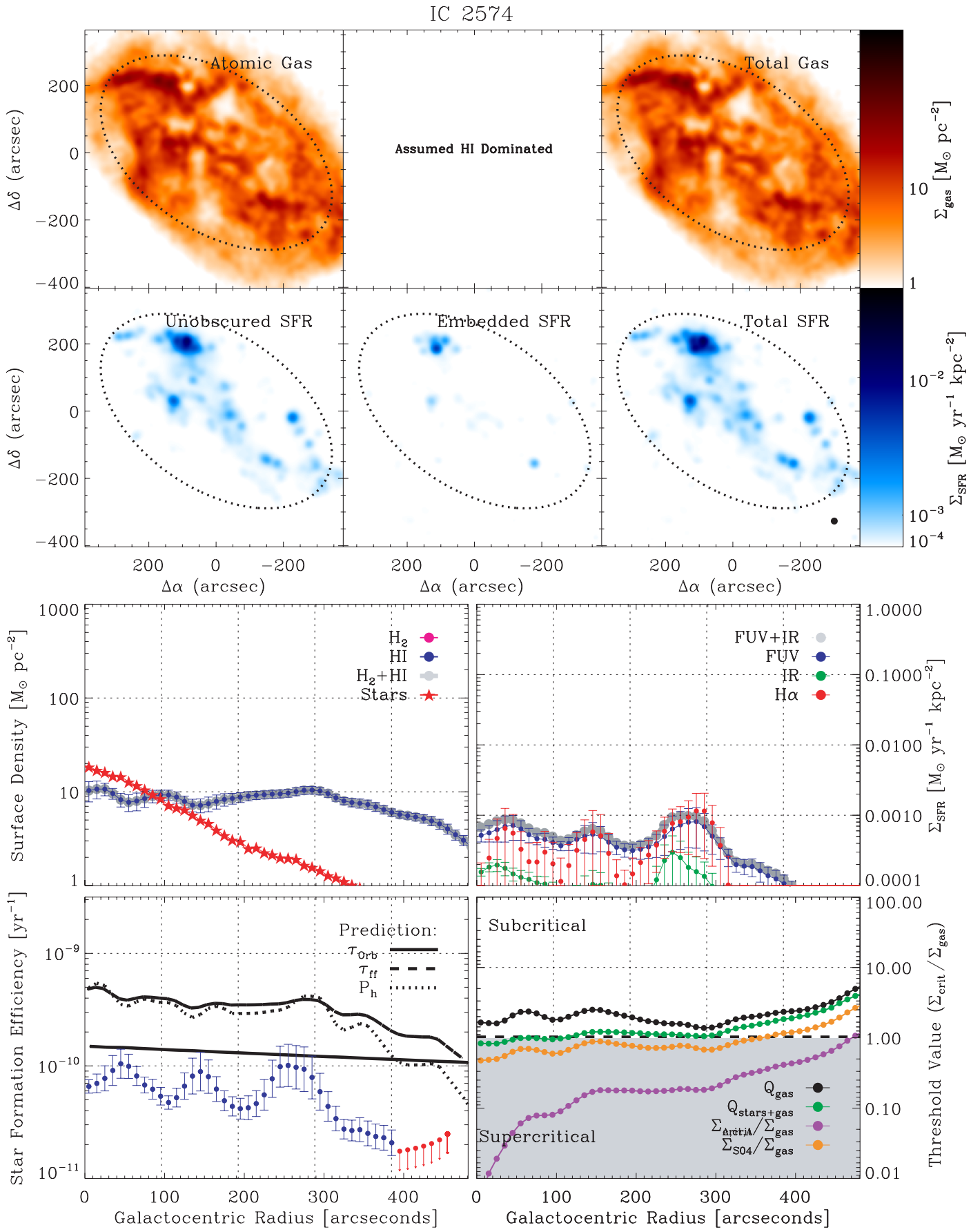

Figure 27. Atlas of data and calculations for IC 2574.

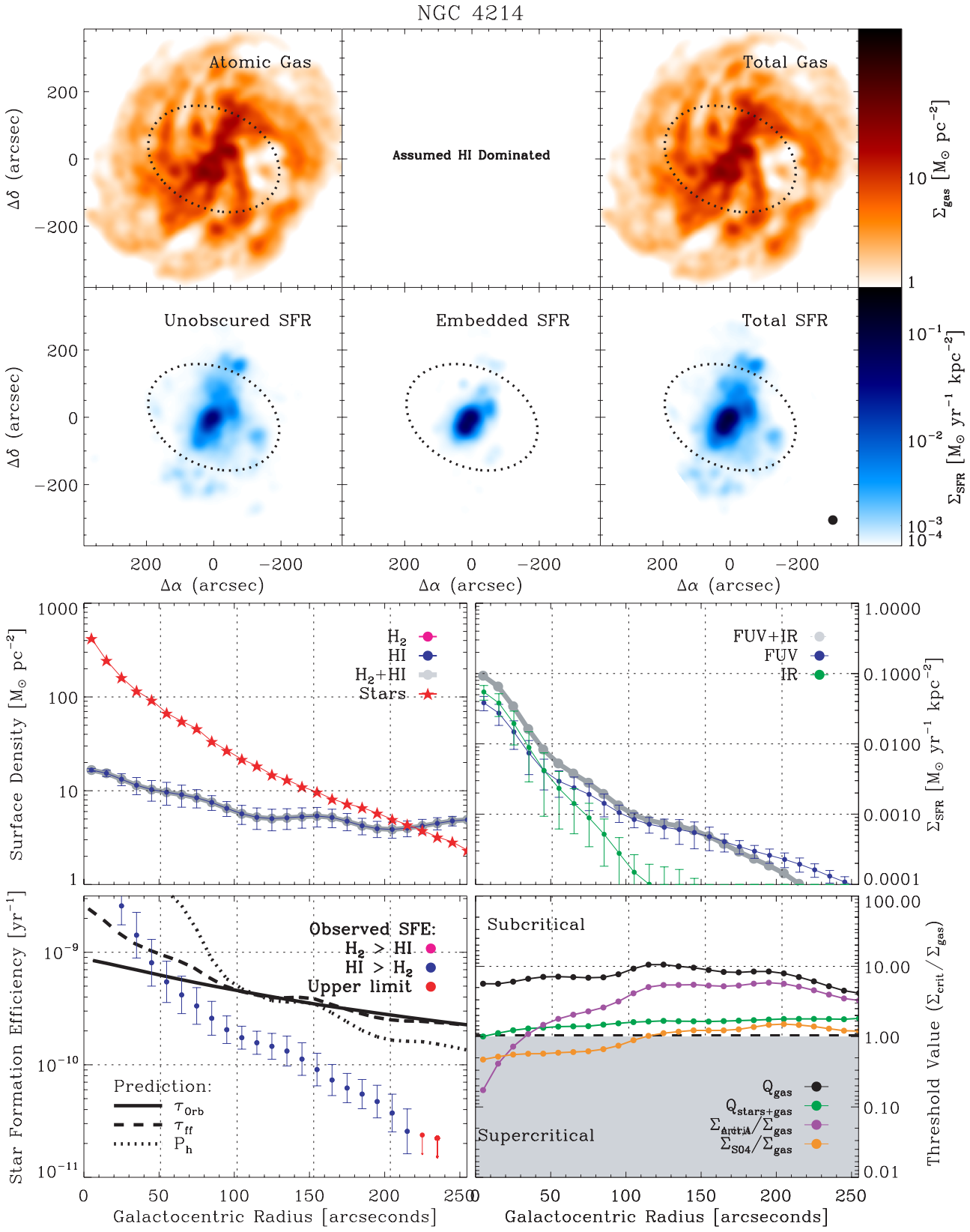

Figure 28. Atlas of data and calculations for NGC 4214.

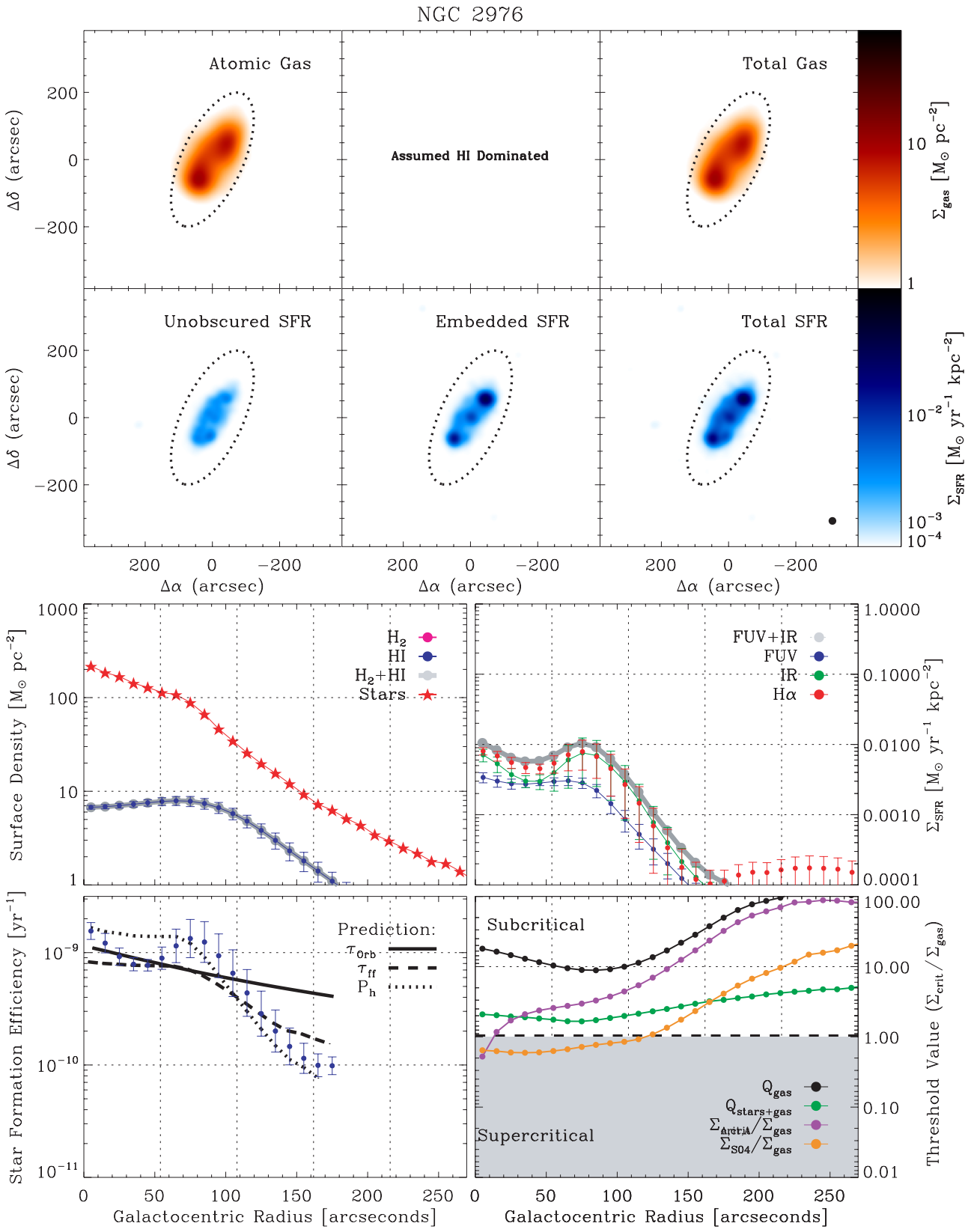

Figure 29. Atlas of data and calculations for NGC 2976.

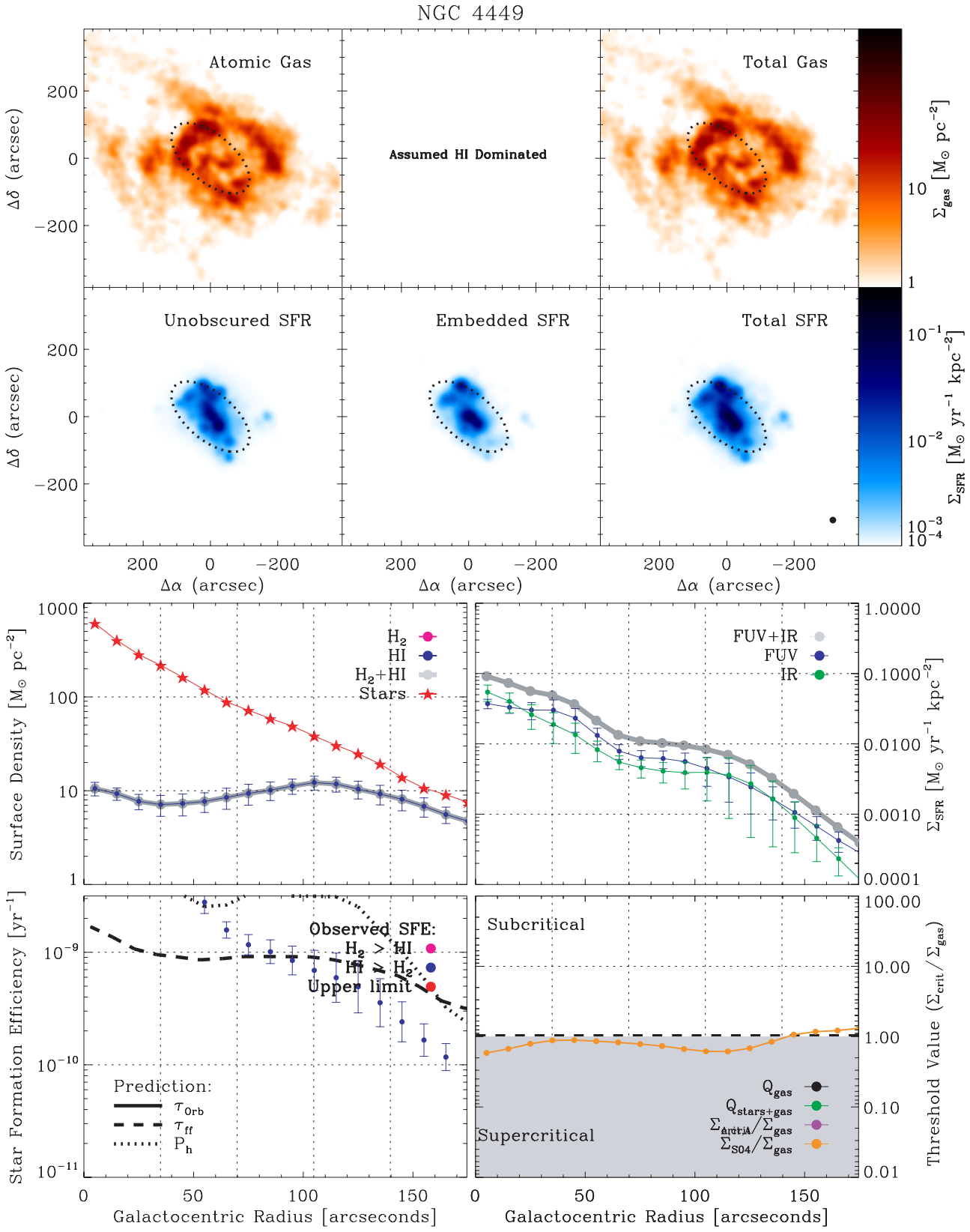

Figure 30. Atlas of data and calculations for NGC 4449.

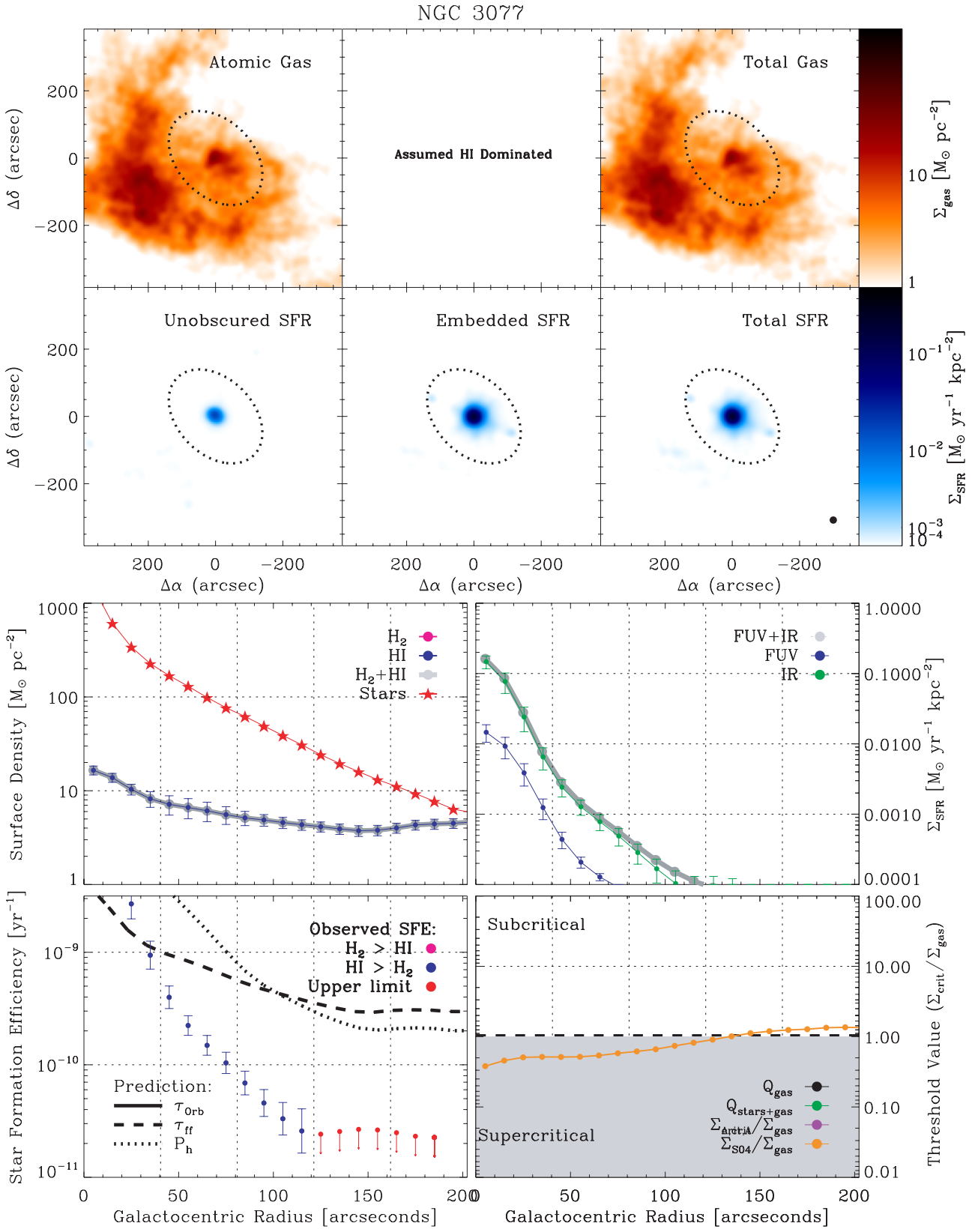

Figure 31. Atlas of data and calculations for NGC 3077.

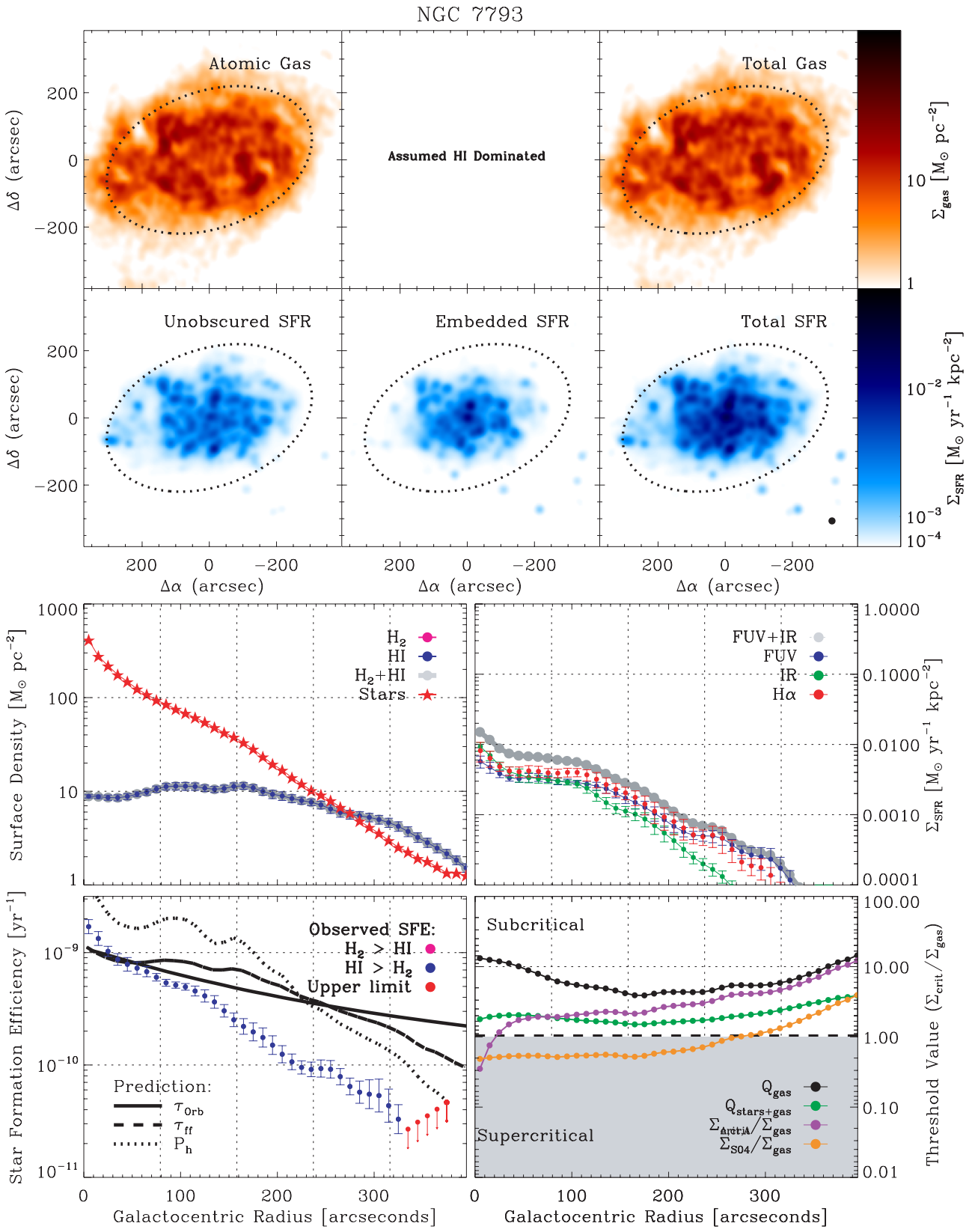

Figure 32. Atlas of data and calculations for NGC 7793.

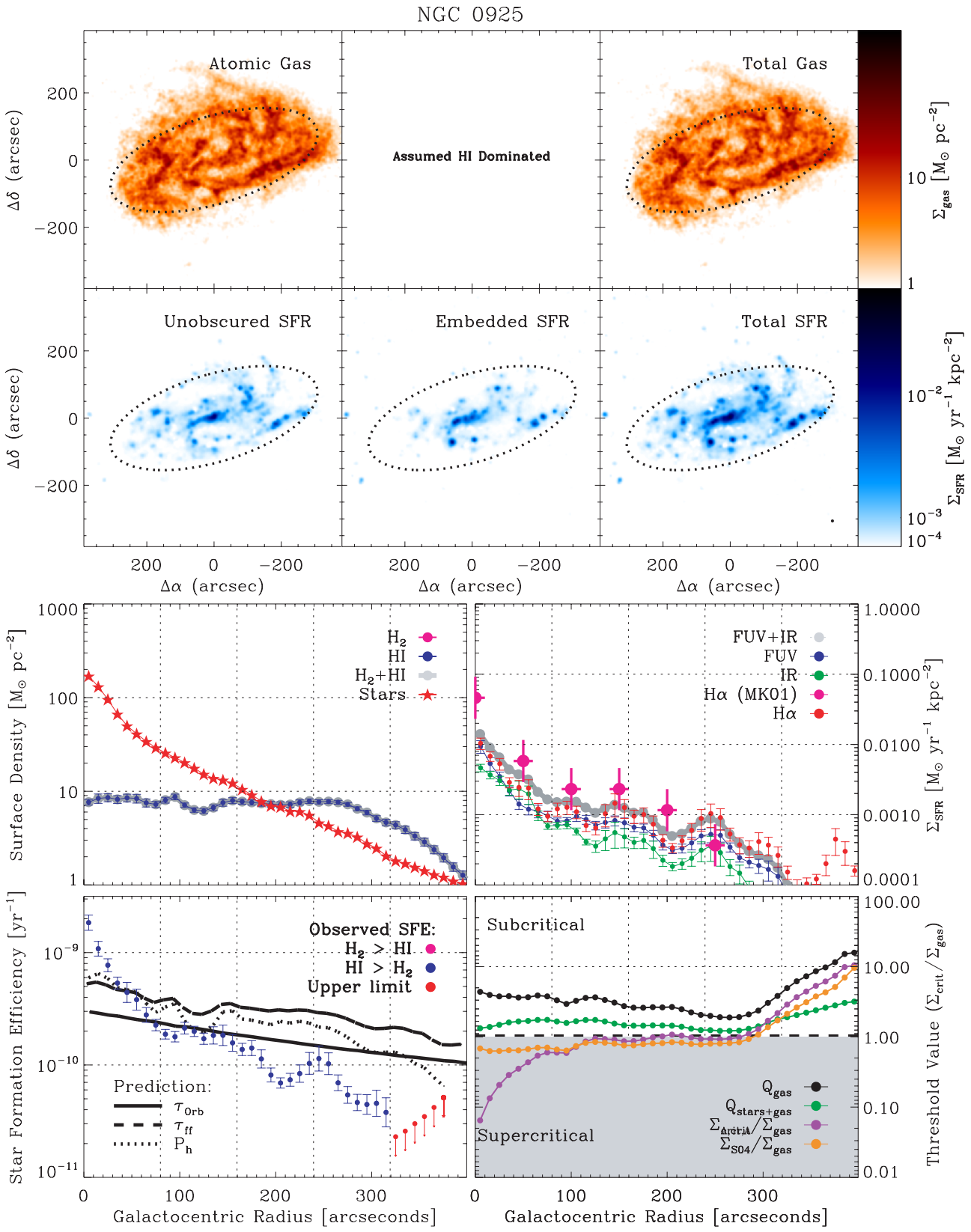

Figure 33. Atlas of data and calculations for NGC 925.

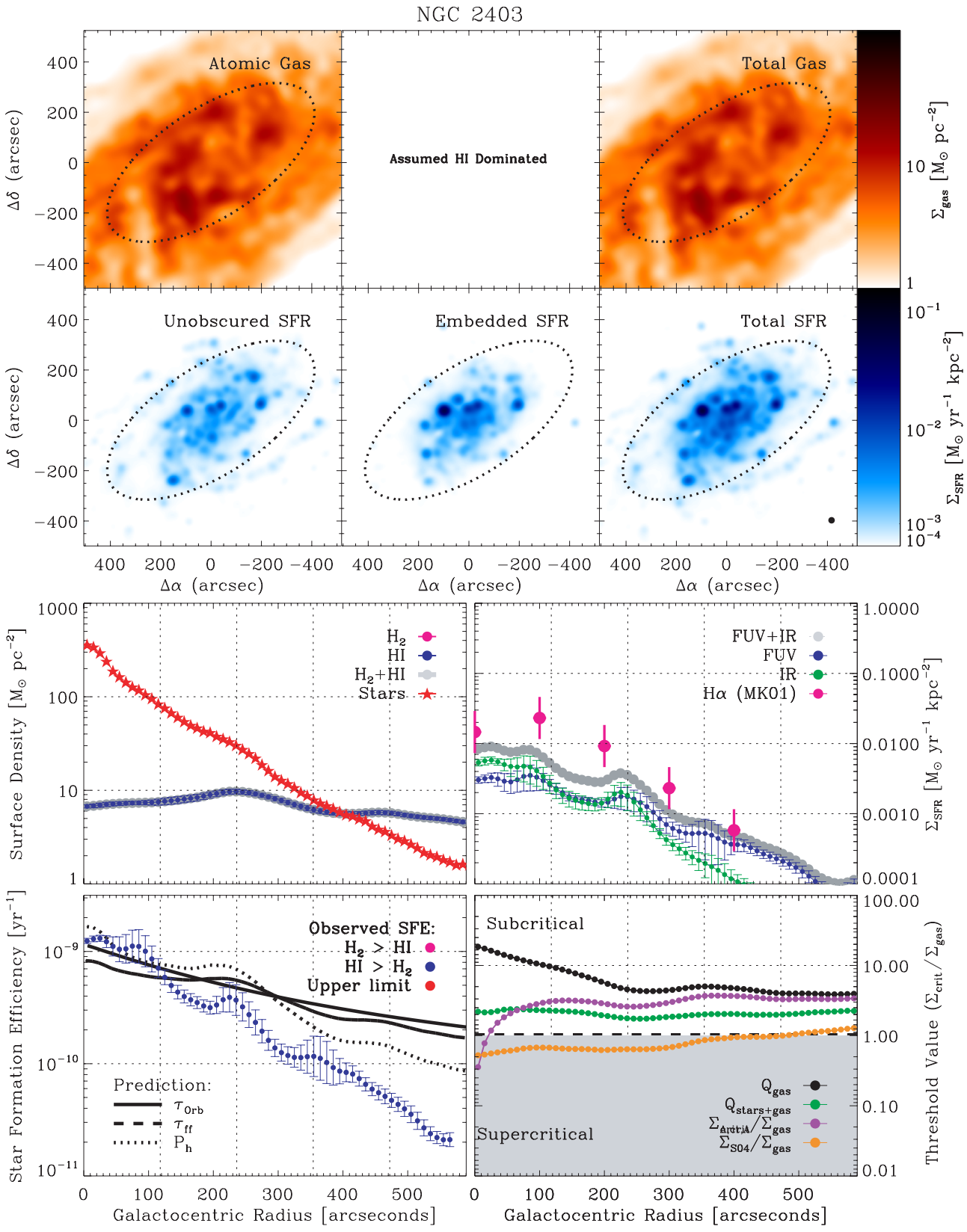

Figure 34. Atlas of data and calculations for NGC 2403.

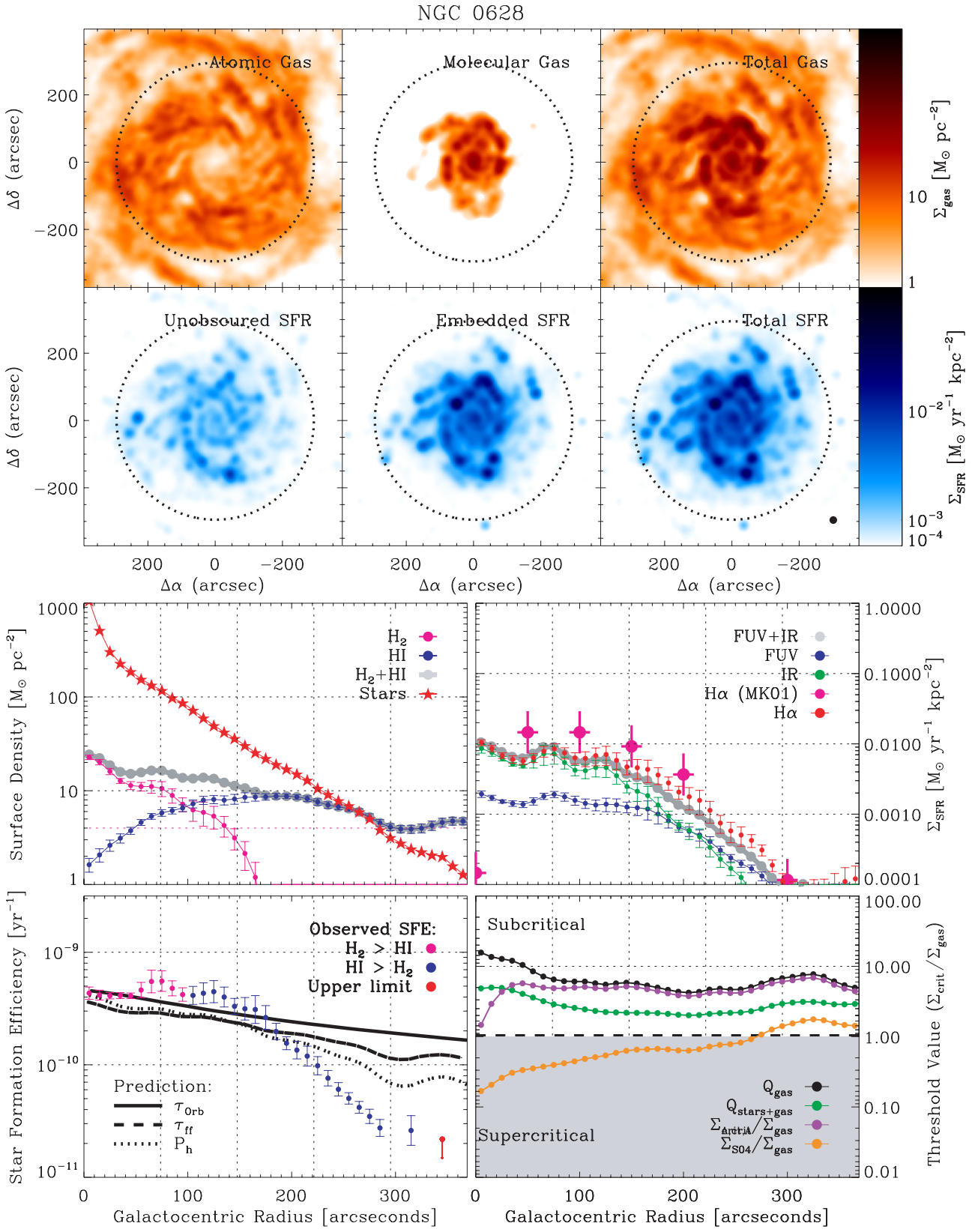

Figure 35. Atlas of data and calculations for NGC 628.

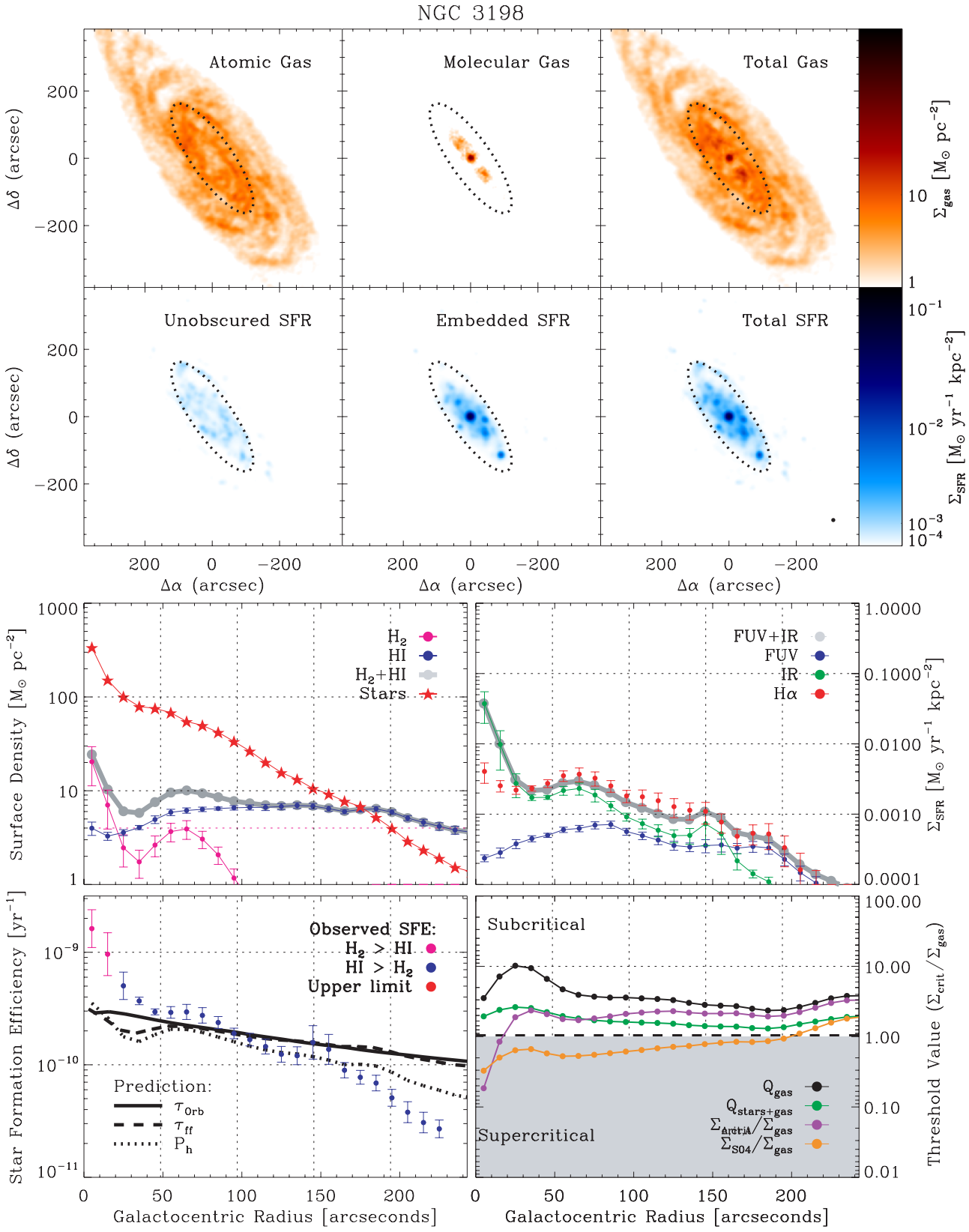

Figure 36. Atlas of data and calculations for NGC 3198.

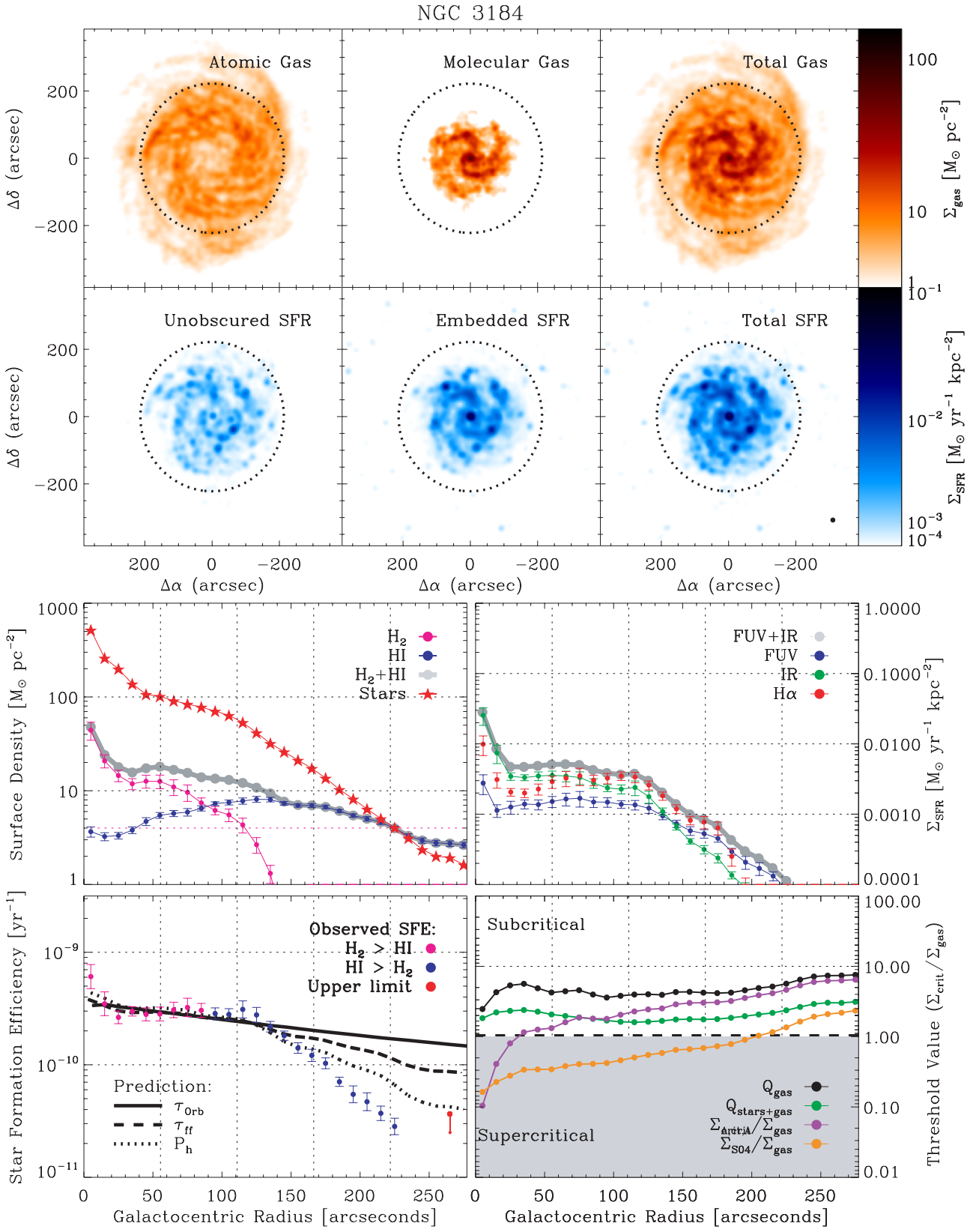

Figure 37. Atlas of data and calculations for NGC 3184.

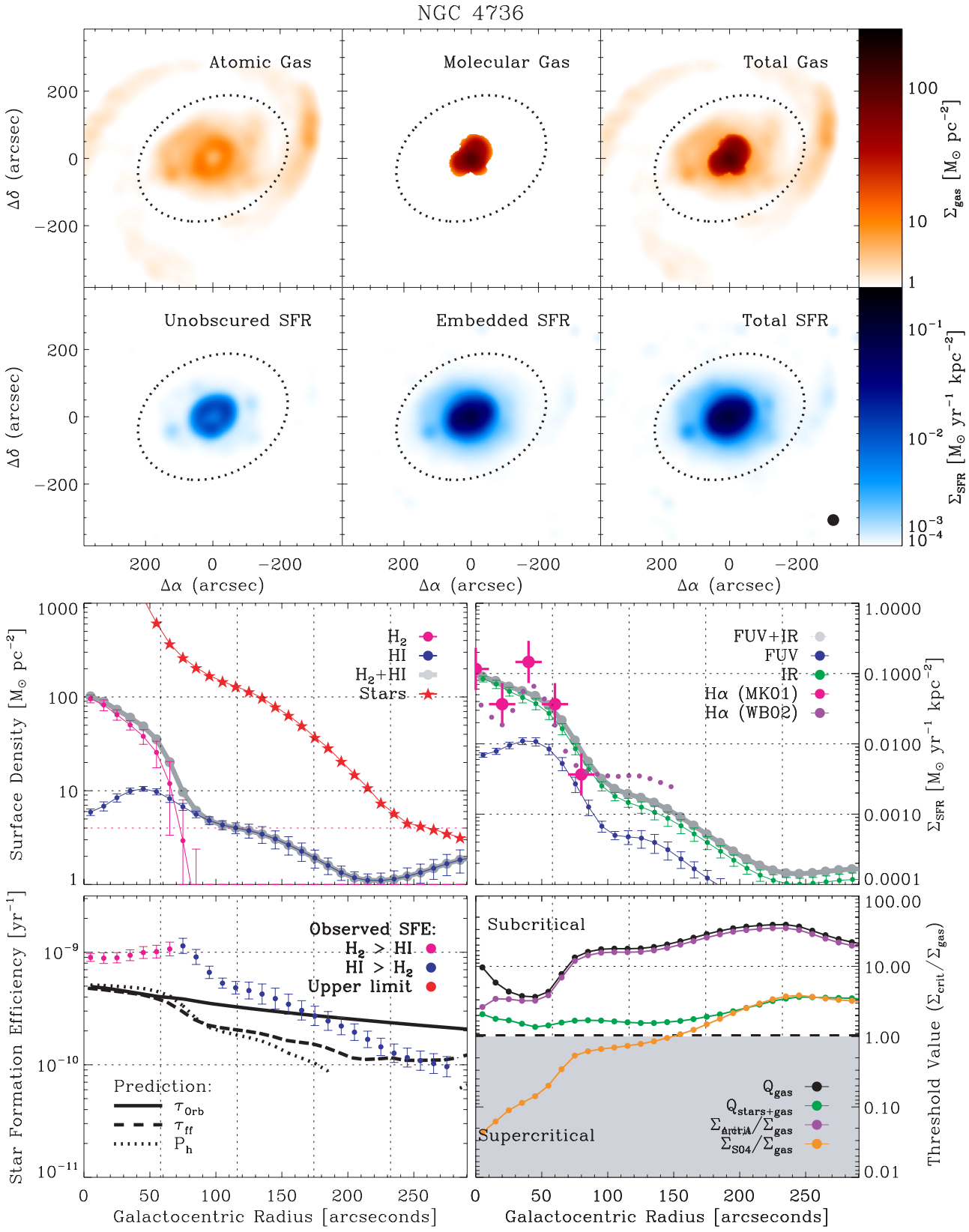

Figure 38. Atlas of data and calculations for NGC 4736.

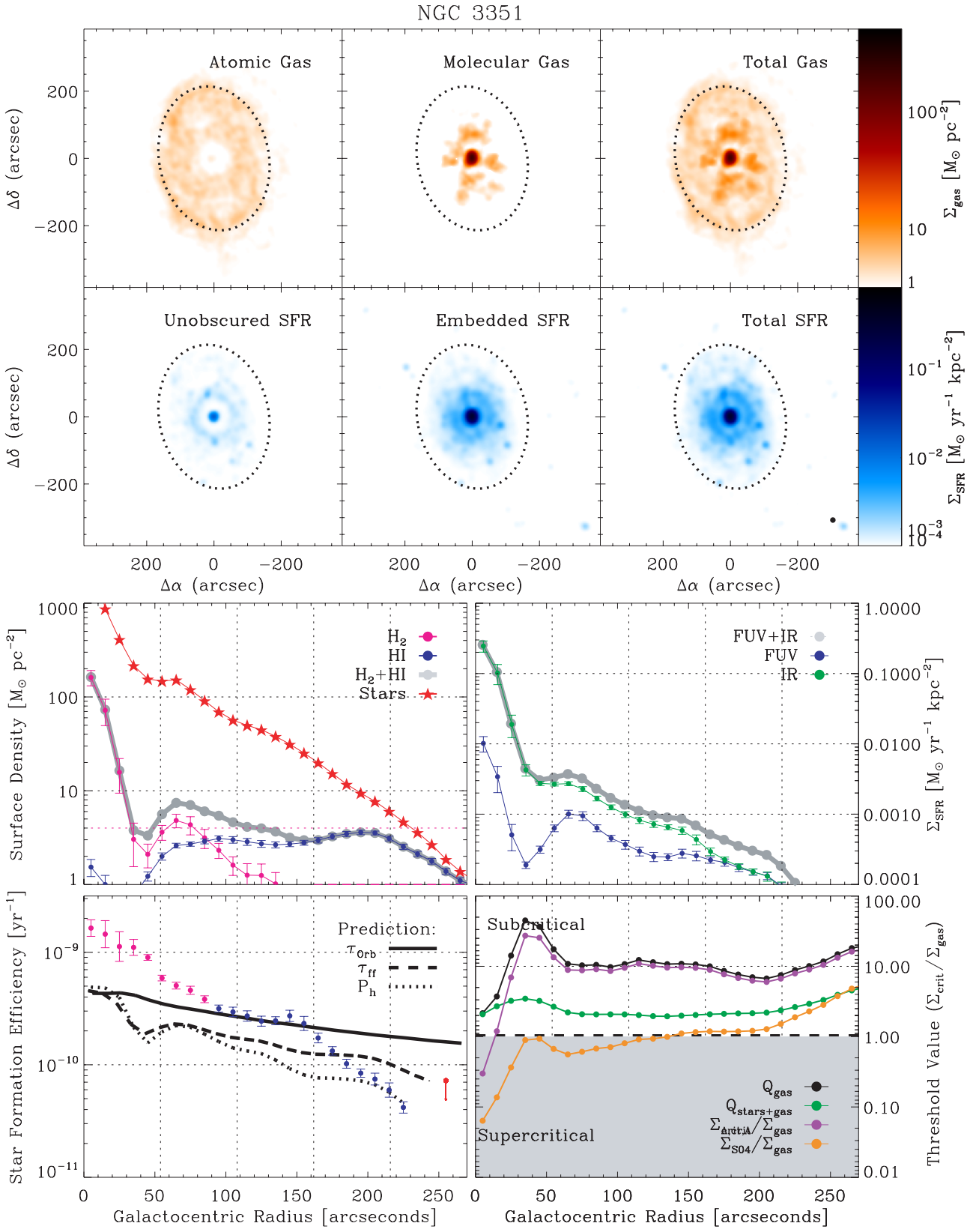

Figure 39. Atlas of data and calculations for NGC 3351.

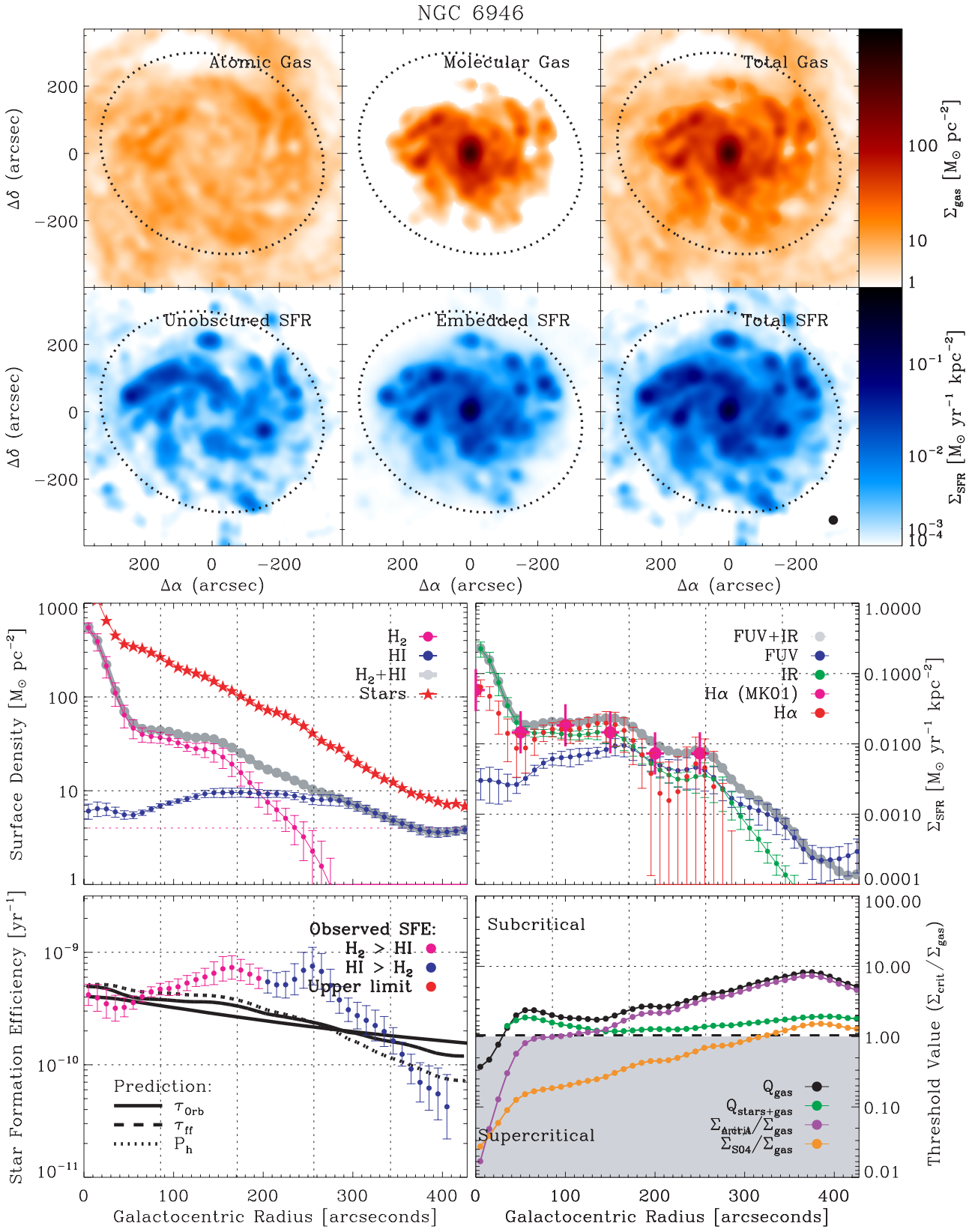

Figure 40. Atlas of data and calculations for NGC 6946.

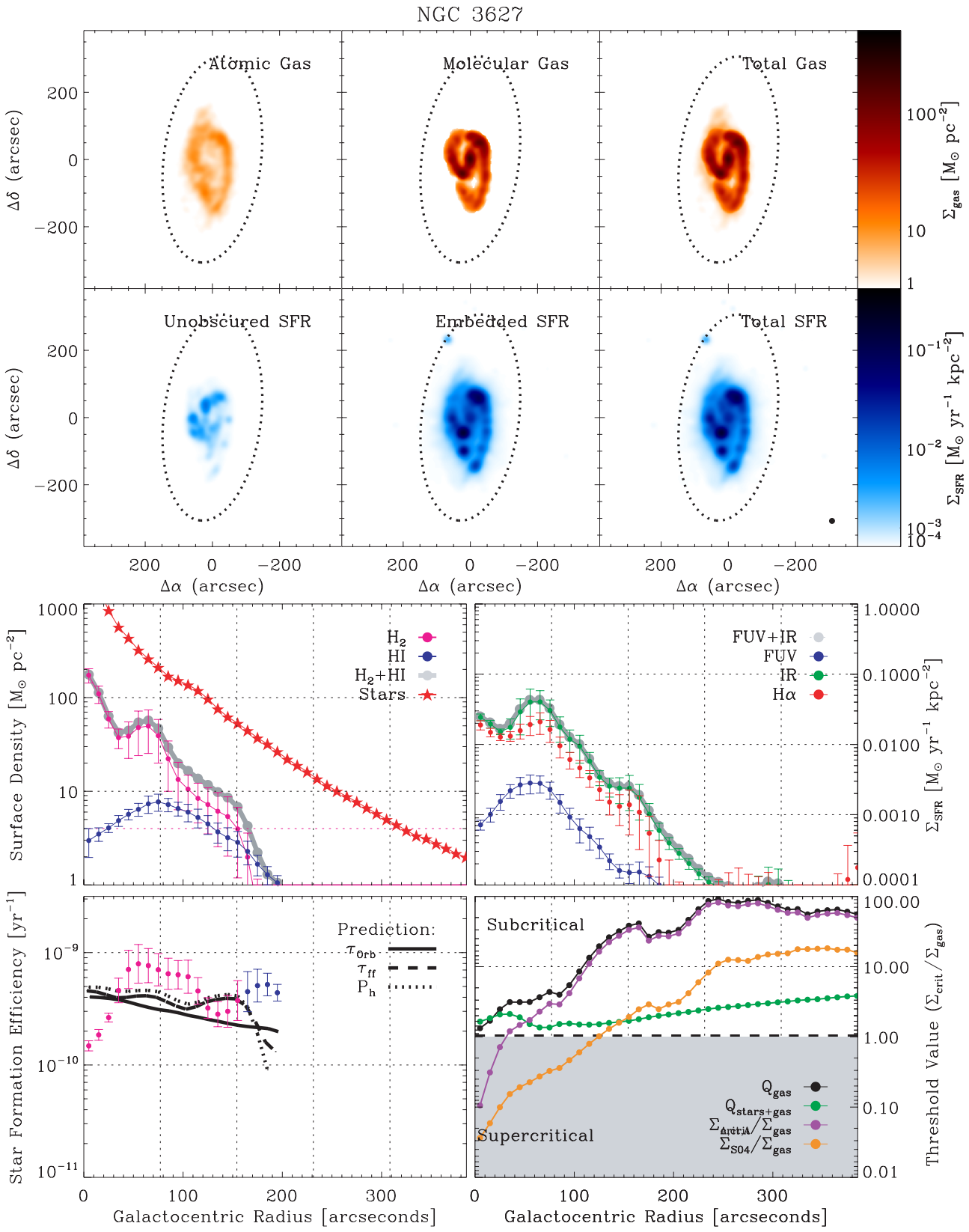

Figure 41. Atlas of data and calculations for NGC 3627.

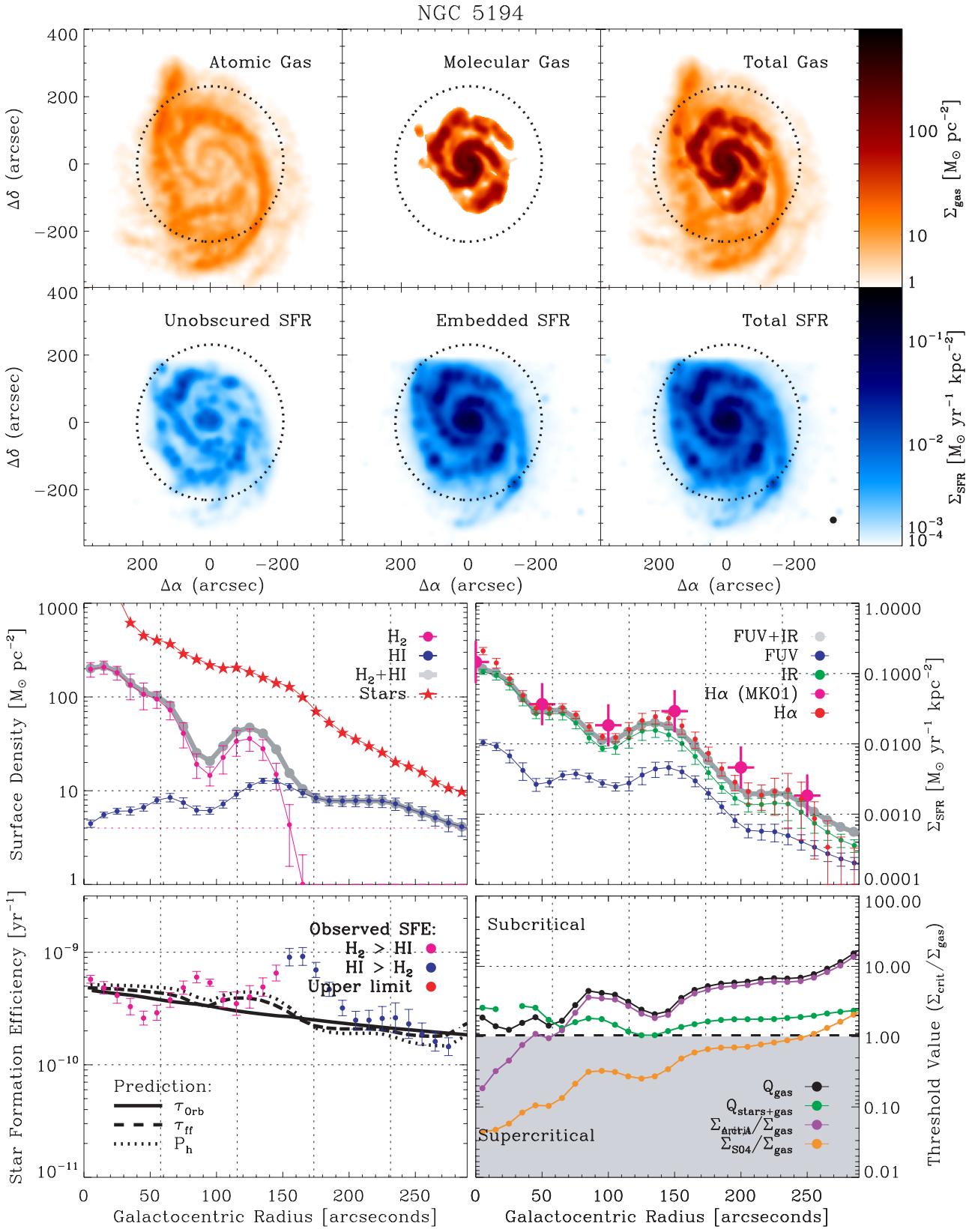

Figure 42. Atlas of data and calculations for NGC 5194.

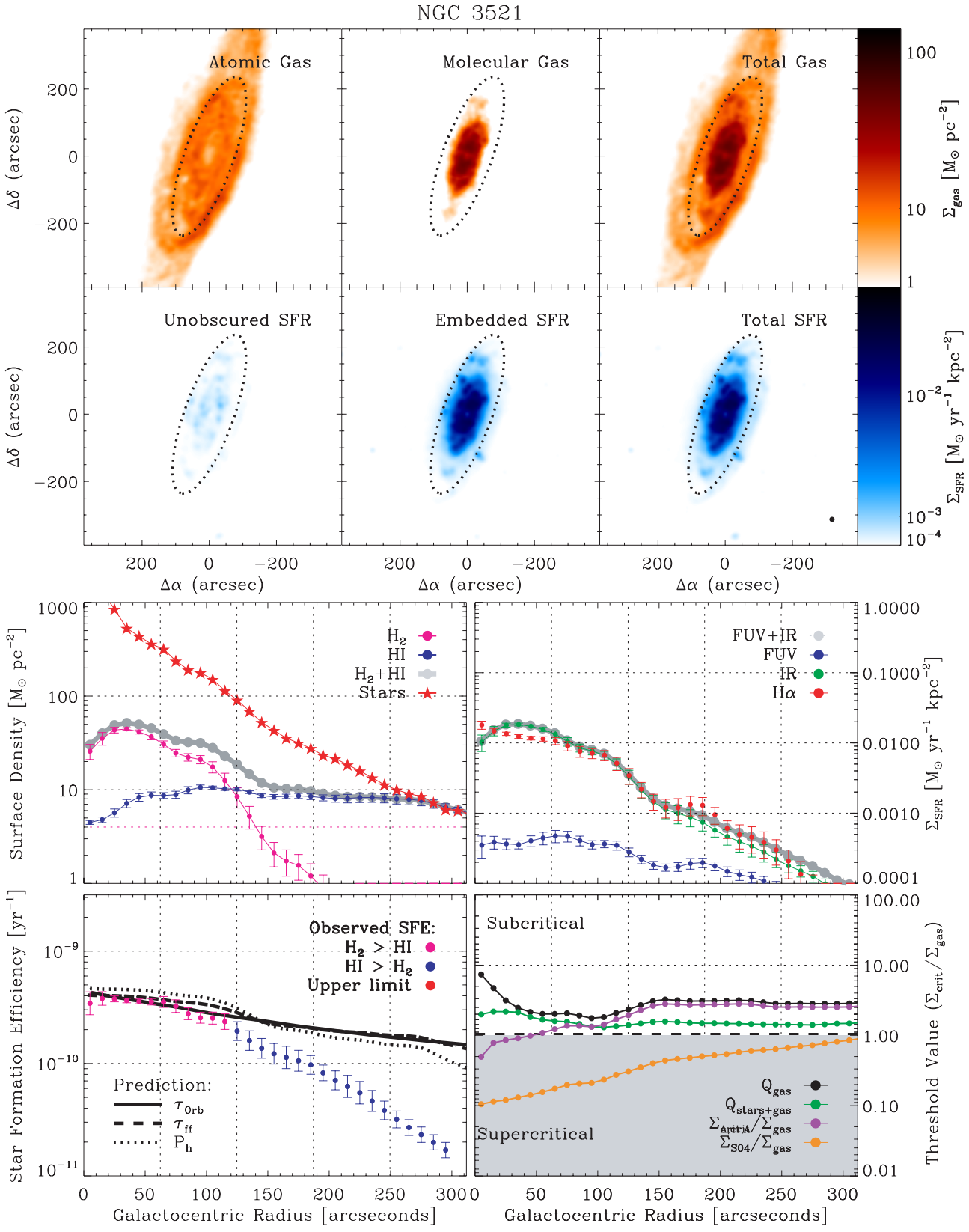

Figure 43. Atlas of data and calculations for NGC 3521.

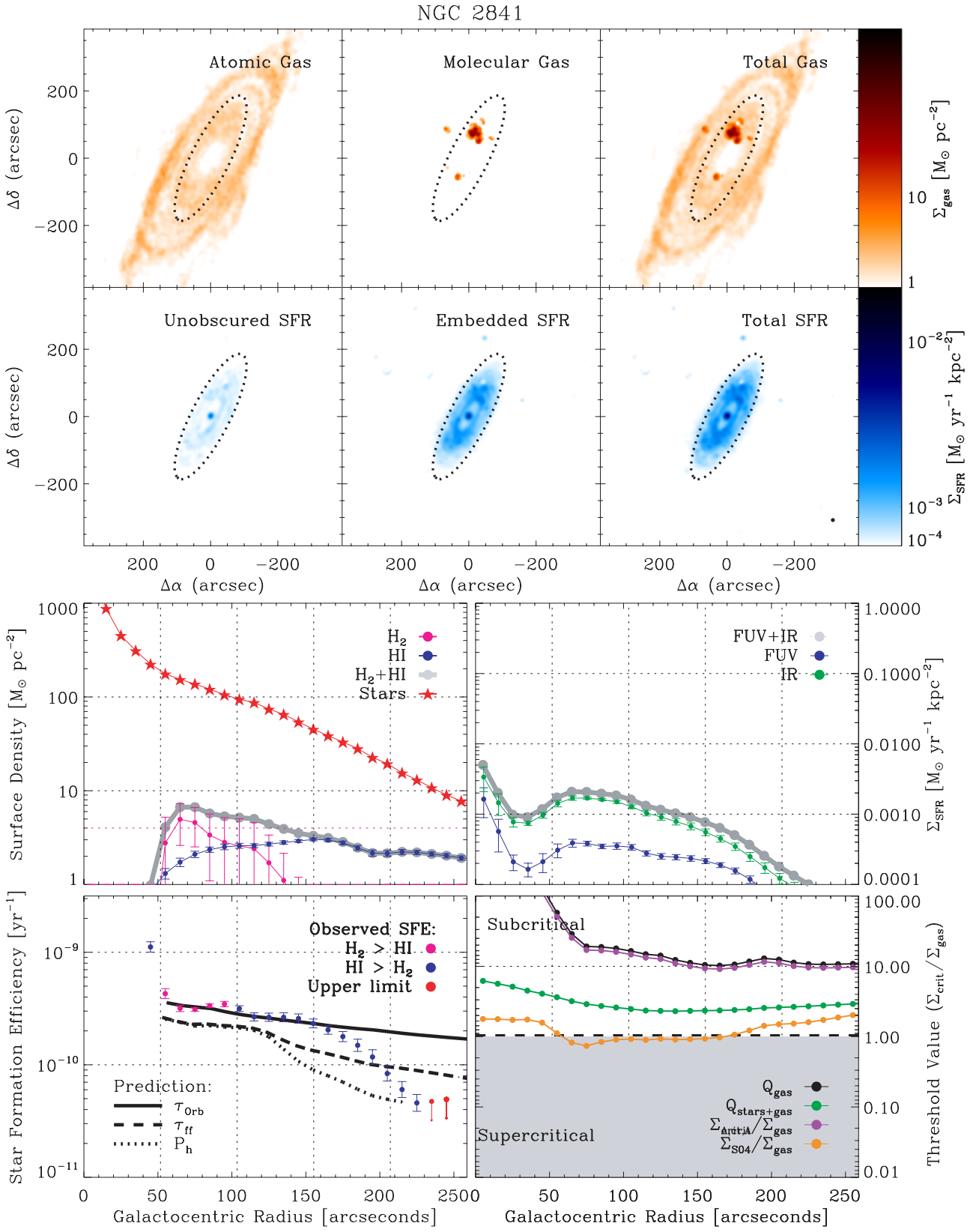

Figure 44. Atlas of data and calculations for NGC 2841.

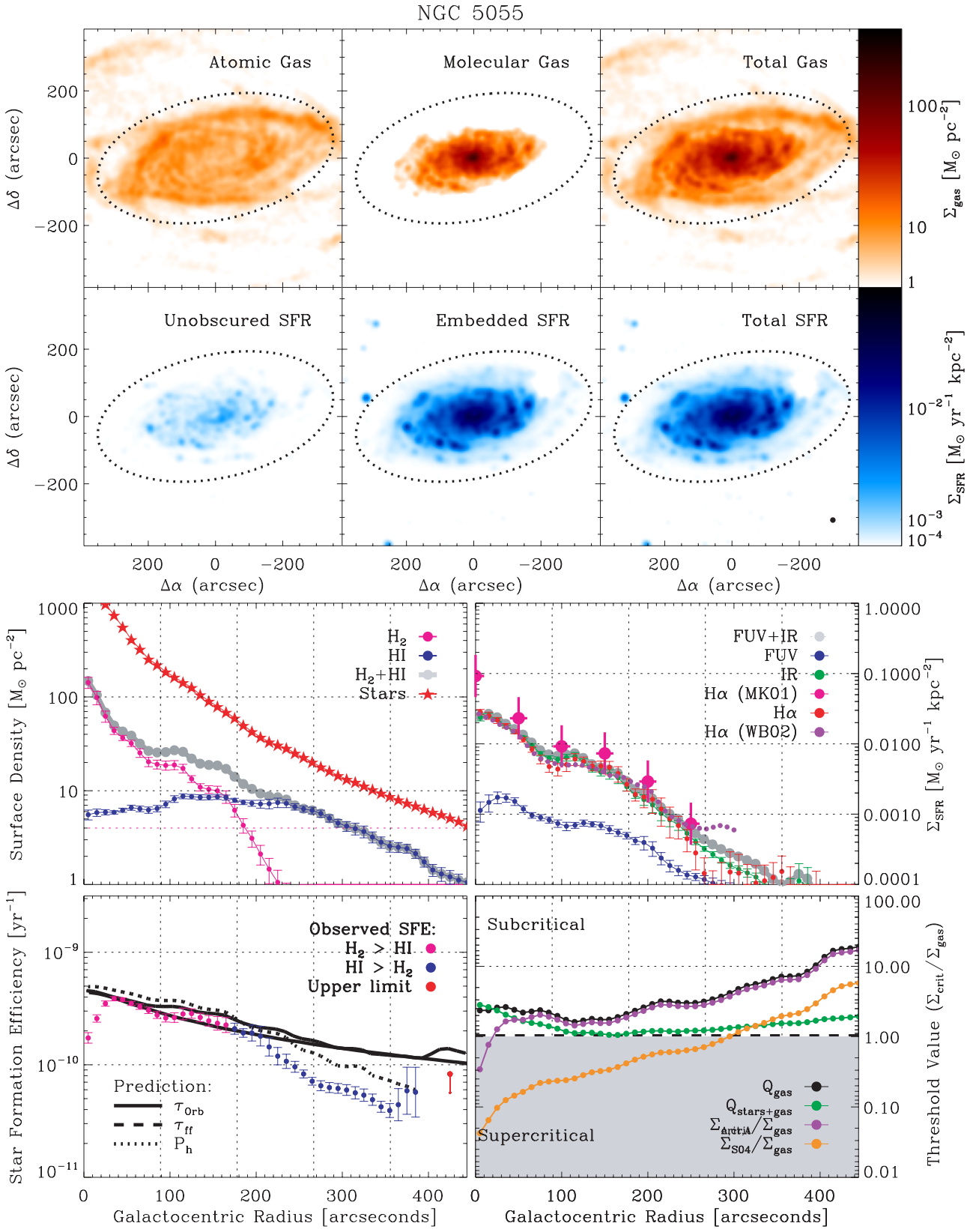

Figure 45. Atlas of data and calculations for NGC 5055.

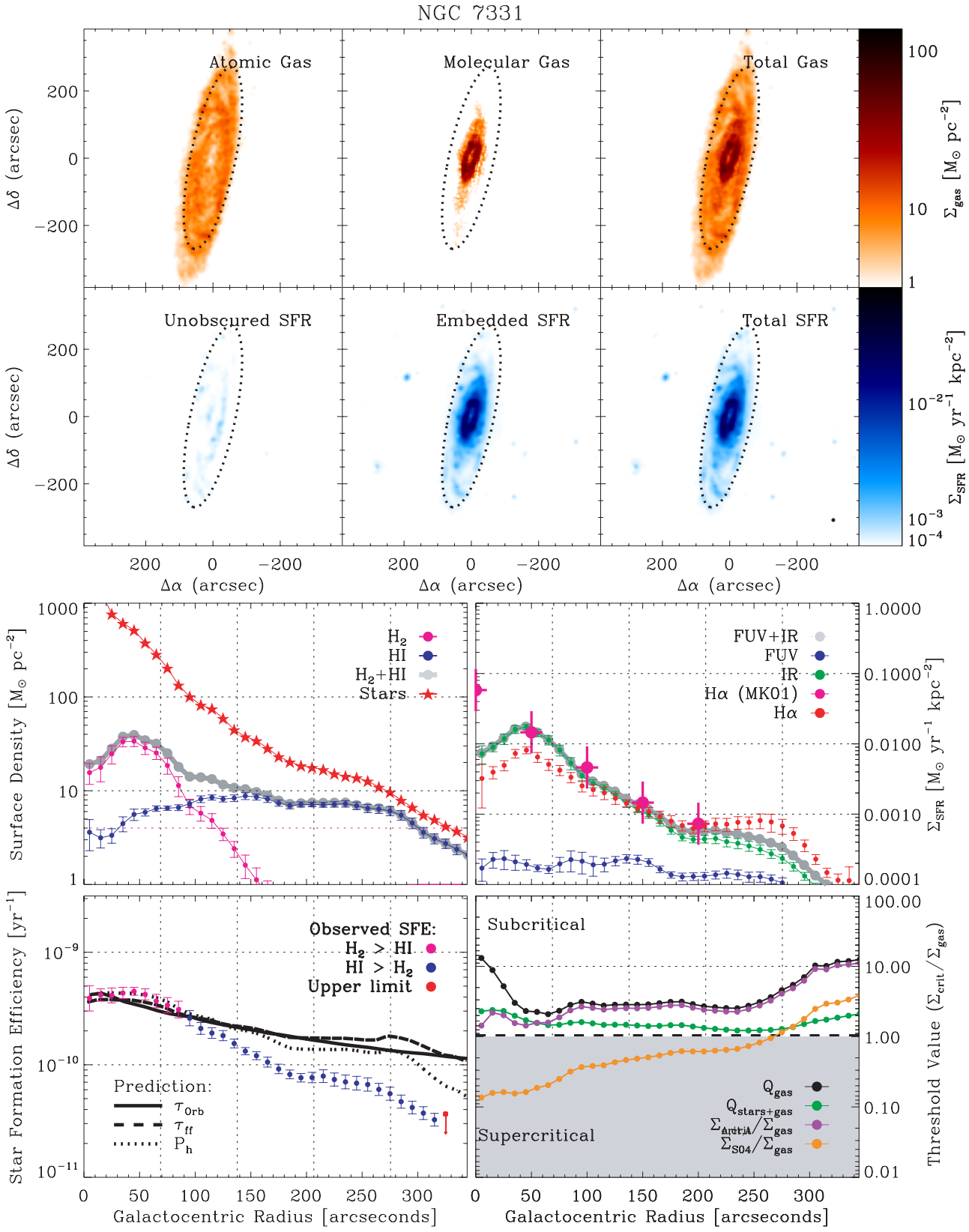

Figure 46. Atlas of data and calculations for NGC 7331.

Martin & Kennicutt (2001; magenta) and Wong & Blitz (2002; purple). All Hα profiles assume 1.1 mag of extinction (a typical average value in disk galaxies; Kennicutt 1998b). The other markings are as in the left panel.

In the left panel of the fourth row, we show the observed SFE for the galaxy. We use the same color scheme as in Section 4, that is, magenta points indicate rings where $\Sigma_{H_2} > \Sigma_{H1}$, blue points show rings where $\Sigma_{H_2} < \Sigma_{H1}$, and red arrows indicate upper limits. The ensemble of points in this panel combines to form Figure 1. Dashed, dotted, and dash-dotted lines show the SFE predicted following the method described in Section 6 with no threshold applied (the thresholds appear in the right panel). The other markings are as in the panels on the third row.

In the right panel of the fourth row, we show azimuthally-averaged values for thresholds described in Section 2.2. We expect widespread star formation (conditions are "supercritical") where the value of a profile is below 1 (the shaded area) and isolated or nonexistent star formation (conditions are "subcritical") above 1. We plot the Toomre Q parameter for a gas disk, $Q_{\rm gas}$ (black), and for a gas disk in the presence of stars, $Q_{\rm stars+gas}$ (green). We show the shear criterion described by Hunter et al. (1998a), $\Sigma_{\rm crit,A}/\Sigma_{\rm gas}$, in purple and the condition for the formation of a cold phase given by Schaye (2004), $\Sigma_{\rm S04}/\Sigma_{\rm gas}$, in orange. The other markings are as in the panels on the third row.

REFERENCES

Bell, E. F. 2003, ApJ, 586, 794
Bell, E. F., & de Jong, R. S. 2001, ApJ, 550, 212
Bell, E. F., McIntosh, D. H., Katz, N., & Weinberg, M. D. 2003, ApJS, 149, 289
Bigiel, F., Leroy, A., Walter, F., Brinks, E., de Blok, W. J. H., Madore, B., & Thornley, M. 2008, AJ, 136, 2846
Binney, J., & Merrifield, M. 1998, Galactic Astronomy/James Binney and Michael Merrifield (Princeton Series in Astrophysics; Princeton, NJ: Princeton Univ. Press)
Blitz, L. 1993, in Protostars and Planets III, ed. E. H. Levy & J. I. Lunine (Tucson, AZ: Arizona Press), 125
Blitz, L., Fukui, Y., Kawamura, A., Leroy, A., Mizuno, N., & Rosolowsky, E. 2007, in Protostars and Planets V, ed. B. Reipurth, D. Jewitt, & K. Keil (Tucson, AZ: Univ. Arizona Press), 81
Blitz, L., & Rosolowsky, E. 2004, ApJ, 612, L29
Blitz, L., & Rosolowsky, E. 2006, ApJ, 650, 933
Boissier, S., Prantzos, N., Boselli, A., & Gavazzi, G. 2003, MNRAS, 346, 1215
Boissier, S., et al. 2007, ApJS, 173, 524
Bolatto, A. D., Leroy, A. K., Rosolowsky, E., Walter, F., & Blitz, L. 2008, ApJ, 685, 948
Bottema, R. 1993, A&A, 275, 16
Braine, J., Combes, F., Casoli, F., Dupraz, C., Gerin, M., Klein, U., Wielebinski, R., & Brouillet, N. 1993, A&AS, 97, 887
Braun, R. 1997, ApJ, 484, 637
Buat, V., Boselli, A., Gavazzi, G., & Bonfanti, C. 2002, A&A, 383, 801
Calzetti, D., Bohlin, R. C., Kinney, A. L., Storchi-Bergmann, T., & Heckman, T. M. 1995, ApJ, 443, 136
Calzetti, D., Kinney, A. L., & Storchi-Bergmann, T. 1994, ApJ, 429, 582
Calzetti, D., et al. 2005, ApJ, 633, 871
Calzetti, D., et al. 2007, ApJ, 666, 870
Cardelli, J. A., Clayton, G. C., & Mathis, J. S. 1989, ApJ, 345, 245
Chabrier, G. 2003, PASP, 115, 763
Ciardullo, R., Durrell, P. R., Laychak, M. B., Herrmann, K. A., Moody, K., Jacoby, G. H., & Feldmeier, J. J. 2004, ApJ, 614, 167
Cortese, L., et al. 2006, ApJ, 637, 242
Crosthwaite, L., & Turner, J. 2007, AJ, 134, 1827
Dale, D. A., & Helou, G. 2002, ApJ, 576, 159
Dale, D. A., et al. 2007, ApJ, 655, 863
Dame, T. M., Hartmann, D., & Thaddeus, P. 2001, ApJ, 547, 792
Dib, S., Bell, E., & Burkert, A. 2006, ApJ, 638, 797
de Blok, E., et al. 2008, AJ, 136, 2648
de Blok, W. J. G., & Walter, F. 2006, AJ, 131, 363
de Grijs, R., & Peletier, R. F. 1997, A&A, 320, L21
Draine, B. T., et al. 2007, ApJ, 663, 866
Elmegreen, B. G. 1989, ApJ, 338, 178
Elmegreen, B. G. 1993, ApJ, 411, 170
Elmegreen, B. G. 1997, RevMexAA, 6, 165
Elmegreen, B. G., & Parravano, A. 1994, ApJ, 435, L121
Engargiola, G., Plambeck, R. L., Rosolowsky, E., & Blitz, L. 2003, ApJS, 149, 343
Fazio, G. G., et al. 2004, ApJS, 154, 10
Fukui, Y., et al. 1999, PASJ, 51, 745
Gil de Paz, A., et al. 2007, ApJS, 173, 185
Gordon, K. D., et al. 2005, PASP, 117, 503
Helfer, T. T., Thornley, M. D., Regan, M. W., Wong, T., Sheth, K., Vogel, S. N., Blitz, L., & Bock, D. C.-J. 2003, ApJS, 145, 259
Helou, G., et al. 2004, ApJS, 154, 253
Hunter, D. A., Elmegreen, B. G., & Baker, A. L. 1998, ApJ, 493, 595
Hunter, D. A., Wilcots, E. M., van Woerden, H., Gallagher, J. S., & Kohle, S. 1998, ApJ, 495, L47
Jarrett, T. H., Chester, T., Cutri, R., Schneider, S. E., & Huchra, J. P. 2003, AJ, 125, 525
Jog, C. J., & Solomon, P. M. 1984, ApJ, 276, 127
Johnson, B. D., et al. 2007, ApJS, 173, 392
Kennicutt, R. C. 1989, ApJ, 344, 685
Kennicutt, R. C. 1998, ApJ, 498, 541
Kennicutt, R. C., Jr. 1998, ARA&A, 36, 189
Kennicutt, R. C., Jr., et al. 2003, PASP, 115, 928
Kennicutt, R. C., Jr., et al. 2007, ApJ, 671, 333
Kim, W.-T., & Ostriker, E. C. 2001, ApJ, 559, 70
Kim, W.-T., & Ostriker, E. C. 2007, ApJ, 660, 1232
Kregel, M., & van der Kruit, P. C. 2005, MNRAS, 358, 481
Kregel, M., van der Kruit, P. C., & de Grijs, R. 2002, MNRAS, 334, 646
Kroupa, P. 2001, MNRAS, 322, 231
Krumholz, M. R., & McKee, C. F. 2005, ApJ, 630, 250
Lee, J. C. 2006, PhD thesis, Univ. of Arizona
Leitherer, C., et al. 1999, ApJS, 123, 3
Leroy, A., Bolatto, A. D., Simon, J. D., & Blitz, L. 2005, ApJ, 625, 763
Leroy, A. K., et al. 2008, AJ, 136, 2782
Li, Y., Mac Low, M.-M., & Klessen, R. S. 2005, ApJ, 626, 823
Li, Y., Mac Low, M.-M., & Klessen, R. S. 2006, ApJ, 639, 879
Lupton, R. H., Gunn, J. E., & Szalay, A. S. 1999, AJ, 118, 1406
Madore, B. F. 1977, MNRAS, 178, 1
Martin, C. L., & Kennicutt, R. C., Jr. 2001, ApJ, 555, 301
Martin, D. C., et al. 2005, ApJ, 619, L1
McKee, C. F., & Ostriker, E. C. 2007, ARA&A, 45, 565
McKee, C. F., & Ostriker, J. P. 1977, ApJ, 218, 148
Merrett, H. R., et al. 2006, MNRAS, 369, 120
Oh, S.-H., de Blok, W. J. G., Walter, F., Brinks, E., & Kennicutt, R. C., Jr. 2008, AJ, 136, 2761
Ott, J., Walter, F., Brinks, E., Van Dyk, S. D., Dirsch, B., & Klein, U. 2001, AJ, 122, 3070
Pahre, M. A., Ashby, M. L. N., Fazio, G. G., & Willner, S. P. 2004, ApJS, 154, 235
Pérez-González, P. G., et al. 2006, ApJ, 648, 987
Prugniel, P., & Heraudeau, P. 1998, A&AS, 128, 299
Rafikov, R. R. 2001, MNRAS, 323, 445
Regan, M. W., Thornley, M. D., Helfer, T. T., Sheth, K., Wong, T., Vogel, S. N., Blitz, L., & Bock, D. C.-J. 2001, ApJ, 561, 218
Riechers, D. A., Walter, F., Carilli, C. L., & Bertoldi, F. 2007, ApJ, 671, L13
Rieke, G. H., et al. 2004, ApJS, 154, 25
Robertson, B. E., & Kravtsov, A. V. 2008, ApJ, 680, 1083
Rosolowsky, E. 2005, PASP, 117, 1403
Rosolowsky, E. 2007, ApJ, 654, 240
Rosolowsky, E., Engargiola, G., Plambeck, R., & Blitz, L. 2003, ApJ, 599, 258
Roussel, H., Gil de Paz, A., Seibert, M., Helou, G., Madore, B. F., & Martin, C. 2005, ApJ, 632, 227
Salim, S., et al. 2007, ApJS, 173, 267
Salpeter, E. E. 1955, ApJ, 121, 161
Sawada, T., et al. 2001, ApJS, 136, 189
Schaye, J. 2004, ApJ, 609, 667
Schlegel, D. J., Finkbeiner, D. P., & Davis, M. 1998, ApJ, 500, 525
Schmidt, M. 1959, ApJ, 129, 243
Schmidt, M. 1963, ApJ, 137, 758
Schuster, K. F., Kramer, C., Hitschfeld, M., Garcia-Burillo, S., & Mookerjea, B. 2007, A&A, 461, 143
Schuster, K.-F., et al. 2004, A&A, 423, 1171
Shapiro, K. L., Gerssen, J., & van der Marel, R. P. 2003, AJ, 126, 2707
Silk, J. 1997, ApJ, 481, 703

Skillman, E. D. 1987, in Star Formation in Galaxies, ed. C. J. Lonsdale Persson (Greenbelt, MD: NASA), 263
Solomon, P. M., Rivolo, A. R., Barrett, J., & Yahil, A. 1987, ApJ, 319, 730
Springel, V., & Hernquist, L. 2003, MNRAS, 339, 289
Strong, A. W., & Mattox, J. R. 1996, A&A, 308, L21
Tamburro, D., Rix, H.-W., Leroy, A. K., Mac Low, M.-M., Walter, F., Brinks, E., & de Blok, W. J. G. 2008a, AJ, submitted
Tamburro, D., Rix, H.-W., Walter, F., Brinks, E., de Blok, W. J. G., Kennicutt, R. C., & Mac Low, M.-M. 2008b, AJ, 136, 2872
Tan, J. C. 2000, ApJ, 536, 173
Taylor, C. L., Kobulnicky, H. A., & Skillman, E. D. 1998, AJ, 116, 2746
Temi, P., Brighenti, F., & Mathews, W. G. 2005, ApJ, 635, L25
Thornley, M. D., Braine, J., & Gardan, E. 2006, ApJ, 651, L101
Toomre, A. 1964, ApJ, 139, 1217
Trachternach, C., de Blok, W. J. G., Walter, F., Brinks, E., & Kennicutt, R. C., Jr. 2008, AJ, 136, 2720
van der Kruit, P. C. 1988, A&A, 192, 117
van der Kruit, P. C., & Searle, L. 1981, A&A, 95, 105
Walter, F., Taylor, C. L., Hüttemeister, S., Scoville, N., & McIntyre, V. 2001, AJ, 121, 727
Walter, F., et al. 2007, ApJ, 661, 102
Walter, F., et al. 2008, AJ, 136, 2563
Wolfire, M. G., Hollenbach, D., & Tielens, A. G. G. M. 1993, ApJ, 402, 195
Wolfire, M. G., McKee, C. F., Hollenbach, D., & Tielens, A. G. G. M. 2003, ApJ, 587, 278
Wong, T., & Blitz, L. 2002, ApJ, 569, 157
Wyder, T. K., et al. 2007, ApJS, 173, 293
Yang, C.-C., Gruendl, R. A., Chu, Y.-H., Mac Low, M.-M., & Fukui, Y. 2007, ApJ, 671, 374
Young, J. S., et al. 1995, ApJS, 98, 219
Young, L. M., van Zee, L., Lo, K. Y., Dohm-Palmer, R. C., & Beierle, M. E. 2003, ApJ, 592, 111